UNIVERSITÀ DEGLI STUDI DI PERUGIA

FACOLTÀ DI SCIENZE MM.FF.NN.

DIPARTIMENTO DI FISICA

Tesi di Dottorato di ricerca in Fisica

A Monte Carlo simulation of the cosmic rays interactions with the near Earth environment

Paolo Zuccon

Relatore : *Ch. Prof.* R. BATTISTON

Corelatore : *Dr.* B. BERTUCCI

Coordinatore del Corso di Dottorato : *Ch. Prof.* P. SODANO

Perugia, Ottobre 2002

To my family.

Contents

Introduction

The study of cosmic radiation and of its interaction with the Earth atmosphere and magnetosphere is the subject of a wide and lively experimental program since the beginning of last century. Ground, underground, balloon borne and space based detectors have been conceived along the years to pursue this research program which ranges over different domains of fundamental physics.

In all these experiments, a different, but always relevant, role is played by the cascade of secondary particles originated in the interaction of cosmic rays with the atmosphere.

Atmospheric secondaries can be considered in turn the *beam* or the background for underground particle physics experiments. Alternatively, they are the signal for ground based indirect studies of high energy cosmic rays or the background for direct detection of cosmic rays in the stratosphere. Secondaries escaping the atmosphere contribute to the radiation measured by spaced based experiments.

The interpretation of observational data depends in most cases on a realistic model for the production atmospheric secondaries and their transport to the experimental apparatus. Quite different approaches to this problem - with only marginal overlaps - have been used in different physical contexts.

A large number of Monte Carlo simulation codes has been developed to describe the aspects of production and development of atmospheric cascades relevant to their detection either in specific ground sites or in the restricted regions of stratosphere covered by balloon borne experiments. The focus of these models is largely put on a *local* description of the atmospheric cascade, with an accurate simulation of the elementary interactions taking place at the different stages of the shower development. A much coarser treatment - if any - is done of geomagnetic effects on the the transport of primary cosmic rays and atmospheric secondaries.

A different approach is used in all models applied to the study of the radiation environment in the space near Earth. There, a major emphasis is naturally put on the structure of the earth magnetosphere and on the transport of the cosmic radiation in the magnetic field, while the contribution of atmospheric secondaries is treated by means of semi-analytic models.

In the last few years, the need for a *unified* approach, where both particle

interactions and geomagnetic effects are accurately taken into account, has been stressed in quite different contexts.

An anomalous flavor ratio of atmospheric neutrinos has been found in different underground experiments. Its interpretation in terms of flavor oscillations in the ν system must be based on a solid prediction on the atmospheric production of different ν species. This naturally implies an accurate description of the physical processes leading to the ν production, however, a relevant influence of geomagnetic effects on the intensity, the energy spectrum and the angular distributions of ν revealed at different experimental sites has been widely recognized.

Large fluxes of particles have been measured by the AMS experiment at energies where cosmic rays are forbidden to reach the space near Earth due to the presence of the geomagnetic field. Their interpretation as atmospheric secondaries escaped in space has been immediately advanced, originating a lively debate on the relevance of this radiation component as a background for future satellite experiments and as a possible additional source in the generation of atmospheric neutrinos. A quantitative answer to the questions opened by the AMS measurements implies a description of the interactions of primary cosmic rays over the whole Earth's atmosphere coherently taking into account the geomagnetic effects.

This thesis presents a new versatile Monte Carlo simulation conceived to reproduce the main physical processes to which cosmic rays and atmospheric produced secondaries are subjected near Earth. The comparison with AMS measurements of H and $e^{\pm}$ fluxes has been chosen as benchmark for this simulation. This choice insures a severe test of our model, due to the accuracy and wide geographical and energy coverage of AMS data, and at the same times allows a more complete understanding of the AMS results.

Many *ingredients* enter into our model, the first three chapters are devoted to their description and to the discussion of their representation in our simulation. Experimental measurements of cosmic ray fluxes near Earth are reviewed in the first chapter, together with the models for their origin and propagation. In the second chapter, the structure of the magnetic field in the Earth proximity is described. The dynamical features of charged particles in the geomagnetic field are discussed, introducing the formalism of the adiabatic invariants and magnetic shells needed to describe trapped radiation. In the third chapter, the setup of the simulation is presented, the technical issues discussed and the modelling of the different components reviewed.

The AMS detector and its measurements of H and $e^{\pm}$ fluxes are concisely presented in the fourth chapter. A detailed comparison of the simulation results with the AMS measurements is performed in Chapter 5. There, in the light of a successful comparison, a coherent explanation of the origin and the dynamical features of the AMS fluxes is given. Their production mechanisms are discussed as well as the dynamics of their extraction from atmosphere.

Chapter 1

Cosmic rays near Earth

The first hints for the presence of an ionizing radiation of unknown origin date to the early years of 1900, when *anomalous* discharge rates were observed in electroscopes placed in ground based laboratories. Evidence of the extraterrestrial origin of this radiation came in 1912 with the first pioneering measurements on balloon (Hess [1], Kohlhörster [2]) of the increasing ionization rate with the altitude. Only later, in the 1929, Bothe and Kohlhörster [3] using the *new* geiger counter and the coincidence technique made the first measurements of single cosmic rays events, proving that they are composed of charged particles. Since then, and up to the fifties, cosmic rays played a major role in the discovery and the study of elementary particles, giving birth to the high energy particle physics. With the advent of particle accelerators, the interest in cosmic rays as a source of high energy particles rapidly fell off, leaving to the astrophysical domain the open questions on their nature, origin, and propagation history from their sources to the Earth. Forty years of continuous experimental effort, on ground as well as in the stratosphere and in space, have supplied us with a large amount of information about the cosmic ray flux composition and intensity in an energy interval which covers many decades.

In this chapter we discuss the features of the cosmic rays flux reaching the Earth. After a general description of this flux, we review the present experimental measurements of galactic cosmic rays. A discussion on the origin, the acceleration mechanisms and the propagation models of the galactic cosmic rays completes this chapter.

1.1 The cosmic rays landscape

Cosmic rays impinging on the Earth atmosphere are observed on a wide range of energies, that spans ~ 12 orders of magnitude. The nature and the origin of these particles is depending on the energy range considered.

Up to the energy of the order $\sim 100\, MeV/nucleon$ the observed flux of

cosmic rays reaching the Earth is of heliospheric origin. The solar wind, a steady flux of charged particles outgoing from the sun prevents extra solar cosmic rays with energy below this limit to reach the Earth vicinity.

Most of the cosmic ray flux observed below $\sim 100\,MeV$ is composed by solar energetic particles (SEP). These particles are fully ionized nuclei present in the solar wind and in the solar system interplanetary medium, which are accelerated by shock waves in the solar wind flux. These shock waves are usually related to energetic solar events but can be also originated from the interaction of the solar wind with the magnetic fields of the planets. Most energetic SEP are produced during solar flare eruption events that are able to accelerate the particles up to the energy of few $GeVs$ [7]. Data supporting this picture have been collected by the Pioneer 10 mission in the '80 and are discussed in [6]. The measured elemental composition of SEP matches with the observed composition of the solar wind confirming the hypothesis on the origin of these particles.

Another component distinguished from the SEP is contributing to the fluxes in the range of energies of $10 \div 50\,MeV/nucleon$: the so called Anomalous Cosmic Rays (ACR). ACR are single ionized nuclei reaching the top of the Earth's atmosphere and are believed to represent interstellar neutral nuclei that have drifted into the heliosphere, become ionized by the solar wind or by the UV radiation, and then accelerated at energies $> 10\,MeV/nucleon$, probably at the solar wind termination shock. The measured energy spectra of the ACR then carry important information to test the acceleration theories of cosmic rays at shock waves and their transport through the heliosphere.

Extra solar cosmic rays, usually called Galactic Cosmic Rays (GCR), represent the dominant component of the cosmic rays flux in the Earth vicinity, for energies above $\sim 100\,MeV$. They are particles accelerated at distant sources, which propagate in the galaxy through relatively weak magnetic fields experiencing electromagnetic and nuclear interactions with photons and nuclear matter in the interstellar medium. Approaching the heliosphere they interact with the fields carried by the solar wind, which effectively modify their flux intensity up to the energy of several GeVs. Cosmic rays of highest energy, are considered by some authors to have an extra galactic origin. Galactic cosmic rays are composed mostly of fully ionized nuclei H (85%), He (12%), heavier nuclei (1%) and a small component of electrons ($\sim 2\%$). There is also a very small contribution $O(0.1\%)$, of positron and antiprotons which are likely to be produced in secondary reactions with the interstellar medium. Figure 1.1 shows the differential flux as function of the kinetic energy per nucleon of the cosmic rays nuclear components.

The dependence on the energy of the differential flux for a given species i is well described by a power law:

$$\Phi(E_k) = K_i\, E_k^{-\gamma_i} \tag{1.1}$$

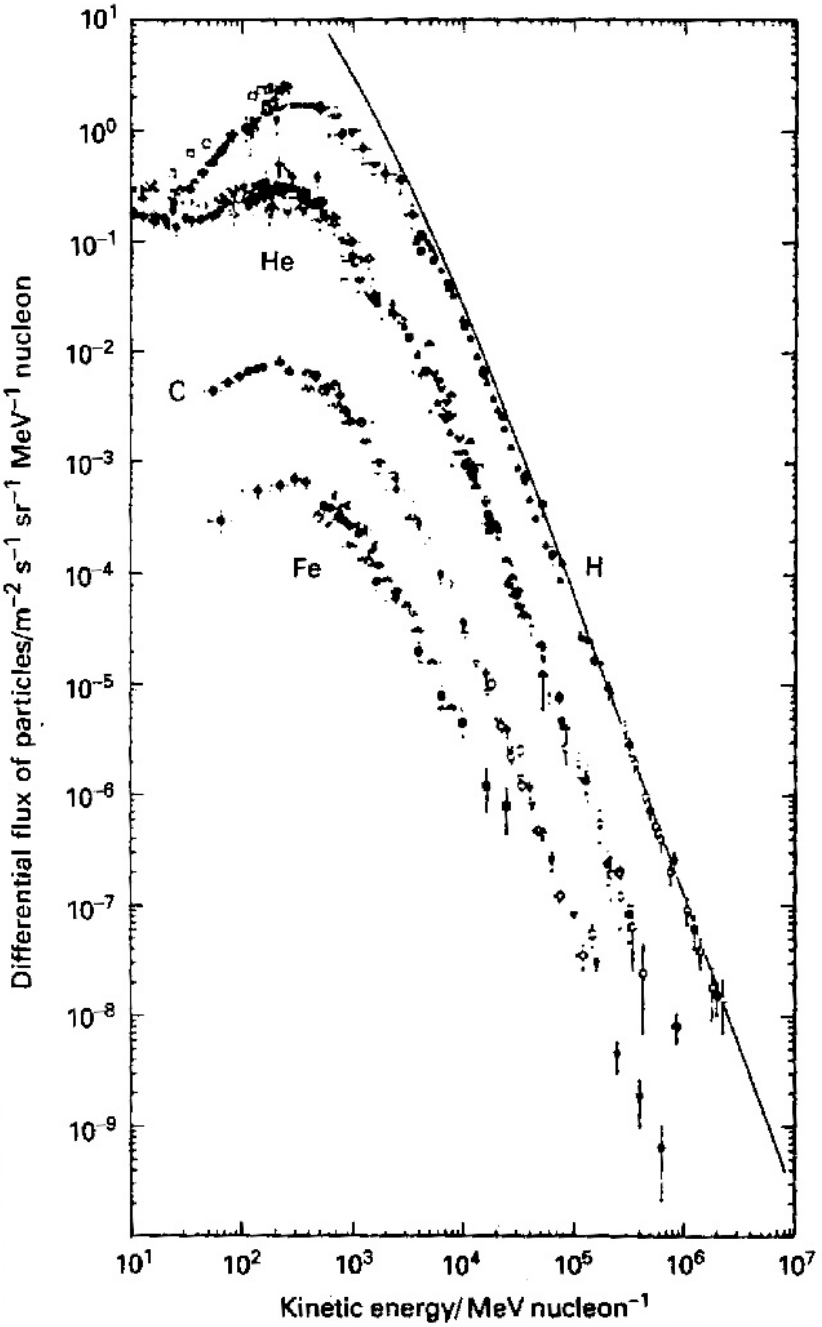

Figure 1.1: The differential spectra of cosmic rays as measured at the Earth. The spectra for hydrogen, helium, carbon, and iron are shown, solid line shows the unmodulated spectrum for hydrogen.

where E_k is the kinetic energy per nucleon, K_i is a normalization factor,and γ_i is the spectral index. Values of the spectral index in the range $2.5 - 3.1$ have been observed for the different nuclear species composing the cosmic rays flux.

The deviation from the power law, observed below $10\,GeV$, is a consequence of the already cited influence of the solar wind called *solar modulation* [10]. Flux intensity in this energy range is anti-correlated to the solar activity and it follows the sun-spot 11-years cycle. Figure 1.3 shows the H and He energy spectra in different conditions of the solar activity. The correlation between the solar activity and the modulation of the cosmic rays flux has been studied by the monitoring of the flux of atmospheric neutrons. In fact, a flux of low energy neutrons ($E \sim O(10^8 - 10^9)eV$) is produced in the interaction of primary CRs with the atmosphere and it is mostly due to low energy primaries ($1 - 20\,GeV$), due to the rapid fall of the primary flux intensity with energy. Figure 1.2 shows the data collected in the last 50 years.

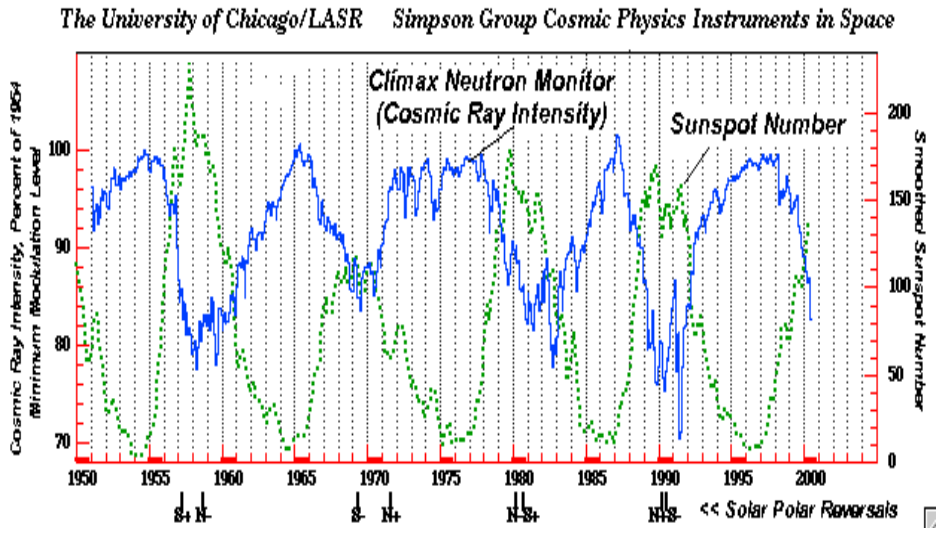

Figure 1.2: Cosmic rays intensity variation (neutron counts) anti-correlated with the eleven-years sun spot cycle.

In our study, we are mainly concerned with the GCR flux, which represents the *beam* for the production of energetic secondaries in atmosphere. In the following, we will review the experimental knowledge on GCR flux intensity and composition, briefly discussing the current hypotheses on GCR origin and propagation.

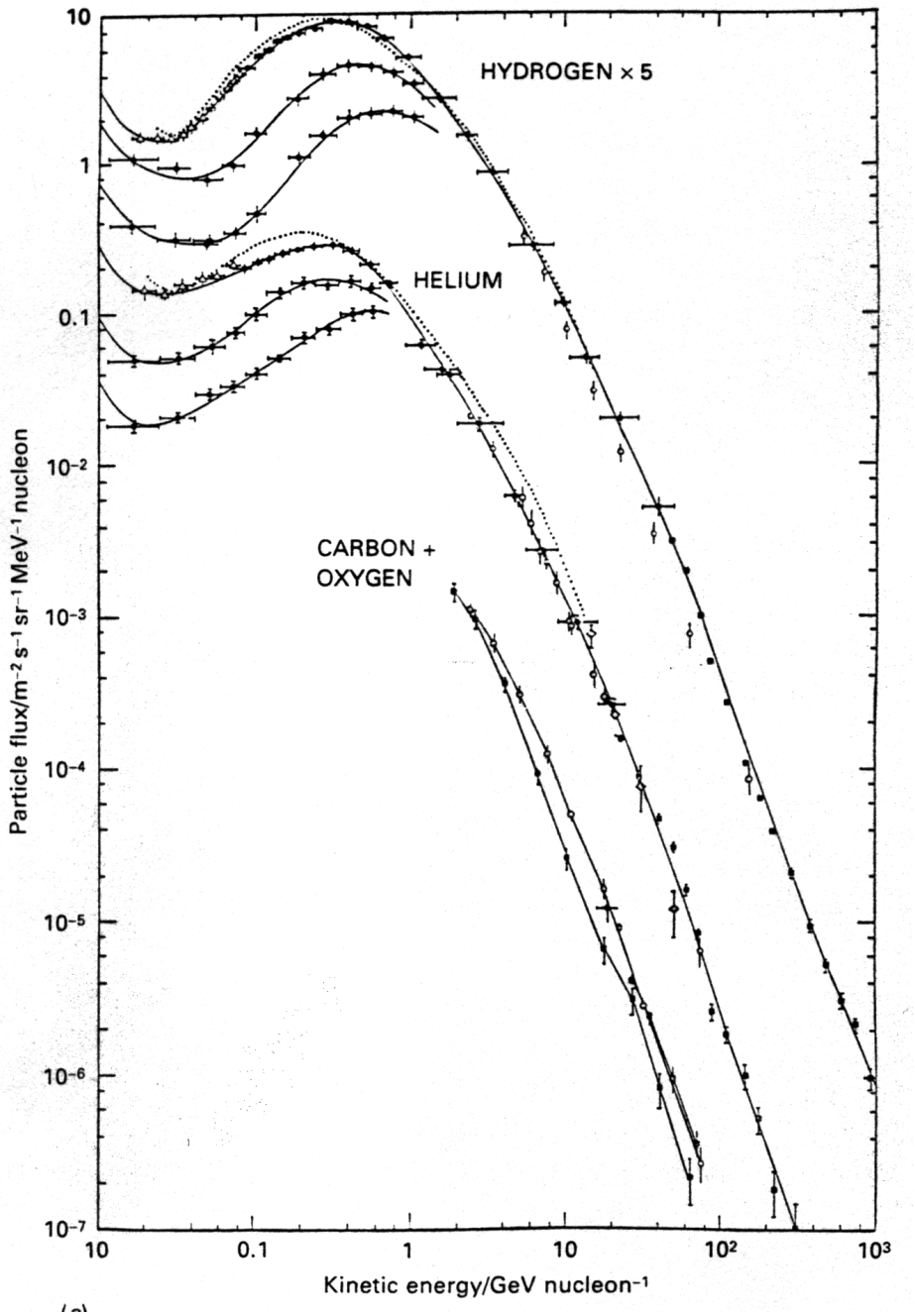

Figure 1.3: Energy spectra of H and He plotted for minimum (upper plot), intermediate and maximum (lower plot) solar modulation effect. The H spectra have been multiplied by a factor 5 for a better reading. Figure from [12].

1.2 Experimental measurements of GCRs

Figure 1.4 is showing the differential energy spectrum of the whole GCR flux as measured at Earth, the extremely wide energy range and the rapid fall with energy of the flux intensity illustrates the experimental challenge in measuring composition, directional distribution and spectrum energy of the different species.

The overall GCR spectrum, above the threshold of the solar modulation, follows a power law with a spectral index $\gamma = 2.7$. At the energy of $\sim 10^{15}\, eV$ the spectrum dips and the slope change to $\gamma = 3.1$ this feature is called *the knee*. At about $3 \times 10^{18}\, eV$, there is another slope change but in opposite direction, the so called *ankle*. The spectrum becomes hard to quantify, but can again approximately described by $\gamma = 2.7$.

There is some limited evidence from the newest experiments (AGASA [8] and HiRes [9, 13]) for another feature at about $3 \times 10^{17}\, eV$, called the *second knee* where the spectrum appears to dip further (see fig. 1.5). There are no other strong features in the overall spectrum, especially no cutoff at the upper end has been observed yet.

Detection techniques are dependent on the energy range considered and on the typical intensity expected, they can be ideally divided in direct and indirect measurements.

Direct measurements of cosmic rays must be performed in space, or at least in the stratosphere, to avoid any contamination from secondaries produced in the atmospheric interactions. The carrier technology puts severe constraints on the weight and the size of the experimental apparatus and on the exposure time of the detector. Direct detection is therefore practically forbidden at energies above some TeVs by the low statistics and already suffers of large uncertainties at a few hundred GeVs.

At higher energies only indirect detection is viable. The interactions of the CR in the atmosphere produce a cascade of secondary particles (sketched in fig. 1.6), which are revealed on large ground based detectors.

The energy, the arrival direction and the nature of the CR are therefore indirectly derived from the observation of the features of the fraction of the shower reaching the ground based detector. The reliability of these measurements depends on how large is the mean fraction of the shower seen by the detector and on the model used to describe the shower development in the atmosphere. Both these aspects are more and more challenging as the observed primary cosmic ray energy increases, since the size of the shower is enlarging at the same time and the knowledge of the feature on the nucleus-nucleus interaction is worsening.

Direct measurements are performed below $\sim 10\, TeV$. These measurements are particulary interesting for us since the cosmic rays fluxes up to $\sim 1\, TeV$ represent the input data of the simulation developed in this work.

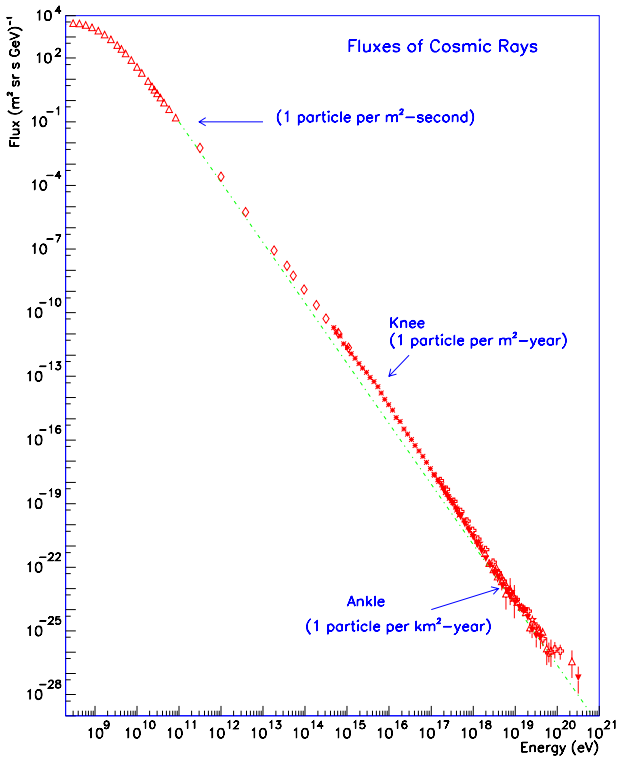

Figure 1.4: The overall cosmic ray spectrum over the whole energy range observed. Figure from an original of S. P. Swordy.

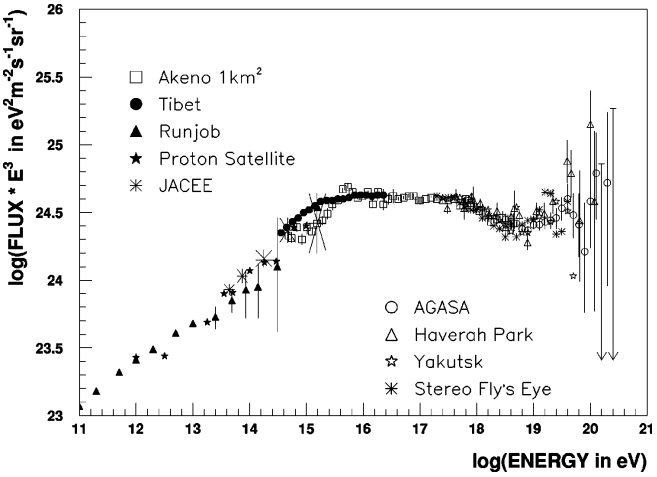

Figure 1.5: Measurements of the highest energy cosmic rays. To emphasize the knee, the second knee and the ankle, the spectrum has been multiplied by E^3. Figure from [11].

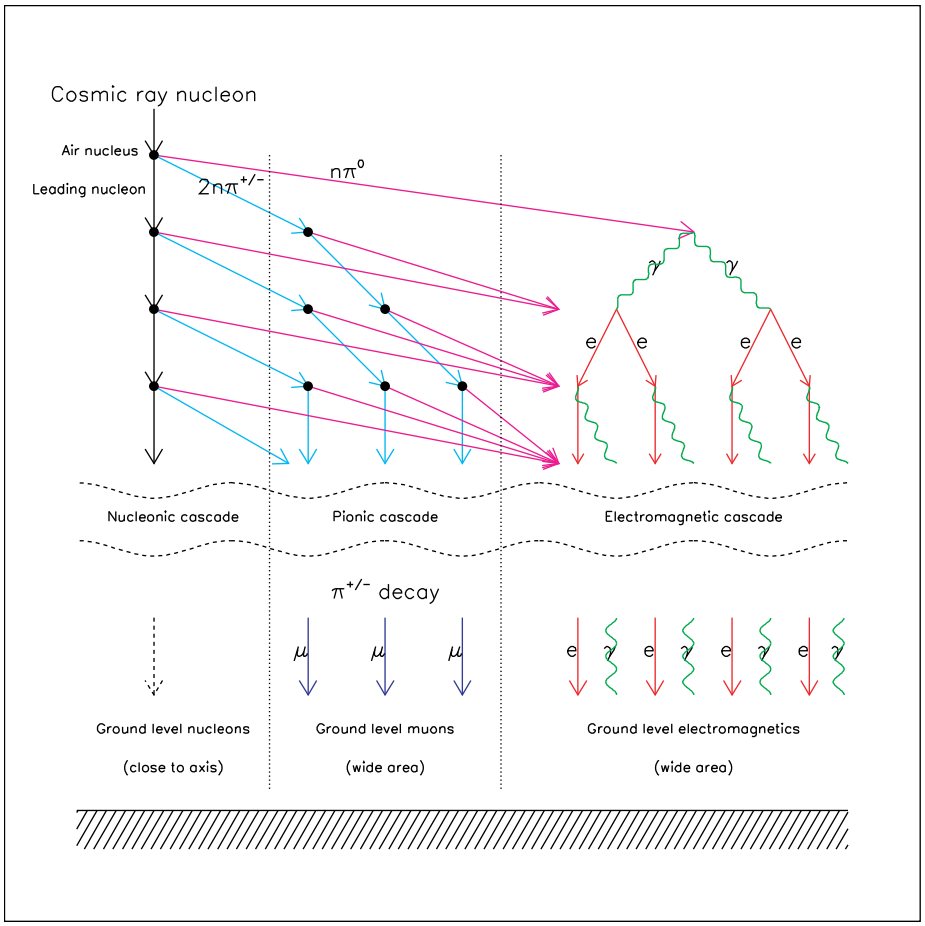

Figure 1.6: Schematic view of shower development in the atmosphere. Figure from [22]

1.2.1 Direct measurements

Various detection techniques have been used to measure cosmic ray fluxes on stratospheric balloons or in space depending on the main objective of the various experiments. A main distinction can be done between experiments based on magnetic spectrometers or different techniques.

The use of magnetic spectrometers is mandatory to look for *rare* components of the CR fluxes ($e^{\pm}, \bar{p}$) or to search for nuclear anti-matter, i.e. whenever a determination of the charge sign of the incoming CRs is needed. For these measurements, ancillary detectors (Time of Flight hodoscopes, Transition Radiation Detectors, Çerenkov detectors, Calorimeters) are used in the particle identification, building up to a redundant experimental apparatus which can be optimal also in measuring the energy spectrum and composition of the nuclear CR species.

However, the use of magnetic spectrometers is effectively disfavored at high CR energies by the difficulties in building a magnet with a large bending power and large acceptance fulfilling the requests of light-weight and low power consumption imposed by the operation on balloon or in space. These circumstances, together with the limited exposure time of the experiments, have *de facto* restricted the use of spectrometers in the measurement of the nuclear CR component. Spectrometric measurements are up to now available mainly for H and He fluxes, and up to a maximal rigidity of $\sim 200 GV/c$.

Larger acceptances are obtained with calorimeters and nuclear emulsion stacks, which instead have been used when the energy reach or the nuclear composition were the main issue, with the major drawback of a difficult intrinsic detector calibration.

Future projects of long duration balloon flights and long term space based experiments will soon change the current picture. Two experiments are scheduled to take measurements of the cosmic rays fluxes in low Earth orbit both for a three years mission, Pamela [21] that will orbit on a satellite from 2003 and the large acceptance AMS02 [23] that will be installed in 2005 on the International Space Station.

Isotropy Direct measurements of the different element in cosmic rays flux up to the TeV region are showing an isotropic distribution of the cosmic rays arrival directions.

Hydrogen Spectrum Hydrogen is the main component of the cosmic rays flux and many experiments precisely measured the H primary spectrum. A good knowledge of the H spectrum is also fundamental for all the experiments that aim to measure rare components of the cosmic rays flux since it represent the principal background source.

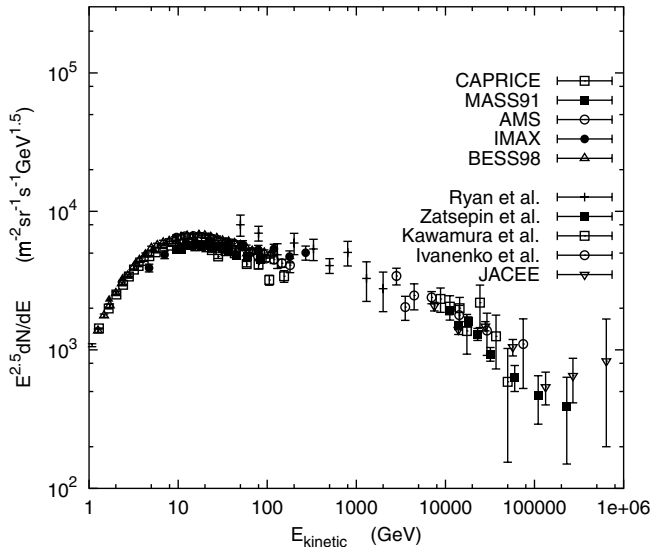

Figure 1.7: Measurements of differential flux of protons.

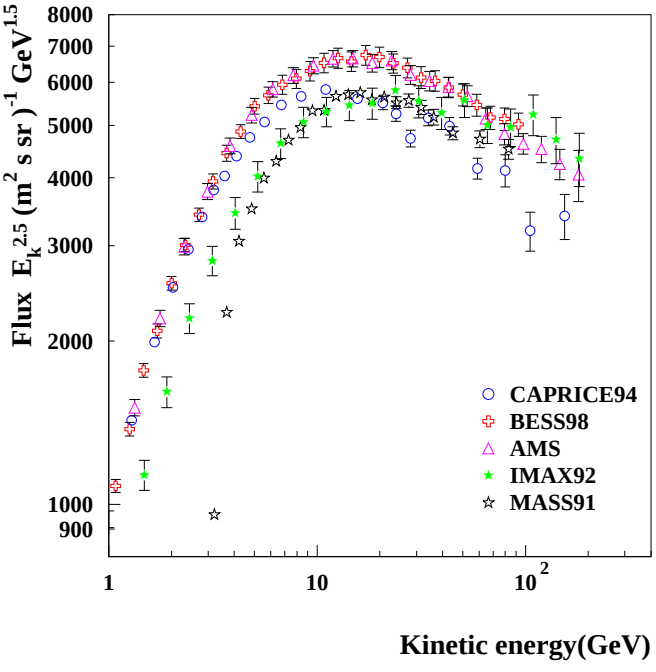

Figure 1.8: Measurements of differential flux of protons up to 200 GeV.

The available measurements can be divided in two groups, those up to $\sim 200\,GeV$ obtained with magnetic spectrometers and those above this limit done with calorimeter detectors. The only measurements that spans above and below $200\,GeV$ are those of Ryan et al. [25], obtained with a balloon borne calorimeter in the '70.

Figure 1.7 shows the full set of measurements up to $\sim 1000\,TeV$ the different precision of the two groups of measurements is evident.

Figure 1.8 shows the most recent measures covering the initial part of the spectrum. These data can be classified in three groups: the AMS measurements done with a magnetic spectrometer that flew onboard the Space Shuttle Discovery; the measurements done with BESS [97], a balloon borne spectrometer by an American-Nippon group; and the others, the campaign conducted by the Wizard collaboration with the balloon borne spectrometers MASS [94] and CAPRICE [124], and the experiment IMAX [96]. This last experiment can be included in this category since it share with MASS and CAPRICE the same the same NMSU/NASA balloon magnet facility.

Below $\sim 10\,GeV$ the agreement is possible only between experiments that took data in periods of comparable solar activity. A good agreement is observed between AMS, BESS98, and CAPRICE94, which took data on periods of solar minimum while the expected trend is observed for IMAX92 (intermediate solar activity), and MASS91 (solar maximum).

Above $\sim 10\,GeV$ we observe that AMS and BESS well agree each other while the other experiments tends to converge to a smaller flux. The flux measurement of BESS and AMS are actually preferred [89], because of the good agreement ($\sim 5\%$) between this two experiments whose are operating in different environments and have completely different systematic errors. Furthermore both AMS and BESS measurements have a larger statistical significance with respect the others.

The limited agreement with the previous experiments ([93, 94, 95, 96]) is partially explained by the limited statistic collected by these experiments, visible also in the fluctuations above $10\,GeV$. Furthermore, a common systematic error could affect all these experiments since they are all based on the same balloon/magnet facility.

At higher energies (fig. 1.7) the situation is not as good, measurements have been done by balloon-borne calorimeters of various kinds ([25, 103, 104, 105, 106]). These do not capture all the energy of the primary and, as a consequence, the energy determination is not as precise as with spectrometers. In the region of overlap between high and low energy data, the former are about 25% higher.

Helium Spectrum Almost the same experiments that measured the H spectrum took data also on He. Figure 1.9 shows the available measurements up to $\sim 100\,TeV/nucleon$, also in this case the separation in two

groups is evident: the more precise measurements done with the spectrometers up to energies $\sim 100\,Gev/nucleon$ and the calorimeter measurements above this limit. In the high energy region the measures from JACEE [103], Sokol [104], Ichimura et al. [24] are affected by very large statistical errors.

Figure 1.10 shows the most recent measurements made with magnetic spectrometers. Also for He spectrum the AMS and BESS measurements are the more accurate actually available, in this case the agreement between the two sets of data is at the level of $\sim 10\%$ [89]. Data from CAPRICE, MASS and IMAX, seems to indicate a lower flux with respect AMS and BESS data, anyway the large statistical errors do not allow for a detailed comparison.

Spectra of nuclei with $Z > 2$ Due to their small flux, at least 2 order of magnitude smaller than H flux, high-Z nuclei spectra have been measured only by long duration/high-acceptance experiments. The best measurements up to $\sim 10\,GeV/nucleon$ have been collected in the '80 by two satellite experiments [16, 15]. At higher energies only calorimetric measurements are available, detectors are based on nuclear emulsions (RUNJOB [105], JACEE [103]), on BGO calorimeters (ATIC [99]), on scintillating fibers calorimeters (TIGER [100]), and TRD detectors (TRACER [101]).

As an example, figure 1.11 from ref. [14] shows the spectra of elements of the Li group and of the sub-Fe group together with a fit to the data.

A throughout review of these measurements goes beyond the scope of this discussion and we refer the reader to ref. [14] where the available experimental data are exposed and discussed.

Figure 1.12 shows solar system abundances of different nuclear species[1] compared to the abundances found abundances in cosmic rays. The following features are immediately evident:

1. an odd-even effect in the relative stabilities of the nuclei according to the atomic number known to be present in the Solar System abundances of elements is also present in the cosmic rays but to a somewhat less degree

2. there is a net under abundance of H and He in the cosmic rays

3. the light elements Li, Be, B are grossly overabundant in the cosmic rays relative to their Solar System abundances

4. there is an excess abundance in the cosmic rays of elements with atomic and mass numbers just less than those of Fe, i.e. elements with atomic numbers between about Ca and Fe

[1] Solar system abundances are very similar to the composition of the interstellar medium.

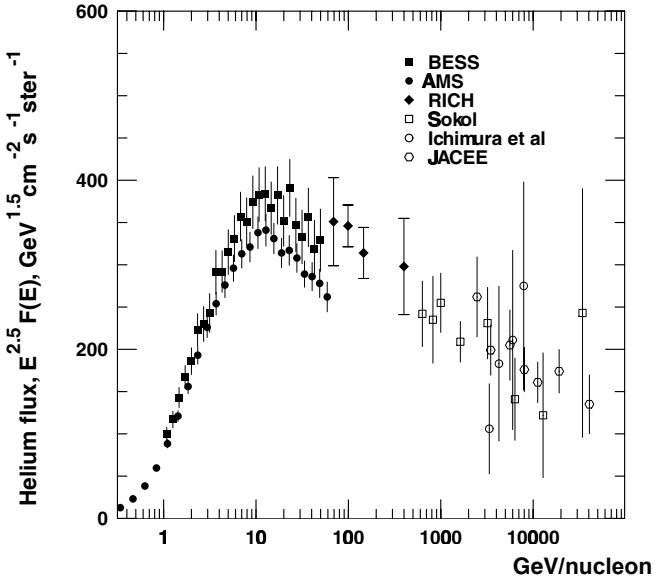

Figure 1.9: Differential flux of Helium compared. Figure from [89].

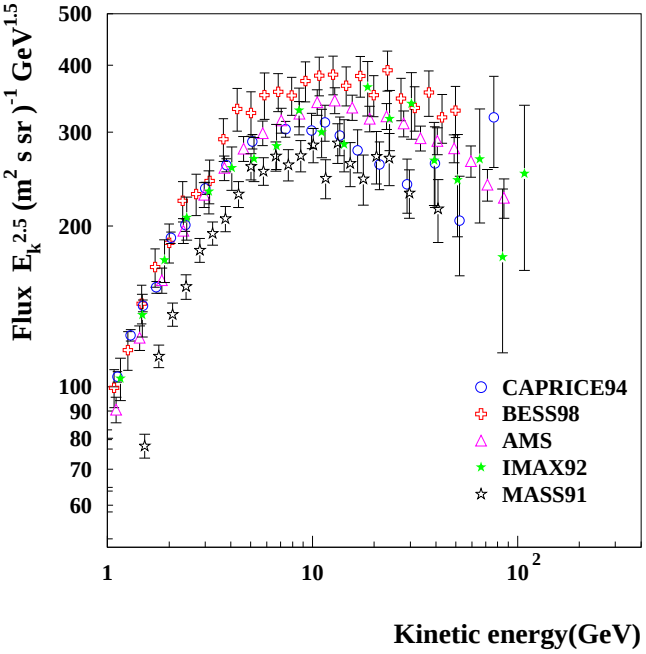

Figure 1.10: Differential flux of Helium compared up to 200 $GeV/nucleon$.

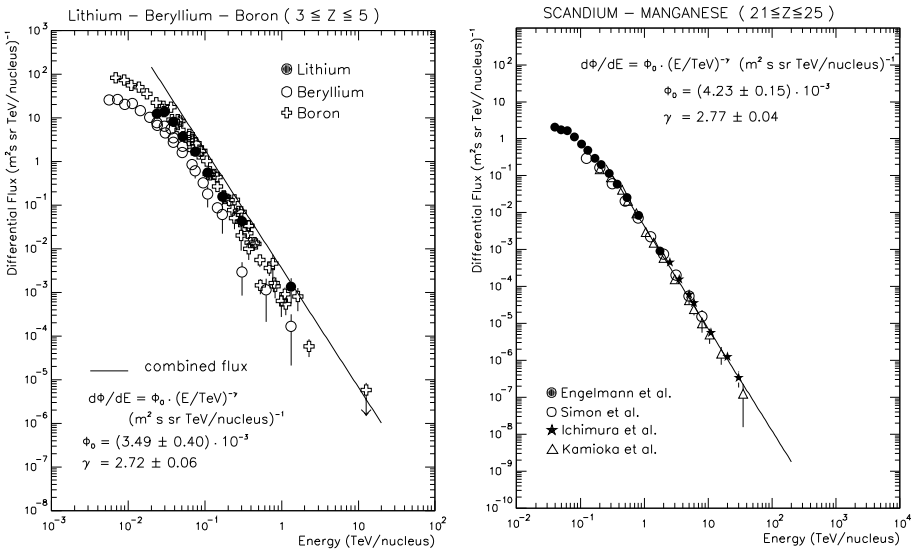

Figure 1.11: Left: Data of Li,Be and B differential fluxes, including the fit for the combined flux. Right: The spectrum of the sub-Fe group elements including the fit. Figure from [14].

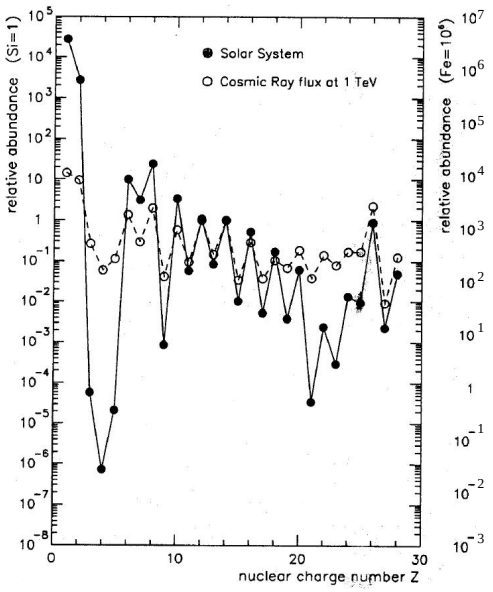

Figure 1.12: The chemical composition of cosmic rays relative to Silicon and Iron at $1\,TeV$, and in the solar system, as function of nuclear charge Z, from [14].

It is remarkable that overall, the distribution of element abundances in the cosmic rays presents the same features of the Solar System abundances. The differences are explained in terms of the models of the cosmic rays sources and the comic rays propagation through the galaxy. Specifically, those of points 3 and 4, can be accounted as result of the spallation reactions occurred during the propagation of cosmic rays through the interstellar medium. The under abundance of H, He and of the elements from C to Ne, is arising from the large ionization potential of these nuclei that introduce a selection mechanism in the acceleration processes.

1.2.2 Indirect measurements

At energies greater than $10^{14}\,eV$, the cosmic rays flux becomes smaller than 1 particle per m^2 per year and only long duration ground based experiments are permitting good measurements. At the same time at energies above some $TeVs$ the Earth atmosphere can be thought as a calorimeter with a variable density, with a vertical thickness of 26 radiation lengths and 11 interaction lengths.

High energy cosmic rays interact with the atmosphere and start the development of extensive air showers (EAS), this is a process of truly multi-particle dynamics with frequent high energy hadronic and electromagnetic interactions taking place. At primary energies of $10^{15}\,eV$, about 10^6 particles reach sea-level. These are mostly photons and electrons plus some fraction of high energy muons and hadrons spread over an area of several hectares. Detectors are typically sampling 1% of this area, aiming to reconstruct as accurately as possible the direction (given by the shower axis), the energy and the nature (or mass) of the primary particle. The reconstruction is made on the basis of Monte Carlo simulation of EAS development in the atmosphere.

Two major experimental techniques are adopted. The first, and the most applied, is to build an array of sensors (scintillators, water Cerenkov tanks, muon detectors) spread over a large area. The detectors count the particle densities sampling the EAS particles hitting the ground. From the timed sampling of the lateral development of the shower at a given atmospheric depth one can deduce the direction, the energy and possibly the identity of the primary CR. The surface of the array is chosen in adequation with the incident flux and the energy range one wants to explore. Detector arrays designed to detect cosmic rays from the knee region up to the ankle, have a typical dimension of some hundreds of m^2 (KASKADE [30], EAS-TOP [31], CASA [37], HEGRA [32]), while detectors for highest energy cosmic rays are of the order of several Km^2 (AGASA [8], SUGAR [36], Yakutsk [35]).

To improve the EAS measurements in some case (DICE [33], BLANCA [34]), these arrays of sensors are completed with detectors that measure the Cerenkov light emitted by high energy electrons produced in the shower

development.

The second technique consists in the study of the longitudinal EAS development by detecting the fluorescence light produced by the interactions of the charged secondaries. The energy and the direction of the primary cosmic ray are reconstructed studying the shape and the motion of the fluorescence halo produced in the development of the high energy shower. As consequence of the small efficiency of the fluorescence effect ($< 1\%$), this technique is used mostly to detect cosmic rays with energy above $\sim 10^{18}\, eV$, and observation can only be done on clear moonless nights, which results in an average 10% duty cycle.

The first successful detectors based on these ideas were built by a group of the University of Utah, under the name of "Fly's Eye" [38] and used with the "Volcano Ranch Ground Array" [39]. A complete detector was then installed at Dugway (Utah) and started to take data in 1982. An updated version, High Resolution Fly's Eye (HiRes) [9], is presently running at the same site.

Two projects are currently under development (EUSO [40], OWL [41]) to make measurements of the cosmic rays fluorescence from the space; this should improve the portion of atmosphere covered by a single detector and also obtain a larger duty cycle.

The AUGER experiment [42] under construction in Argentina, is combining the two techniques; it is composed of an array of water Cerenkov tanks covering about $3000\, Km^2$ and several fluorescence detectors embedded in the large surface array.

These indirect methods of detection bear, however, a number of serious difficulties in the interpretation of the data and require detailed modelling of the EAS development and detector responses. Particulary, systematic effects caused by the employed high-energy interaction models and by inevitable fluctuations in EAS need to be considered.

Many different experiments made measurements of the cosmic rays spectrum through the observation of the EAS , a throughout review of these measurements is beyond the the scope of this discussion (see for example [20]), here we report on the features of the high energy cosmic rays as obtained from the measurements.

At present, in the *knee* region and beyond little is known about cosmic rays other than their all particle energy spectrum [57]. The fraction of heavy elements appears to continuously increase and there are hypothesis that the *knee* could be originated by the disappearing of the light elements [68].

Figure 1.13 shows the cosmic rays spectrum as measured by the KASKADE detector [30], the *knee* feature is clearly seen at about $10^{15}\, eV$. The change in the spectral slope is compared with the hypothesis of a decreasing H contribution to the cosmic ray flux with increasing energy, anyway no striking evidences exists to prefer it to other solutions [44].

In the energy range corresponding to the *ankle* feature, the composition

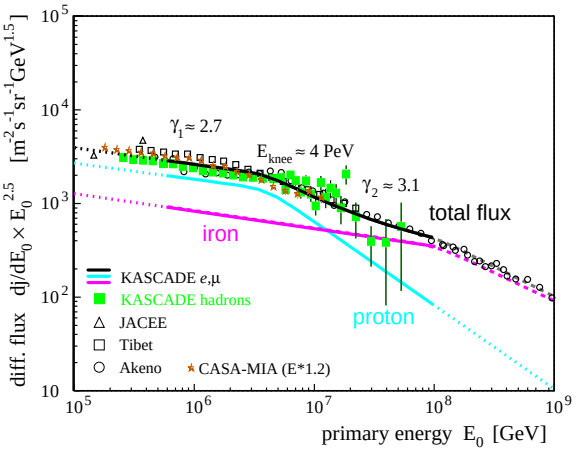

Figure 1.13: Cosmic ray spectrum in the knee region as obtained by different experiments. The lines represent KASKADE results based on simultaneous fits to electro and muon shower sizes assuming all particle spectrum to be a superposition of a proton and iron component. Figure from ref. [44].

seems to become light again [69] and the *ankle* could be interpreted as a transition to what appears to be mostly Hydrogen and Helium nuclei

At much higher energies it is not possible to prove unambiguously what the nature of this particles is.

Figures 1.14 and 1.15 shows the *ankle* region and the most high energy cosmic rays measurements from AGASA and from HiRes, the ankle feature is emphasized. No cutoff has appeared until now up to the highest observed energy.

No relevant anisotropy in the cosmic ray flux has been detected up to the ankle region, some hint for anisotropy above the ankle comes from AGASA (see fig. 1.14) and from other experiments [17, 18, 19], but the statistics collected is still to low for a clear statement.

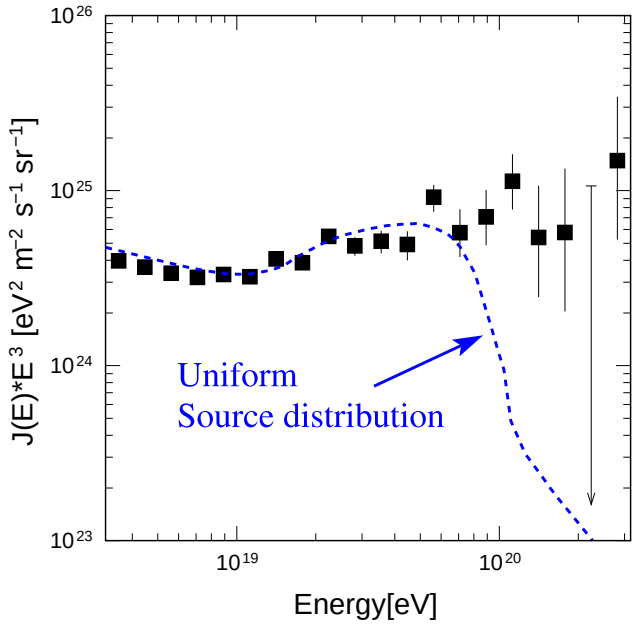

Figure 1.14: The AGASA energy spectrum including events with zenith angle up to 60°. The dashed curve is the expected energy spectrum for universal sources and includes the AGASA experimental resolution effects. Figure from [45].

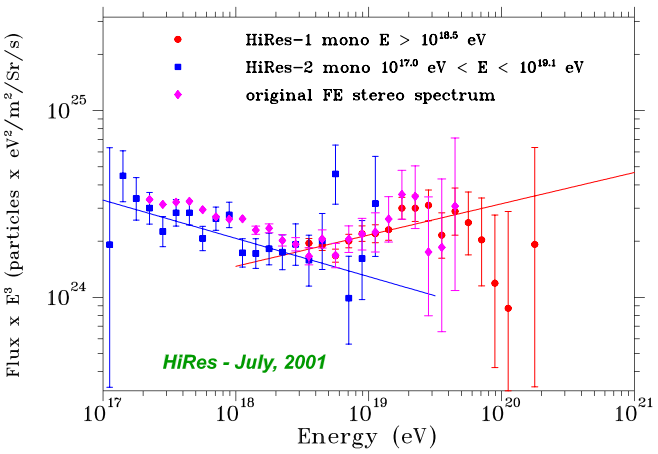

Figure 1.15: The HiRes cosmic rays spectrum. HiRes-1 has accumulated more running time than HiRes-2, giving it greater exposure for the highest energies. HiRes-2 has larger aperture angle at lower energies by virtue of its greater elevation angle coverage. Also shown is the earlier Fly's Eye spectrum.

1.3 The origin of cosmic rays

The interpretation of the observational data on CR flux energy spectra and composition near Earth is an astrophysical challenge. What we observe, in fact, is just the end of a quite long journey that these particles have done from their sources up to us in an interstellar medium filled of particles and fields. A careful modelling of the different ambient conditions and physical processes acting on cosmic particles all along their life is needed in order to coherently explain their characteristics directly observed in Earth proximity. In fig. 1.16 a simplified picture of the *life* of a generic CR from is ejection at source up to its arrival at Earth is presented. As depicted in figure, different processes act on the particles at the different steps of the journey modifying their original properties. We have already seen how geomagnetic effects and solar modulation affect the locally measured CR flux. At the galactic (extra-galactic) level, charged particles are diffused by weak galactic and planetary magnetic fields, so that any directional information on their origin is lost when they arrive to the Earth. The original CR composition is reprocessed during propagation by nuclear interactions in the interstellar matter. The energy spectra at sources are changed in the interaction with magnetic and electric fields, with a delicate interplay of energy losses and possible re-accelerations. Relative abundances of spallation products at Earth are interpreted in terms of the total amount of nuclear matter

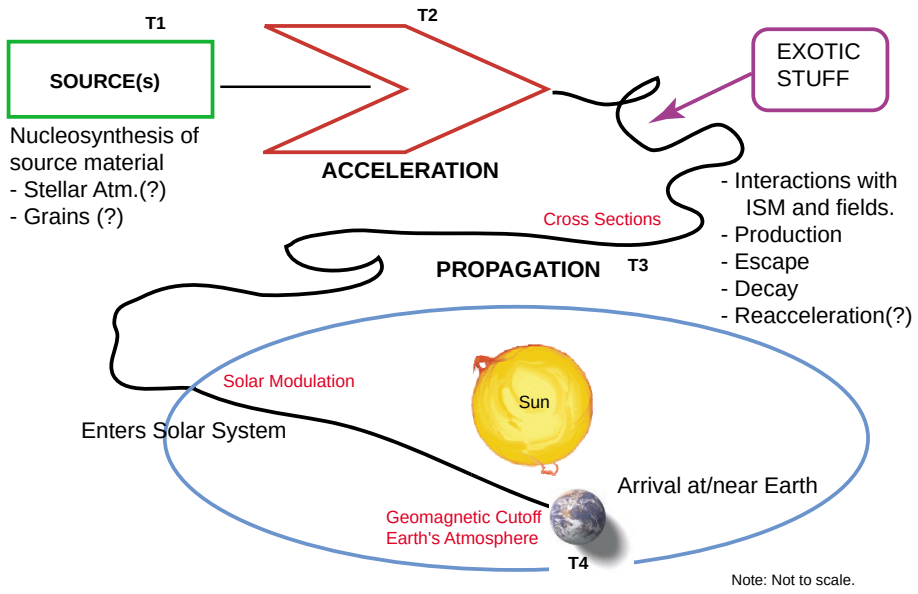

Figure 1.16: Sketch of the journey of a cosmic ray from the production site tho the Earth's atmosphere. Figure from [102].

traversed by parent species, while the ratio of unstable to stable isotopes are used to infer the propagation time. The power-law behavior of the CR energy spectra and changes in the spectral indexes are analyzed in terms of possible acceleration mechanisms and subsequent energy losses.

In the following we will briefly discuss actual models on CR sources, acceleration and propagation.

1.3.1 Cosmic rays sources

Galactic cosmic rays are believed to be predominantly produced inside our galaxy up to energies of $\approx 10^{19}\,eV$. A strong support to this hypothesis comes from the observed power-law spectrum for high energy electrons. Compton scattering with the Cosmic Microwave Background (CMB) would destroy this spectrum, were they produced at distances greater than $300\,kpc$.

The problem of determining the sources of the cosmic rays is one of the open questions of the astrophysics, the most favored theories are at moment concentrated on two basic ideas:

Low mass stars ejection Since low mass stars are very often observed to be very active, their contribution to cosmic rays injection via solar wind is expected to be substantial [27]. This is confirmed with the observation that the selection effects for the different elements among energetic particles are very similar in the solar wind and in the cosmic rays. In fact, in a few other stars these selection effects have been checked [28], [29].

Ionized dust particles In this model, the composition of the cosmic rays is explained as the result of the ionization of some dust particle and of the interaction processes within the dust itself. These kind of models have been developed by different groups [43], [46] giving in both cases a rather good explanation for the various abundances.

In any case the point is really open and the debate within the community is rich [47].

For what concerns the cosmic rays above $10^{19}\,eV$ they have gyroradii, in typical galactic magnetic fields, that are larger than the thickness of the galactic disk , and they are believed to be of extragalactic origin and might travel from their sources through intergalactic space almost undisturbed. Anyway there are also models that indicate the galactic halo as the source for cosmic rays above $10^{19}\,eV$ [58, 64, 65].

1.3.2 Cosmic rays acceleration

Galactic cosmic rays are believed to be accelerated via the so-called *diffusive shock acceleration*. Energetic particles are cycling back and forth across the

shock region, gaining energy each time they turn back; since the two sides of a shock are a permanently compressing system the particles gain energy. In a spherical shock the particles also lose energy from adiabatic expansion. Furthermore, in a system where the unperturbed magnetic field is perpendicular to the shock normal, particles can modify their energy by drifts, here dominated by curvature drifts; the particles move sideways in a curved magnetic field, and experience an electric field from the motion through a magnetic field; the component of the motion parallel to the perceived electric field leads to an energy change.

The energy enhancement due to the reflection is described as:

$$\frac{dE}{dt} = \frac{2V^2}{c\lambda}E = \alpha E \tag{1.2}$$

where λ is the mean free path ($\lambda = \rho\, c\, \tau \;\; g/cm^2$; ρ being the mean matter density and τ the mean time interval) between magnetic clouds, which are the sites of mirroring. This illustrates that the average increase in energy is only of the second order in V/c.

This process has enjoyed an enduring popularity since it predicts the power law energy spectrum of cosmic rays:

$$N(E) \propto E^{-\gamma} \;\; \gamma = \left(1 - \frac{1}{\alpha\tau_e}\right) \tag{1.3}$$

where τ_e is the mean time spent by a particle in the accelerating regions.

In the modern version of Fermi second order acceleration [72] the particles interact with various types of plasma waves and gain energy being scattered stochastically by these waves.

The cosmic rays below about $10^{13}\, eV$ are accelerated by the shocks originated in blast shockwaves of supernovae into the normal stellar medium [59].

The cosmic rays from $\sim 10^{12}\, eV$ up to the knee region ($10^{15}\, eV$), are very likely due to the explosion of massive stars into their former stellar winds [60]. The consequences of this concept have been checked by calculating the cosmic ray abundances and comparing them with observations [61]; the comparison suggest that up to the highest energy where abundances are known ($\sim 10^{13}\, eV$), this concept successfully explains the data. It is interesting that no mixing from supernova ejecta is required to account for the known cosmic rays abundances, Wolf Rayet winds and other strong stellar winds around evolved stars as sources are all that is needed.

For energies beyond the knee there is no consensus on the acceleration process; the simplest model proposes that the acceleration process through the supernova explosions is acting also in this energy range but with particles being accelerated by interaction with multiple supernova remnants as they move through the interstellar medium. This extended acceleration may take

particles up to $10^{18}\,eV$ with the higher-charge nuclei reaching the higher energies and become more dominant [67]. This idea is consistent with the limited evidence on mass composition $< 10^{18}\,eV$ and with the steepening of the energy spectrum near $10^{15}\,eV$. However there is yet no direct evidence of acceleration of protons by supernova remnants at any energy.

Another model proposes that a galactic wind termination shock might be able to accelerate cosmic rays to these energies [62]. Also hypothesis of extragalactic origin have been proposed [63], although the matching of the flux at the knee from two different source populations seems problematic.

For energies above the ankle region $\sim 10^{18}\,eV$, only hypothesis have been made. In the highest-energy region, not only deflection by the intergalactic magnetic field, but also the energy losses of cosmic rays in the intergalactic radiation fields, such as microwave, infrared, and radio backgrounds, become important. Soon after the discovery of the cosmic background radiation, Greisen [48] and Zatsepin and Kuzmin [49] predicted that there would be a cutoff in the spectrum of protons around $6 \times 10^{19}\,eV$ due to photopion production on the microwave background. This has become known as the GZK cutoff.

This cutoff is not seen: in fact, no cutoff is seen at any energy, up to the limit of data $\sim 10^{20}\,eV$. This is one of the most serious problems facing cosmic rays physics today. Assuming a not uniform source distribution, just as the observed galaxy distribution, alleviates the problem, but does not solve it [50], [51].

Particle between the *ankle* region and the expected (but not seen) GZK-cutoff are believed to come from pulsars with high magnetic field located outside our galaxy but there are also other proposals including the possibility they come from Gamma ray bursts [54].

Beyond the expected GZK-cutoff there is no argument whether this particles are really protons as an extrapolation from lower energies might suggest. Some generation and acceleration model has been proposed involving exotic processes like: decay of topological defects [55], decay of primordial black holes [56] and violation of Lorentz invariance [75].

1.3.3 Cosmic rays propagation

Cosmic rays propagating through the ISM from the sources to the Earth undergo several physical processes: diffusion along magnetic field lines and on the irregularities of the magnetic field, spallation reactions with the interstellar gas and radioactive decay. A model of the propagation of the cosmic rays through the galaxy should take in account all these process explaining how they contribute to the features of the cosmic rays fluxes observed at the Earth.

It has been recognized that the relevant physical propagation model to be used is the diffusion one [73, 74], though the so called leaky box model

has been widely preferred for decades because of its simplicity.

In the diffusive models cosmic rays are thought as a steady flux propagating in the galaxy, that diffuse following the density gradients presents in the galactic disk and in the halo.

The steady state differential density $N^j(E, \vec{r})$ of the nucleus j as a function of energy E and position $\vec{r}$ in the Galaxy, is given by [73]:

$$\begin{aligned} \nabla \cdot (K^j \nabla N^j - V_c N^j) - \frac{\partial}{\partial E}\left(\frac{\nabla \cdot V_c}{3} E_k \left(\frac{2m + E_k}{m + E_k}\right) N^j\right) \\ + \frac{\partial}{\partial E}(b^j N^j) - \frac{1}{2}\frac{\partial^2}{\partial E^2}(d^j N^j) + \tilde{\Gamma}^j N^j = q^j + \sum_{m_k > m_j} \tilde{\Gamma}^{kj} N^k \end{aligned} \tag{1.4}$$

The first terms represent diffusion (K^j is the diffusion coefficient) and convection (V_c is the convection velocity). The divergence of this velocity, expressed in the next term gives rise to an energy loss term connected with the adiabatic expansion of cosmic rays. Further, ionization and coulombian losses are taken in account, the energy loss coefficients are depending on the implementation of the model. The third term accounts for a possible reacceleration in first order derivative (all included in b^j). Finally a second order derivative in E for the associated second order term in reacceleration (d^j is the energy diffusion coefficient). These stand for the continuous losses. The last term of the left hand side takes care of the disappearance of the nucleus j ($\tilde{\Gamma}^j$ for short) due to its collisions with interstellar matter (ISM).

In the right hand side, the source term q^j takes into account the primary production and acceleration of nuclei described by an injection spectrum. Finally, the last term is for the secondary j sources, namely spallation contribution $\tilde{\Gamma}^{kj}$ from all other heavier nuclei. The notation used is E for total energy per nucleon and E_k for kinetic energy per nucleon. Quantities in this equation are functions of spatial coordinates (not time, steady–state being assumed) and of energy.

The general solution of eq. 1.4 requires to solve a triangular-like system for each nuclear species since only heaviest nuclei contribute to a given nucleus.

To compare calculations obtained with these models, to observations one has to take into account the effects of the solar wind on the particles in the heliosphere.

Chapter 2

Geomagnetic effects on Cosmic Rays

The magnetic field surrounding the Earth plays a key role in determining the properties of charged cosmic ray fluxes in the near Earth region. It modulates the intensity of the cosmic rays approaching to Earth and constraints the motion of the secondary particles produced in the interactions between the primary cosmic rays and the atmosphere.

In this chapter, we will illustrate the main features of the geomagnetic field briefly discussing the structure of the magnetosphere. The dynamics of charged particles in a dipole magnetic field will be then reviewed to introduce the mechanisms of geomagnetic cutoff and magnetic trapping. The formalism used to apply the results from the dipole field model to the realistic geomagnetic field will be finally discussed.

2.1 The Earth's magnetic field

The Earth, as other planets in the solar system[1], is generating a magnetic field. The geomagnetic field is originated in the mantle part of our planet, great differences in temperature and chemical composition generate strong density gradients that create ascensions currents in the magma. Combined with the rotation of the Earth these currents generate a set of convection cells that through a dynamo effect are believed to produce the geomagnetic field. Recently an experimental setup succeeded in reproducing such dynamo effect confirming this picture [78]. The geomagnetic field is characterized by secular variations. Geological measurements show that the Earth's magnetic field reversed its polarity hundreds of times, the mean interval between the inversions being about 500.000 years. In the last 50 years measurements have been collected regularly with increasing precision, revealing an yearly

[1] Jupiter, Mars and Saturn have a magnetic field, Venus instead is not generating any magnetic field

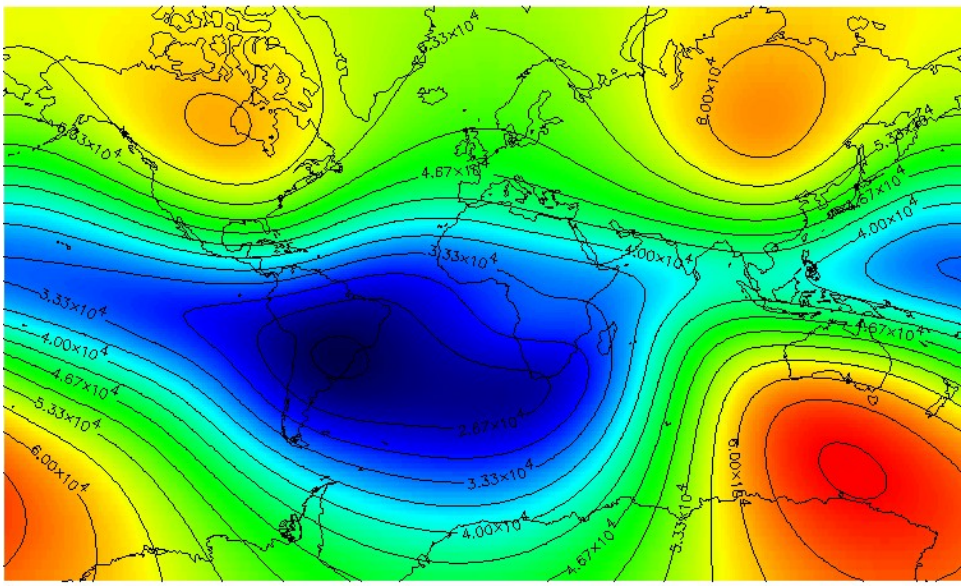

Figure 2.1: Geomagnetic field map on Earth's surface, Mercatore projection. Field values are expressed in nT for 1998 epoch.

weakening of the field intensity of 0.07% and a westward drift of $\sim 0.2°/year$ of the magnetic field configuration over the Earth's surface.

This field can be described, at first order, as a magnetic dipole tilted with respect the rotation axis of $\sim 11.5°$, displaced by $\approx 400Km$ with respect the Earth's center and with a magnetic moment $M = 8.1 \times 10^{25}\ G\,cm^3$. The dipole orientation is such that the magnetic south pole is located near the geographic north pole, in the Greenland, at a latitude 75° N and longitude 291°. The magnetic north pole is instead near the geographic south pole, on the border of the Antarctica. Figure 2.1 shows the field map at the Earth surface. The intensity at the Earth's surface varies from a maximum of $\sim 0.6G$ near the magnetic poles to a minimum of $\sim 0.2G$ in the region of the South Atlantic Anomaly (SAA), in between Brazil and South Africa. The complex behavior of the equipotential field lines is mainly a consequence of the offset and tilt.

2.1.1 The geomagnetic coordinates

The simplest description of a purely dipolar field is obtained in cylindrical coordinates referred to the system defined in fig. 2.2. The components of the field are:

$$B_r = -\frac{M}{r^3} 2 \sin\lambda\ ;\ B_\lambda = \frac{M}{r^3} \cos\lambda \tag{2.1}$$

Figure 2.2: Geomagnetic spherical coordinates and dipolar field line structure.

and the field lines have the form :

$$r = r_0 \cos^2 \lambda \tag{2.2}$$

The B intensity along each field line is expressed as:

$$B(\lambda) = \frac{M}{r_o^3} \frac{\left[4 - 3\cos^2 \lambda\right]^{1/2}}{\cos^6 \lambda} \tag{2.3}$$

It reaches its minimum value $B_0 = M/r_0^3$ on the equatorial plane (λ=0) at the largest from the dipole center $r = r_0$. This equatorial radius r_0 of the field line is often expressed in units of Earth Radii (R_E), introducing the dimensionless parameter $R_0 = r_0/R_E$. The intersection of a field line with parameter R_0 with a sphere of radius R_E centered in the origin of the dipole is simply given by:

$$cos^2\lambda = \frac{R_E}{r_0} = \frac{1}{R_0} \tag{2.4}$$

R_0 completely determine the field line and can be used as independent parameter to characterize the dipolar field.

Corrected geomagnetic (CGM) coordinates (latitude and longitude) were developed by Gustafson ed al. [80]. The main purpose is to develop a coordinate system so that the dipole field theory can be applied to realistic distorted field by still using corrected longitude and latitude.

CGM coordinates of a point A in space, by definition are calculated tracing the geomagnetic field-line passing in A to the dipole geomagnetic equator (B), then returning to the same altitude along the dipole field line and assigning the obtained dipole longitude and latitude (A_M) as the CGM coordinates of the starting point (fig. 2.3). At near-equatorial region the magnetic field lines may not reach the dipole equator and, therefore, the standard definition of CGM coordinates is irrelevant. There an approach based on a B minimum value along the given magnetic field-line is applied to define the CGM coordinates. This approach is discussed in detail in [80].

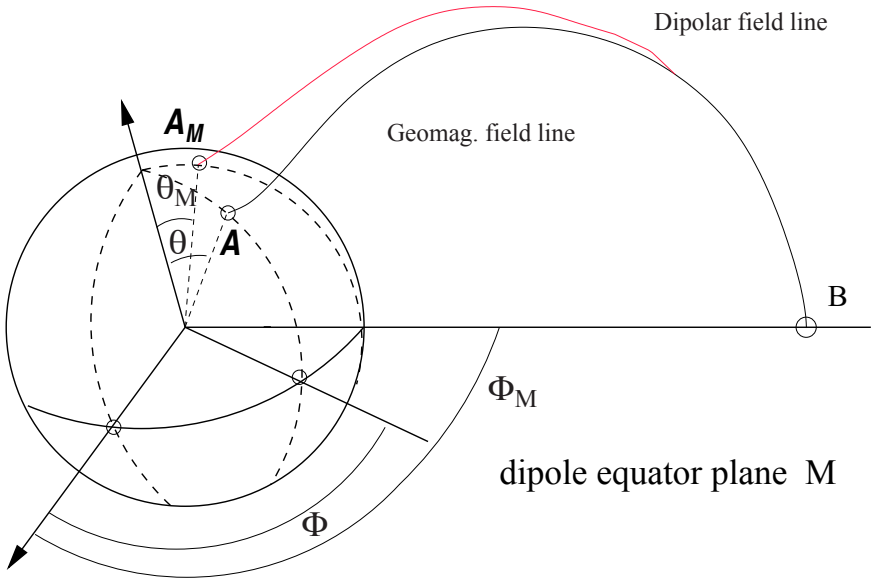

Figure 2.3: The definition of corrected geomagnetic coordinates.

By these definitions, the relation of altitude and latitude found in the dipolar case, can be preserved and magnetic field lines are parallel to the CGM meridians. The CGM-longitude is shifted from geographic longitude by approximately 71° depending on CGM-latitude. For the latitude, the formula $R = R_0\ cos^2\theta_{dipole}$ where R_0 is the altitude at equator and θ_{dipole} is the dipole latitude, is replaced by the more realistic one:

$$R = L\ cos^2\Theta_M \tag{2.5}$$

where L is the McIllwain L-parameter [88] and Θ_M is the CGM-latitude.

2.2 The interaction with the solar wind

The Earth's magnetic field is immersed into the solar wind, a steady flux of charged particles that outgoes from the Sun.

Interacting with the geomagnetic field, the solar wind generates a set of structures which defines the magnetosphere. The general features of this phenomenon can be treated very well by the hydrodynamic theory, in this sense we can look at the geomagnetic field like an obstacle into the propagation of the fluid called solar wind, just like a big stone in a mountain river.

Figure 2.4 is showing the structures constituting the magnetosphere.

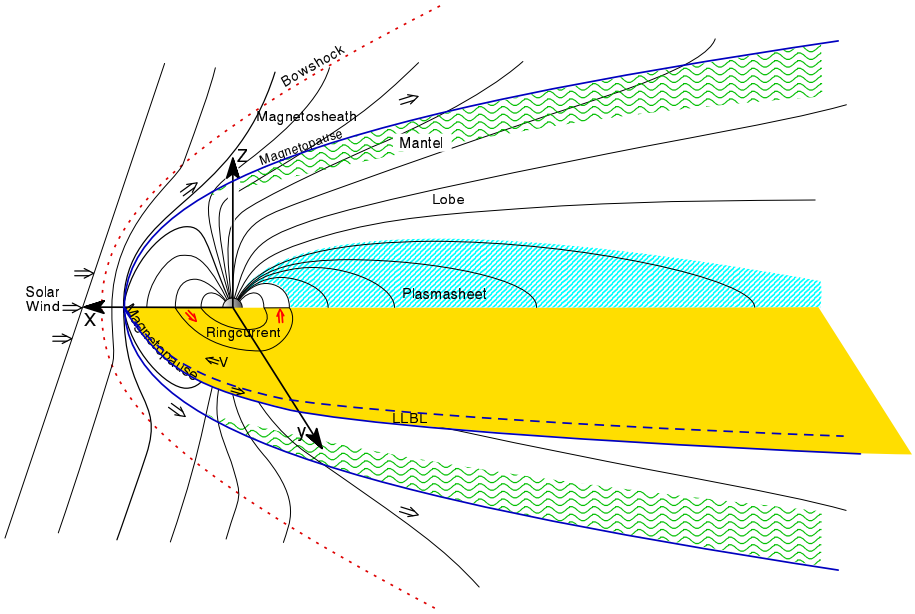

Figure 2.4: Sketch of the magnetosphere structures.

Currents of solar wind charged particles are following the paths created by the shock boundaries, these currents are generating an additional magnetic field (external component) that sums to the Earth generated field (internal component) into the magnetosphere field. Figure 2.5 is showing the ratio (open squares) between the external and the internal component as function of the distance from the Earth. The two components become equal in at $\sim 10\,R_E$, the magnetopause zone.

The size and the shape of the magnetosphere depends on the solar activity, on the distance Sun-Earth, and can be heavily modified during energetic solar events (magnetic storms).

2.3 Charged particles in the geomagnetic field

The dynamics of a charged particle in a magnetic field is the consequence of the Lorentz force:

$$\frac{d\mathbf{p}}{dt} = Z\,e\,\mathbf{v} \times \mathbf{B} \tag{2.6}$$

where $\mathbf{p}$ is the particle momentum, e the electron charge, Ze the charge of the particle, $\mathbf{v}$ the particle velocity and $\mathbf{B}$ the local magnetic field. To describe the motion of a particle in a magnetic field it is useful to introduce the definition of rigidity as the momentum divided by the total charge: $\mathbf{R} = \mathbf{p}/Ze$. Expressing the momentum in GeV/c units one obtains a rigidity expressed in GV/c (Giga Volts over c) units.

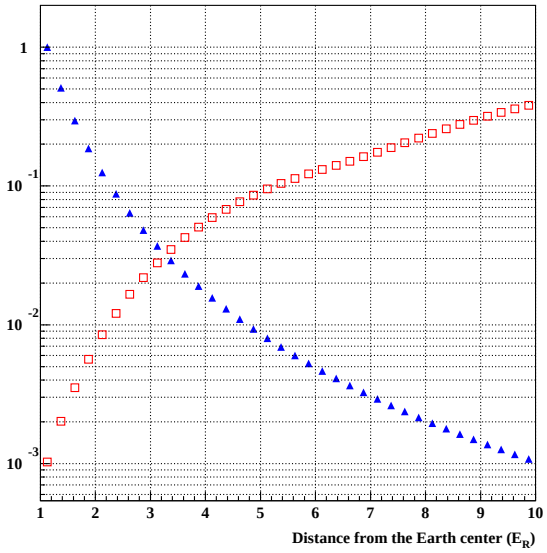

Figure 2.5: Blue triangles represent the intensity of the internal field as a function of the distance from the Earth's center. The intensities are referred to the value at 1 R_e, i.e. at the Earth's surface. Open red squares are showing the fraction of external field with respect the total.

For an arbitrary B field configuration, the general solution of the motion equation 2.6 does not admit a closed form and its numerical integration is needed to evaluate the characteristics of the particle's motion. Even in a simple dipolar field, different degrees of complexity arise in the description of the motion of a particle depending on the initial conditions. However, in this case, the symmetries in the field configuration allow for a relatively simple definition of different regimes in the particle's motion which can be used to understand the major geomagnetic effects on near Earth radiation environment.

Charged particles in dipolar magnetic field can follow three kind of trajectories:

Unbounded These are trajectories that are starting far away from the field source (mathematically at infinity), then approach the source of the field, being deflected, and at the end are reaching again a great distance from the source.

Bounded These are trajectories that remain confined within a maximal distance from the dipole center.

Semi-bounded These are trajectories that starts from infinity, approach the field source and remain confined within a maximal distance from

the dipole center (Semi-bounded in the future). In the case the trajectory is followed from the bounded part to the infinity it is called Semi-bounded in the past. The phase-space configurations for this kind of trajectories are very rare.

Unbounded trajectories are followed by most of the incoming cosmic ray particles in their approach to Earth. The geomagnetic shielding acting on low energy cosmic rays can be effectively described in terms of the *allowed* or *forbidden* trajectories for the access of CR to the Earth.

Bounded trajectories are followed by most secondaries produced in atmosphere and the relatively low energy particles injected by means of different mechanisms in the magnetosphere. We are particularly interested in the periodicities appearing in the bounded motion of these particles under some simple approximations.

Semi-bounded trajectories can be followed by either primary CR or atmospheric secondaries for very peculiar initial conditions.

2.3.1 The geomagnetic cutoff

Experimental evidence for a modulation of the cosmic ray flux as a function of the geomagnetic latitude dates to the '30s [81]. Qualitatively, the effect is easily understood when considering the B field line configuration with respect a geocentered spherical surface. At magnetic equator, the B field lines run nearly parallel to the spherical surface, while at the poles they encounter the surface at nearly normal incidence. In the polar region, low energy charged particles can therefore reach the surface following the field lines, while in the equatorial region the same particles would be deflected by the Lorentz force. In particular, above 78° in geomagnetic latitude, geomagnetic field lines are connected with the magnetopause region and the geomagnetic cutoff effect disappears. In these conditions low energy solar wind particles reach the Earth atmosphere and form the aurora borealis.

Quantitatively, the question of charged particle access to a given location coming from infinity can be formulated either in a *direction* or in a *rigidity* picture [85]. In the first case, the access of a particle with a specific rigidity is studied as a function of its direction of arrival. A complementary study, i.e. the access along a specific direction as a function of the rigidity of the particle, is the basis of the second approach.

The peculiar result of the *direction* picture in a dipolar field is a net separation of the whole solid angle around any given location of the field in three separate regions characterized by full, partial and no access. This is better explained with the help of fig. 2.6 relative to a positive charged particle with an arbitrary rigidity value. The reference system (fig. 2.7) has its origin in an arbitrary position of the field with a vertical axis along the zenith direction. The horizontal axis is defined perpendicular both to the

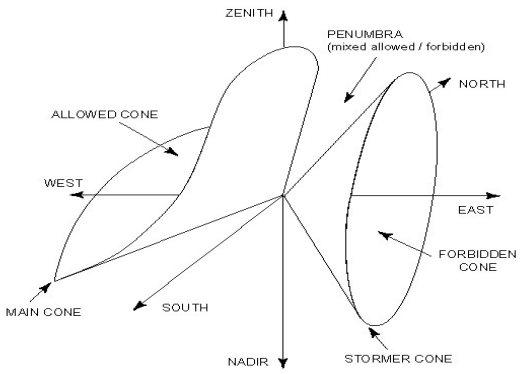

Figure 2.6: Representation of the full, partial and no access regions in a generic point of the geomagnetic field for a positively charged particle with an arbitrary rigidity [85]. See text for more details.

zenith and the dipole axis, in the East-West direction with respect the local B field.

On the right side of the picture, the *Störmer cone* defines the region of no access at that given point. A positively charged particle with that specific rigidity can not reach that point from infinity along any of the directions (*forbidden* trajectories) enclosed in the Störmer cone. The existence of this cone is a general property of any axially symmetric field and, at any field location and for any particle rigidity, the axis of this cone lies in the E-W direction, opening to the East for positively charged particles and to the West for negatively charged ones.

On the left side of the picture, the *main cone* defines the angular region of full access. A positively charged particle with that specific rigidity can reach that point from infinity along all directions (*allowed* trajectories) enclosed in the main cone. Opposite as for the Störmer cone, the orientation and the effective shape of the main cone can significantly vary with the particle rigidity and the considered geomagnetic location.

A mix of allowed and forbidden trajectories corresponds to the directions out of the two cones: this is the *penumbra* region. There, only a partial access to the point is possible due to the presence of a solid earth which intercepts part of the trajectories corresponding to arrival directions outside the Störmer cone.

In the penumbra, the possibility for a positively charged particle to enter the field in that location should be evaluated in each direction by the full integration of the corresponding trajectory.

The logical step towards a *rigidity* approach to the problem is done by considering how the above picture changes for different particle rigidities.

At a given location, the angular opening of the Störmer cone and the

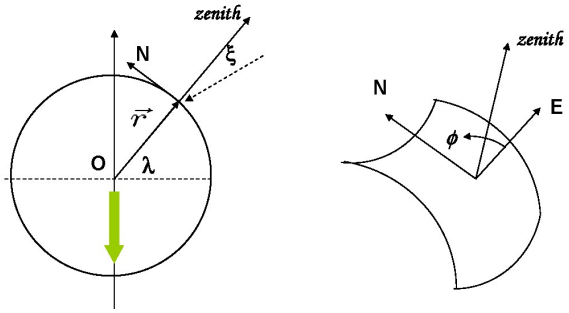

Figure 2.7: Definition of the spherical geomagnetic coordinates (r, λ) and of the local geomagnetic reference system ($East$, $North$, $Zenith$). The arrival direction of a particle in a point P is described by the polar angle ξ to the zenith and the azimuthal angle ϕ with respect local East.

shape and orientation of the *main* cone are a function of the rigidity of the particle. For increasing values of the rigidity, the looser bending effect of the magnetic field naturally results in a widening of the region delimited by the main cone and in a reduction of the opening angle in the Störmer cone. For a given direction of arrival, there will exist a minimum value of the particle rigidity for which the Störmer cone opens up to include that direction. This rigidity value defines the *Störmer rigidity cutoff* (R_S): all particles with a rigidity $R \leq R_S$ are forbidden to enter the field along that given direction. Analytically, the Störmer cutoff can be evaluated from the relation:

$$R_S = \frac{M \cos^4 \lambda}{r^2[1 + (1 \mp \cos^3 \lambda \cos \phi \sin \xi)^{1/2}]^2} \tag{2.7}$$

where M represents the dipole moment, the arrival location is defined by the geomagnetic coordinates (r, λ) and the arrival direction is defined by ξ and ϕ , respectively the polar angle from local zenith and the azimuthal angle counted clockwise from local magnetic East (fig. 2.7). The $\mp$ sign respectively applies to positively/negatively charged particles.

For vertical incidence ($\xi = 0$), the azimuthal dependence of the cutoff simply vanishes putting in evidence the cutoff behavior with latitude :

$$R_S = \frac{M \cos^4 \lambda}{4r^2} = \frac{59.6 \cos^4 \lambda}{4r^2} \, GV/c \tag{2.8}$$

where r is expressed in units of earth radii. The cutoff is maximum (minimum) at the magnetic equator (poles) with a ≈ 15 GV/c (null) value at the Earth's surface.

For an arbitrary ξ, the cutoff is larger for positively (negatively) charged particles arriving from eastern (western) direction. At low energies this breaks the isotropy of the incoming cosmic ray flux, which - depending on the charge sign of the particles - exhibits an East-West asymmetry.

With the Störmer cutoff we can exactly define the minimum rigidity needed to access a magnetic location along a given direction. However, due to the *penumbra*, nothing guarantees that above the Störmer rigidity the access is always granted.

2.3.2 Bounded trajectories and trapped particles

The complex dynamics of charged particles geomagnetically bounded at a finite distance from Earth finds a relatively simple description when treated in the framework of the Adiabatic Theory. This is possible under the assumption that any variation of the B field along the motion of a given particle occurs *adiabatically*, i.e. with large spatial and temporal scales with respect the instantaneous characteristics of the motion. Then, the B field lines define the proper frame to which refer the particle's motion which is analyzed in terms of three distinct components: the gyration around the B field lines and the displacement parallel and normal to the B field lines.

The first space/time scale that enters in this description is given by the circular motion of the particle in the plane orthogonal to the field.

In an uniform B field, the solution of eq. 2.6 leads to a uniform motion along the field line and an uniform circular motion in the orthogonal plane with a *cyclotron* radius:

$$\rho_c = \frac{p_\perp}{Ze\,B} = \left(\frac{m_0\gamma}{Ze}\right)\frac{\beta c}{B}\sin\alpha = \left(\frac{m_0\gamma}{Ze}\right)\frac{v_\perp}{B} \tag{2.9}$$

and a *cyclotron* period :

$$\tau_c = \frac{2\pi\rho_c}{v_\perp} = \frac{2\pi m_0\gamma}{Ze\,B} \tag{2.10}$$

where $p_\perp$ and $v_\perp$ are the momentum and velocity orthogonal to the B field, m_0 is the rest mass of the particle, β and γ the relativistic velocity and the Lorentz factor and α the pitch angle defined as the angle between the momentum vector and the field.

A clockwise (anti-clockwise) spiralling motion is followed by positive (negatively) charged particle as a result of a circular motion around a center which moves with constant velocity on the field line.

When dealing with non uniform or time dependent magnetic fields, we can still assume that the motion can be described as the superposition of an approximately circular gyration around a *guiding center* and a displacement of the *guiding center* itself, provided that the B field variation along the cyclotron motion are small enough :

$$\rho_c\frac{\nabla_\parallel B}{B} \ll 1 \;,\; \rho_c\frac{\nabla_\perp B}{B} \ll 1 \;,\; \tau_c\frac{1}{B}\frac{dB}{dt} \ll 1 \tag{2.11}$$

where $\nabla_\parallel B$ and $\nabla_\perp B$ represent the variation of the B intensity in the parallel and perpendicular directions to the field line. The two conditions on $\nabla_\parallel B$

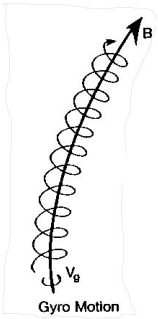

Figure 2.8: Example of gyromotion along a field line.

and $\nabla_\perp B$ are separately needed in order to apply this approach to the motion along and across the field lines.

The particle position at a given instant is then defined by the position of the guiding center $\overrightarrow{r_G}$ in an inertial reference frame (IFR), and by the phase ξ of its circular orbit perpendicular to the magnetic field in the Guiding Center Reference frame (GCR). The particle's motion is described by the the guiding center, dropping the detailed information on the phase ξ, while the actual values of ρ_c and τ_c are needed to evaluate the validity of the approach in each specific case.

As long as this description is valid, it can be easily demonstrated (see [84]) that the magnetic moment μ associated to the particle's cyclotron motion in the GCR is conserved:

$$\mu = iA = \frac{Ze}{\tau_c}\pi\rho_c^2 = \frac{p_\perp^2}{2m_0 B} = \text{const} \tag{2.12}$$

where $p_\perp^2$ is the particle's momentum orthogonal to the B field in the cyclotron motion, i.e. the p^* momentum in the GCR frame. μ is often referred as the *first adiabatic invariant* of the motion.

The motion of the guiding center along the field lines is the second component entering the adiabatic description of the particle's motion. This component is driven by the variation of the B intensity parallel to the field line ($\nabla_\parallel B$)

A variation of the B intensity along the field line ($\nabla_\parallel B$) corresponds to a variation of magnetic flux through the cyclotron orbit of the particle, i.e. through a current loop, and induces an electrical field, according the Faraday's law. The work done on the particle by the electrical field over a cyclotron orbit is:

$$W = Z\, e\, \pi\, \rho_c^2\, \frac{\Delta B}{\tau_c} = \frac{\gamma m\, v_\perp^2}{2}\, \frac{\Delta B}{B} \tag{2.13}$$

This corresponds to a variation in the kinetic energy relative to the cyclotron motion. Since the total energy is conserved by the magnetic force, an op-

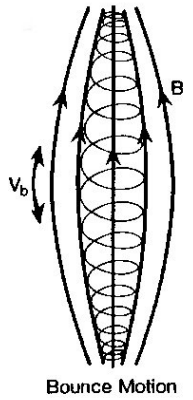

Figure 2.9: magnetic mirroring.

posite change occurs in the kinetic energy relative to the motion parallel to the field line. If the motion is towards a region of increasing (decreasing) B intensity, $p_{\|}$ will decrease (increase) irrespective of the charge sign of the particle. From the magnetic moment conservation (2.13) and expressing $p_{\perp} = p \sin\alpha$ we have:

$$\frac{2m_0\mu}{p^2} = \text{const} = \frac{sin^2(\alpha)}{B} \tag{2.14}$$

We can therefore express the value of the momentum parallel to the field line at an arbitrary position s along the field line as:

$$p_{\|}(s) = p\cos\alpha(s) = p\left[1 - \frac{B(s)}{B_i}\sin^2\alpha_i\right]^{1/2} \tag{2.15}$$

where $B(s)$ and $\alpha(s)$ are the field intensity and the pitch angle as a function of s, the arc length along the field line, and B_i and α_i are the values of the same quantities at the arbitrary initial position s_i. The $p_{\|}$ component will vanish for a B field intensity:

$$B_m = \frac{B_i}{\sin^2\alpha_i} \tag{2.16}$$

This condition corresponds to a magnetic *mirroring* of the particle's motion: the particle is driven back along the field line by the $\nabla_{\|}B$. If a minimum in the B field intensity can be defined along the field line, then the particle will be magnetically trapped and will persist in a *bouncing motion* between two mirror points defined by the condition 2.16. It should be noted that the location of mirror points, i.e. the geometry of the *bouncing*, is independent of the nature and velocity of the particles, being completely defined by the geometry of the field and the initial combination of position (B_i) and pitch angle (α_i).

The period of the bouncing motion is defined as:

$$\tau_b = 2\int_{s_m}^{s'_m} \frac{ds}{v_{\parallel}(s)} = \frac{2}{v}\int_{s_m}^{s'_m} \frac{ds}{\left[1-\frac{B(s)}{B_m}\right]^{1/2}} \gg \tau_c \tag{2.17}$$

and is naturally much larger than the gyration period.

If the variations of the B field encountered during a bounce period are satisfying the condition:

$$\tau_b \frac{1}{B}\frac{dB}{dt} \ll 1 \tag{2.18}$$

a second adiabatic invariant can be defined as the path integral:

$$J = \oint p_{\parallel} ds = \oint p\cos\alpha ds = 2p\int_{s_m}^{s'_m} \left[1-\frac{B_m}{B_s}\right]^{1/2} ds = 2pI \tag{2.19}$$

This is an adiabatically conserved quantity along the bouncing motion, and for a given particle's momentum is completely defined by the structure of the field, represented by the so-called *Eye* integral I entering in its definition 2.19.

The *drift* motion of the guiding center in the direction orthogonal to the field is the third component entering the adiabatic description of the particle's motion. This is produced by two separate mechanisms. The so-called *gradient* component of the drift can be ascribed to the presence of the B intensity variation in the direction orthogonal to the field line ($\nabla_{\perp} B$). During gyration, the particle systematically experiences a stronger (weaker) field intensity in the part of its orbit along (opposite) to the $\nabla_{\perp} B$ causing an alternate change of its Larmor radius and therefore a drift of its orbit in the direction orthogonal both to the field and the $\nabla_{\perp} B$. The so-called *curvature* component of the drift can be described in terms of the centripetal force needed to drive the particle's motion along a curved field line. This is felt by the gyrating particle in the GCR frame as an inertial (centrifugal) force orthogonal to the field causing a drift of the cyclotron motion in the direction orthogonal both to the centrifugal force and to the field, i.e. in the same direction of the *gradient* drift. The *gradient-curvature* drift velocity can be expressed as:

$$\mathbf{V_D} = \mathbf{V_C} + \mathbf{V_G} = \frac{mv^2}{2ZeB^3}(1+cos^2\alpha)\,\mathbf{B}\times\mathbf{n} = \frac{E_k}{Ze\,B^3}(1+cos^2\alpha)\,\mathbf{B}\times\mathbf{n} \tag{2.20}$$

where E_k is the kinetic energy of the particle and $\mathbf{n}$ is the direction normal to B. It should be noticed that the charge of the particle explicitly enters in the V_D definition, positively (negatively) charged particles will have opposite drifting directions.

This third component of the motion is again related to a static or slowly varying B field with respect the characteristic time, τ_D, needed to complete

a full drift around the dipole:

$$\tau_D \frac{1}{B}\frac{dB}{dt} \ll 1$$

and it is associated to the conservation of the magnetic flux through the surface enclosed by the particle motion, *the third adiabatic invariant*.

The decomposition of the particle motion in the three components described, it is possible if the frequencies of the three different motions are well separated:

$$\omega_C \ll \omega_B \ll \omega_D$$

where ω_C is the cyclotron motion frequency, ω_B is the bouncing motion one and ω_D is the frequency of the drift motion. Under this condition no resonances are present between the different components of the motion, and the three adiabatic invariants are conserved. As discussed in ref. [82], in a quasi-dipolar field, like the one of the Earth, the most dangerous resonances are these between the cyclotron rotation (ω_C) and the longitudinal bouncing (ω_B), since in the geomagnetic field the relations: $\omega_C, \omega_B \ll \omega_D$ are always satisfied [87]. As consequence it is possible to define an adiabaticity (or smallness) parameter:

$$\chi_e = \frac{\omega_B}{\omega_C} \tag{2.21}$$

and a maximal value (χ_c) of this parameter below which the motion can be described using the adiabatic invariant approach. Theoretical estimates of the maximum value of χ_e allowed for a trapped orbit settles around $\chi_c \simeq 0.3$ [86].

The global motion of a charged particle trapped in the geomagnetic field will be then a *sum* of the three components discussed above as depicted in fig. 2.10: the guiding center of the particle will move on a surface - the drift shell - generated by the different field line segments followed at different drift times in the bouncing motion. As it can be seen in figure 2.10, the characteristics of the *drift shell* are fixed by the geometry of the field lines and the location of mirror points along them as determined by the condition 2.16.

In the dipolar case, the shell geometry is particularly simple and can be obtained by a full rotation around the dipole axis of an arbitrary field line segment fully contained in a meridian plane. The field line segment is univocally defined in terms of its equatorial distance from the dipole center (r_0) and the latitude of mirroring (λ_m), which will be the same in the northern and southern hemispheres.

On different field lines this will correspond to a distance of the mirror points from the dipole center:

$$h = r_0 cos^2\lambda_m = R_0\, R_E\, cos^2\lambda_m \tag{2.22}$$

In the ideal case of a perfect dipole with no solid earth, the shells will be therefore closed and defined by a couple of parameters (r_0,α_0) or equivalently (r_0,B_m).

The same formalism can be applied for the nearly-dipolar realistic field, using an operative definition of the shell parameters which takes into account the exact field properties. In this more general case the shell parameters are: the *McIllwain equivalent equatorial radius* L [88] and $B_m(\alpha_0)$

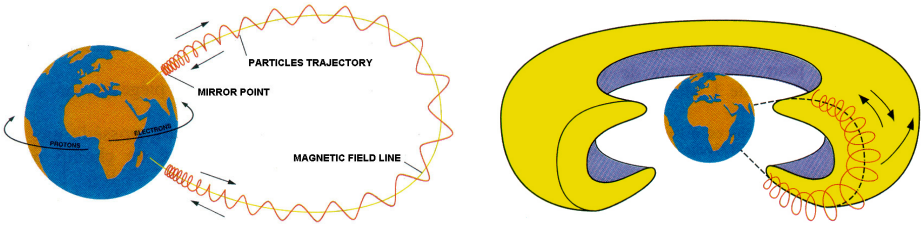

Figure 2.10: Components of the motion of a charged particle trapped in the geomagnetic field

A major change in the above picture is given by the introduction of the solid Earth. The shells are *opened* in correspondence of their intersections with the earth surface and the resulting structures reflect the offset of the dipole momentum with respect to the Earth rotation axis.

This is depicted in fig. 2.11. The shell shape and the altitude of the mirror points along the shell are represented for distinct (L, B_m) values. The altitude is referred to the Earth's surface.

A closed shell is presented in the uppermost plots. The distorted shape of the drift surface corresponds to the realistic description of the geomagnetic field. All mirror points lie above the Earth atmosphere (represented by the shaded area up to $\sim 100km$), so that a particle injected on this shell will be indefinitely trapped in the geomagnetic field moving along the shell surface.

An open shell is presented in the middle plots. In this case, most of the mirror points are lying below atmosphere. Atmospheric secondaries will be injected all along the shell but will also be reabsorbed soon after, in at most one or two bounces. Their residence time out of the atmosphere will be small (O(10^{-2} s)) and representative of the characteristic bouncing time (τ_b).

Another open shell is presented in the bottom plots. Its mirror points are lying below atmosphere only in the region of weakest field intensity, i.e. around the SAA. Atmospheric secondaries will be injected on this shell just in that region and will be able to perform nearly a complete drift around Earth before being reabsorbed. Even if not stably trapped, they will *live* for a relatively long time O(τ_D) in orbit around the Earth.

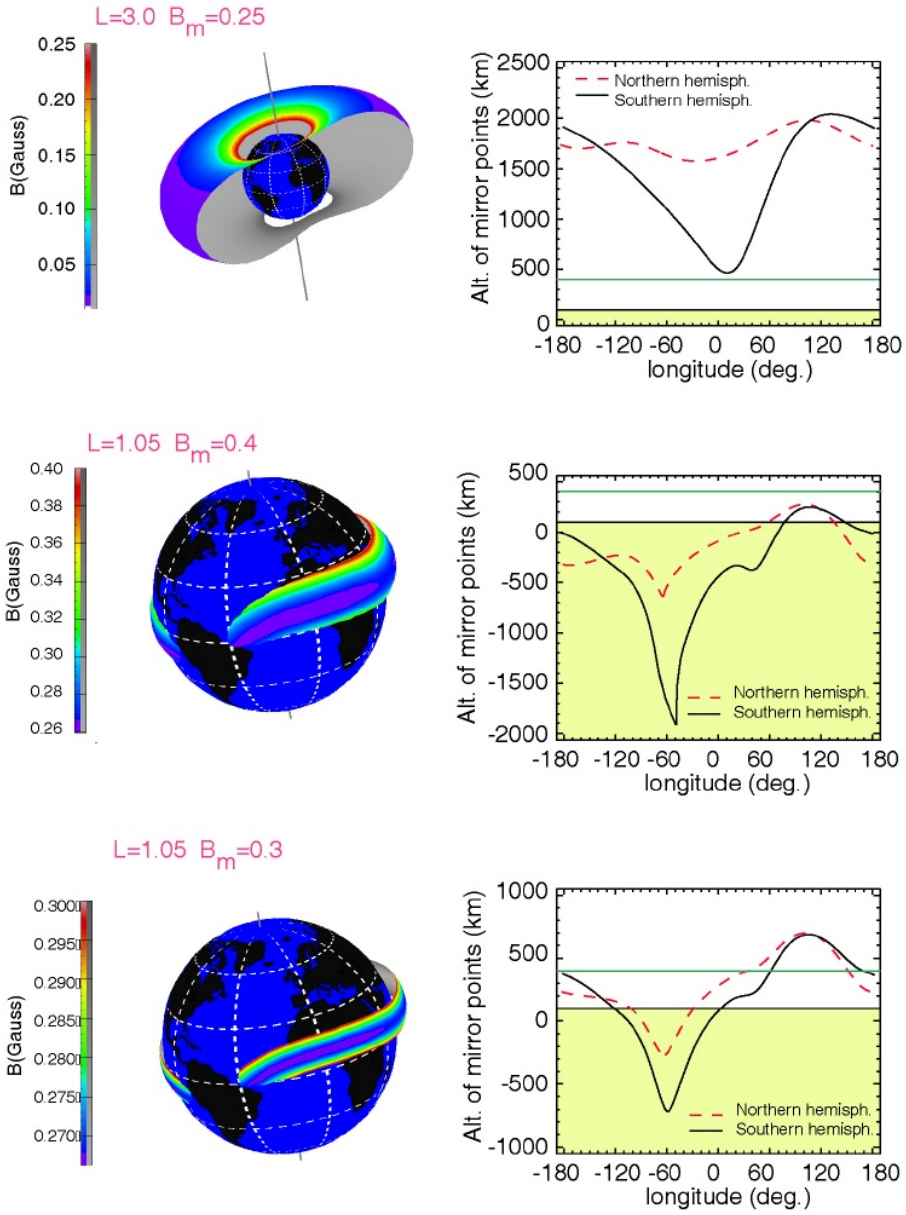

Figure 2.11: Examples of shells. Left figures are representing from top to bottom, examples of closed shells, short lived open shells and long lived open shells. Right plots are representing the altitudes of the mirror points in the northern (solid line) and in the southern (dashed line) hemispheres versus the geographic longitude. The limit of the shaded area represent the atmosphere limit, the horizontal solid line the AMS orbit altitude. Figures obtained with the SPENVIS online tool [83].

Chapter 3

The Monte Carlo simulation

The simulation of the cosmic ray interactions with the Earth's atmosphere and magnetosphere is a complex task that requires to combine models describing different features of the near Earth environment together with the models of the physics processes cosmic rays are subjected to.

In this chapter, we review all the elements used in this simulation discussing the adopted solutions. In our model of the near Earth environment, a flux of galactic cosmic rays is isotropically generated over the whole Earth. The Earth is represented as a solid sphere completely absorbing any particle incident on its surface and surrounded by a 120 km thick atmosphere. A perfect vacuum zone extends from the top of the atmosphere up to a distance of ~ 10 Earth's Radii (R_E) where another region of perfect absorber encloses our little universe (fig. 3.1). Magnetic field fills the atmosphere and the surrounding vacuum driving the motion of charged cosmic rays and atmospheric secondaries. Hadronic and electromagnetic processes in atmospheric interactions of the incident cosmic rays are fully treated by means of an up-to-date and widely used Monte Carlo code.

In the following, we will first illustrate how the cosmic ray flux is generated and what is the assumed primary flux. We will then describe the model of the magnetic field and discuss the tracing technique used to follow the particle motion within. We will end the chapter with a description of the model of the atmosphere and the characteristics of the Monte Carlo code used to simulate the interactions.

3.1 The event generation

The ideal approach in the generation of the primary cosmic rays flux would be to start with an isotropic distribution of particles at a great distance from the Earth (typically $10\,R_E$) where it is reasonable to assume that the geomagnetic field introduces negligible distortions on the interstellar flux. This method is however intrinsically inefficient from the computational point

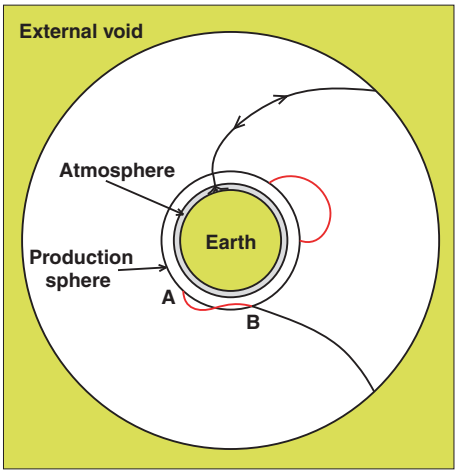

Figure 3.1: Sketch of the setup of the simulation. The Earth and the external void are made of a perfect absorbing material. The figure is out of scale

of view, since most of the particles are generated with trajectories which will not reach the Earth environment.

Kinematical cuts can be applied in order to improve the selection efficiency at generation, however they tend to introduce a bias for low rigidity particles.

A good alternative to this approach is the so called *backtracing method* already used, with some differences in [119]. The idea is that one can generate an isotropic flux near the Earth and then remove one by one the trajectories forbidden by the presence of the geomagnetic field.

In our implementation an isotropic flux is generated uniformly on a geocentered spherical surface with a radius of $1.07\,R_E$ ($\sim 500\,K\,a.s.l.$). Details on the composition and energy dependence of the flux and on its generation will be given in the next section. Only the trajectories pointing inside the spherical surface are considered, for each trajectory the time reversed trajectory is traced inverting the momentum direction and the charge sign. Depending on the satisfaction of one of these conditions an action is taken:

1. the particle reaches the distance of $10\,R_E$ from the Earth's center. Then it is a primary cosmic ray on an allowed trajectory, it is propagated forward and can reach the Earth's atmosphere.

2. the particle touches again the production sphere. Then it is a under cutoff particle on a forbidden trajectory or a primary cosmic ray on an allowed one already counted. In this second case the particle is discarded.

3. neither of the above condition is satisfied before a time limit is reached.

In this case the particle is discarded. This condition arise only for a small fraction of the events $O(10^{-6})$.

Under the two hypothesis that the flux at $10\,E_R$ (in our case) is isotropic and that there are no acceleration processes within $10\,E_R$ from the Earth, in the following is demonstrated that the first method and the backtracing one are equivalent.

Let us consider the effect of the geomagnetic field on an incoming flux of charged particles in the absence of a solid Earth. For the discussion we start with an isotropic flux of monoenergetic protons at large distance, i.e. at infinity, from the origin of a geocentrical reference frame. The realistic case of an energy spectrum can be treated just as a superposition of monoenergetic cases.

As already described in chapter 2, in this scenario three types of trajectory are possible: unbounded, bounded and semi-bounded trajectories; we neglect the semi-bounded trajectories for their very rare occurrence.

Unbounded trajectories cross a spherical surface centered in the field source only an even number of times, as shown in fig. 3.2 we call *legs* the trajectory parts connecting the spherical surface to infinity and *loops* the parts of the trajectory starting and ending on the spherical surface.

Since each trajectory can be followed in both directions and no source or sink of particles is contained within the surface, the incoming flux is the same as the outgoing.

The presence of the magnetic field breaks the isotropy of the flux *"near"* the field source, so for any given location on the spherical surface there is a flux dependence on the direction of arrival.

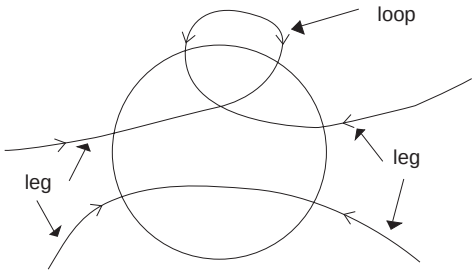

Figure 3.2: Trajectories types crossing a spherical surface

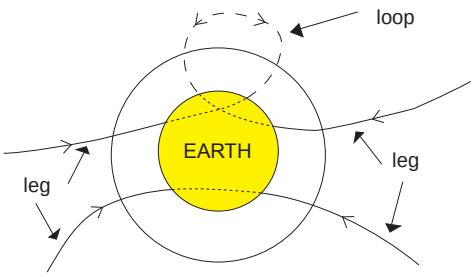

Figure 3.3: Trajectories in the presence of a solid Earth

Liouville theorem guarantees that the flux of primary cosmic rays on a given direction is the same as at infinity on the subset of directions matching the unbounded trajectories (allowed directions) and zero in the complemental set matching the bounded trajectories (forbidden directions) [91].

Being the flux isotropic at infinity all the allowed directions are carrying the same flux, so the problem of generating a realistic flux of primary cosmic

rays *"near"* the Earth reduces to the one of finding allowed directions.

The pattern of the allowed and forbidden directions depends on both the rigidity and the location and is the geomagnetic cutoff already described in chapter 2.

With the introduction of a solid Earth, all the trajectories that are crossing the Earth are broken in two or more pieces (fig. 3.3): the *legs* become one-way trajectories and many *loops* disappear.

Since a lot of particles are absorbed by the Earth the flux which exits from the surrounding spherical surface is considerably smaller than in the previous case, on the contrary the incoming flux is modified only by the absence of certain *loops*.

The right flux of particles reaching the Earth's atmosphere is then obtained generating particles on the trajectories corresponding to the *legs*. Trajectories like the one shown in fig. 3.4 should be considered only at point B to avoid double or multiple counting of the same track, to respect this prescription we reject all trajectories that are back-traced to the production sphere.

To check the validity of our technique we made a test comparing the results of the inefficient generation technique at 10 Earth's radii distance from the Earth's center with the backtracing technique described above.

Figure 3.5 shows this comparison for several characteristic distributions, the agreement between the two methods is good.

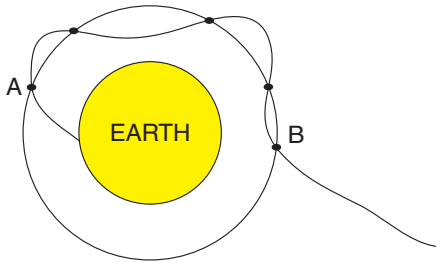

Figure 3.4: An example of multiple counting along a trajectory, this type of trajectory has to be considered only at point B.

3.2 The primary flux

As discussed in chapter 1, the CR flux incident on the Earth's atmosphere extends over a large interval both in energy and intensity and different experimental uncertainties affect its measurement in different energy ranges. An accurate modelling of all the CR flux components over the full energy spectrum is therefore a major problem, which is not completely relevant in our study. In fact, we are interested in the production of atmospheric secondaries - p, $e^{\pm}$ - with energies below few tens of GeV. With this objective

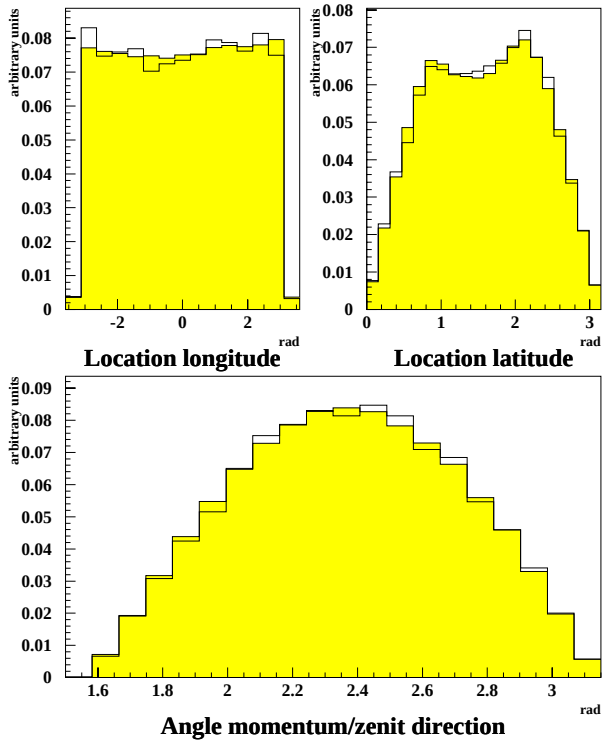

Figure 3.5: Latitude and longitude of impact points and angle between momentum and zenith directions for particles generated at a distance of 10 Earth's radii (solid line) and particle generated at 1.07 Earth's radii (shaded histogram). Distribution are normalized to one.

in mind, we have to evaluate first the CR components and the portion of their energy spectrum which are relevant for the production of secondaries in atmosphere.

Fully ionized nuclei represent $\sim 98\%$ of the cosmic ray flux and almost all of the secondary particles are produced in the nucleus-nucleus scattering, where cosmic rays act as projectiles and atmospheric nuclei as targets.

In a superposition scheme, only one nucleon of the projectile interacts with the target, while the remaining nucleons of the projectile are acting as spectators. After this first interaction the projectile with a missing nucleon breaks in nuclear fragments which interact then against other atmospheric nuclei (see fig. 3.6). The full process can be seen as the superposition of the interactions of all the single nucleons composing the projectile, each one with the same average kinetic energy, against different atmospheric nuclei [125, 126]. As result, for different CR nuclear species, the number of interactions producing secondaries in atmosphere scales linearly with the number

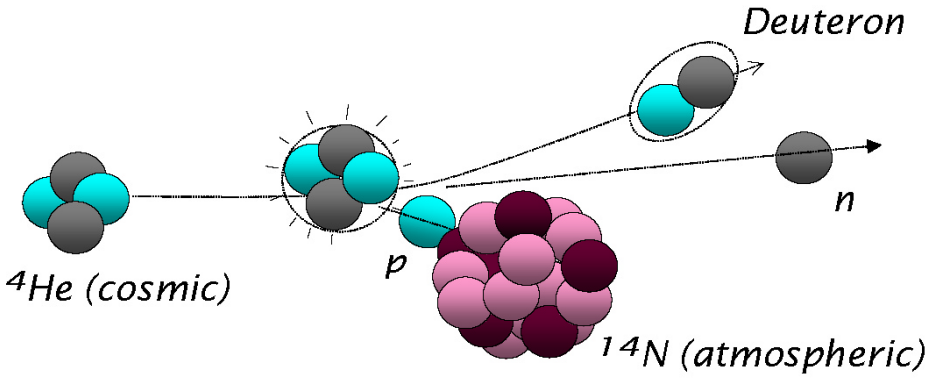

Figure 3.6: Simplified picture of nucleus-nucleus interaction in a superposition scheme.

of nucleons, while the typical features of the interactions, as the multiplicity of secondaries, are characterized by the kinetic energy per nucleon E_{kn}. The flux intensities of different nuclear species shall then be weighted by the nucleon content and E_{kn} to evaluate their contribution to secondary production.

Following this approach, the relative importance of cosmic nuclear species in secondary production is given in figure 3.7 as a function of the kinetic energy per nucleon, E_{kn}. Nuclear species are grouped following the astrophysical scheme, however for each group a mean number of nucleons reflecting the fine composition within the group is used.

It can be noticed that the sum of H and He contributions accounts for more than 90% of the secondary production at all energies, reaching a 95% in the low energy interval - $1 \div 100\, GeV/nucleon$ - where the primary fluxes have larger intensity.

With this figure in mind, we choose to not include the heavier nuclei component in our simulation of the primary CR flux, mostly for three reasons:

1. the global incertitude on the H and He spectra normalization is of the same order of the neglected heavy nuclei flux.

2. the incertitude on heavy nuclei spectra is quite large both on normalization and composition. The former is a consequence of the small flux of heavy nuclei, the latter of experimental problems in the discrimination between nuclear species as the nuclear charge goes up.

3. the simulation of heavy nuclei interactions with the atmosphere at present is quite approximative due to the lack of experimental data.

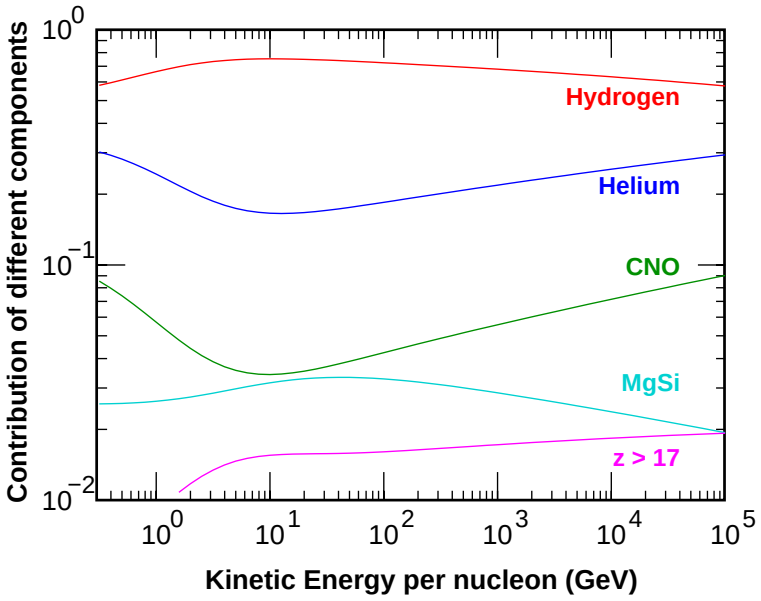

Figure 3.7: Relative contribution of the of various nuclei to the kinetic energy carried by the cosmic rays to the atmosphere [89].

CR electrons and positrons entering the atmosphere can only experience e.m. energy losses or interact with atmospheric nuclei via elastic scattering, with no production of secondary particles. They can contribute to the under cutoff flux observed near earth only if they become *trapped* by the geomagnetic field as consequence of a change in their momentum (dramatic energy losses, multiple scattering, etc.). Given the small probability of such a process and the low electron flux intensity, this contribution can be safely neglected and we did not take into account the $e^{\pm}$ component in our representation of the CR primary spectrum.

3.2.1 Representation of *H* and *He* fluxes

Both the normalization and the shape of the assumed primary spectrum for *H* and *He* have important consequences for the calculation of secondary fluxes. Whereas the normalization of the primary flux directly reflects on that one of secondaries, a twofold dependence from the primary spectrum shape is introduced by geomagnetic effects on the characteristics of secondaries. Given the present experimental errors (cfr. §1.1), a normalization uncertainty of 7% and 8% can be assumed for the *H* and *He* fluxes. Less clear is the representation of the shape:

- at energies below some GeVs the influence of solar modulation reflects in different flux levels depending on the solar cycle.

- at high energies, the experimental measurements, made with calorimetric detectors, have large statistical and systematic errors and are not easily connected with the more accurate determinations at low energy. For instance, in the H measurements, the only experiment that presents an overlap with the AMS and BESS measurements is that of Ryan et al. [25], which measures the spectrum of protons above $50\,GeV$ with a balloon-borne calorimeter. In the region of overlap data are about 25% higher than the magnetic spectrometer measurements. Since the calorimetric energy determination is likely subject to larger systematic errors, it is commonly assumed that high energy data should be normalized downward to the spectrometer data.

Different analytical functions fitted to different experimental data sets have been used to represent the primary fluxes by several groups concerned with the calculation of atmospheric neutrino fluxes [119, 110, 89]. In these calculations, the large spread of the assumed primary fluxes has allowed to get similar final results in spite of the substantial differences in the treatment of hadronic interactions and geomagnetic effects.

As discussed in ref. [89], an agreement on a *standard* representation of the primary flux is mandatory to cross check predictions from different simulation setups. In this view, we used as parametrization of the H and He fluxes the function proposed in ref. [89]:

$$\phi(E_k) \;=\; K \times \left(E_k \;+ b\, \exp\left[-c\sqrt{E_k}\right]\right)^{-\alpha} \tag{3.1}$$

with E_k expressed in GeV/nucleon. The values of the fitted parameters K, b, c, α are reported in table 3.1. The fits for protons and helium are determined largely by the AMS [98] and BESS [97] data, with their small statistical uncertainties. In figs. 3.8 and 3.9 the fitted functions are superimposed on the experimental measurements of proton and helium fluxes.

The spectra proposed in [89] are referring to the solar cycle period of the AMS and BESS measurements. For a general use, the fit parameters describing the solar modulation effect should be adjusted to the solar cycle period on which one is interested. In this work we want to compare our simulation with AMS data and so no adjustment is needed.

parameter/component	α	K	b	c
Hydrogen (A=1)	2.74±0.01	14900±600	2.15	0.21
Helium (A=4)	2.64±0.01	600±30	1.25	0.14

Table 3.1: Parameters for the fit of Eq. 3.1.

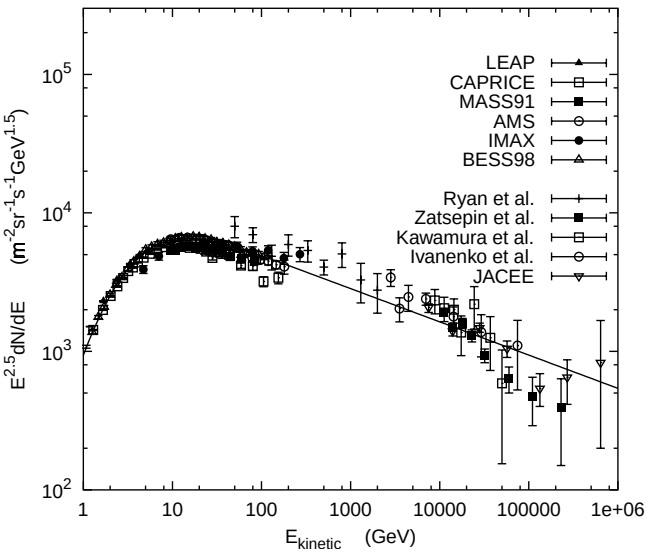

Figure 3.8: Differential flux of protons compared to the fit. Figure from [89].

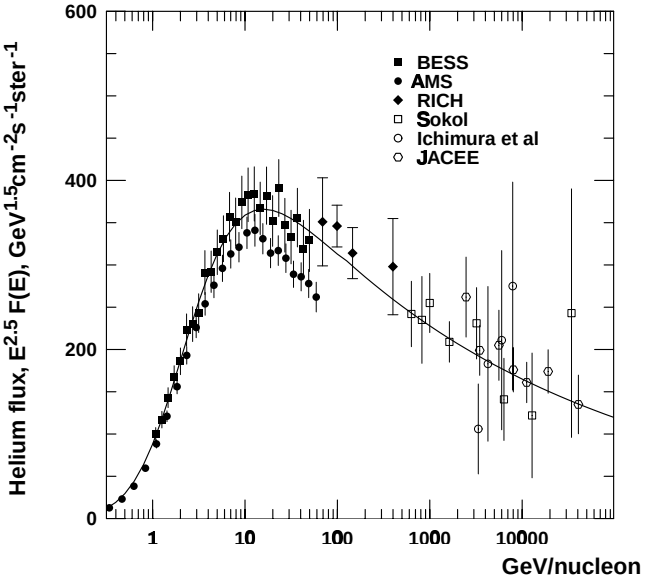

Figure 3.9: Differential flux of Helium compared to the fit. Figure is taken from [89].

3.2.2 The energy interval

The kinetic energy range used in this simulation is $0.1 \div 800\,GeV$ for H primary flux and $0.1 \div 800\,GeV/nucleon$ for He primary flux. This choice allows to include in our simulation $\sim 98.5\%$ ($\sim 98\%$) of the energy carried in atmospheric interactions by cosmic H (He), as can be seen in fig. 3.10. The H and He fluxes, weighted for the E_{kn} and the nucleon content, are shown as a function of E_{kn} in the left panel by the solid and dashed curves respectively. According to the simple interaction scheme discussed above, these distributions represent the primary energy fluxes effective for secondary production in atmosphere. The integrals of these energy fluxes, normalized to unity, are reported as a function of E_{kn} in the right panel. They are defined as:

$$I(E_{kn}) = \frac{\int_{0.1}^{E_{kn}} \Phi(E_{kn})\, A\, E_{kn} dE_{kn}}{\int_{0.1}^{\infty} \Phi(E_{kn})\, A\, E_{kn} dE_{kn}}$$

where $\Phi(E_{kn})$ is the particle flux (particle/(s m^2 sr) and A=1(4) is the nucleon content for H (He). The integration limit of 800 GeV/nucleon used in our simulation is indicated by the vertical line.

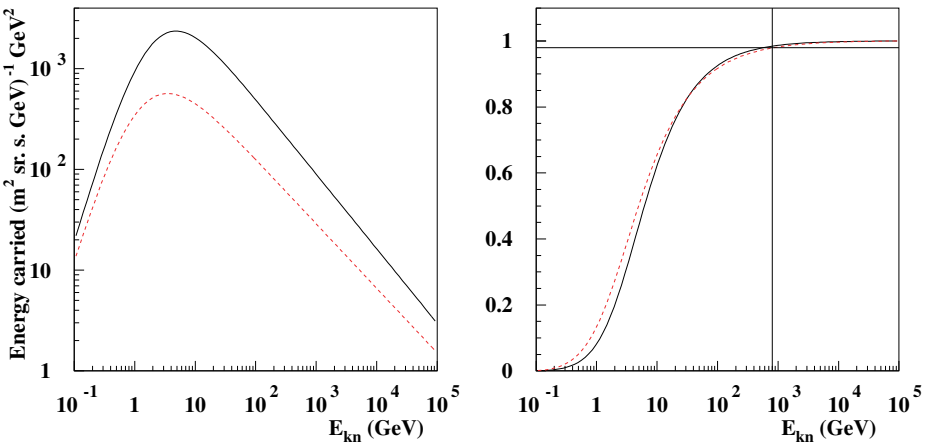

Figure 3.10: a) The amount of kinetic energy carried by H (solid line) and He (shaded line) as function of the kinetic energy. b) Integral function of the left graph, the vertical line placed at $800\,GeV$ represent the upper limit of our spectrum, the horizontal line correspond to 98%.

Within the chosen energy range, H and He flux intensities cover almost seven orders of magnitude. The generation of the events over the full spectrum constitutes a delicate issue both in the optimization of the processing time and the achievable accuracy in the generation process itself.

A standard approach for efficient generation of random numbers belonging to a distribution with a known analytical form is based on the inverse transform method. The generation of a random variable x distributed with a probability density function *f(x)* in a $[x_{min}, x_{max}]$ interval is reduced to the extraction of a random variable u uniformly distributed in the [0,1] interval. The relation between x and u is set by the corresponding cumulative function:

$$F(x) = \int_{x_{min}}^{x} f(y)dy$$

through the expressions :

$$u = F(x) \quad x = F^{-1}(u) \tag{3.2}$$

where F^{-1} is the inverse of the cumulative function. The random variable u is therefore extracted with standard algorithms [111] and the corresponding x found through eq. 3.2. In our case, nor the cumulative function neither its inverse have a simple analytical form and a numerical method inspired to the one used in [112] is used to evaluate them.

As consequence of the particular shape of the energy spectrum, the generation of primary cosmic rays over the whole energy range used in this simulation requires a very high numerical precision. The accuracy required in order to simulate the highest part of the energy spectrum is greater than the computer precision even using a double-precision representation. This problem has been solved dividing the selected energy range in bins.

Even in the absence of a limitation on the generation accuracy, our strategy should take into account of the different yield in secondaries along the energy spectrum to optimize the processing time.

At low values of the kinetic energy, where the particle flux is maximum, the effective yield in secondaries is marginal for our study. Due to the rigidity cutoff, these low energy particles can reach the atmosphere only in proximity of the magnetic poles. As a consequence, their contribution to near Earth secondaries is twofold limited: by the energy (low multiplicity in their interactions and low energy of the secondaries) and by the geomagnetic reduction of their flux in atmosphere. The generation of a *full statistics* for this part of the energy spectrum would then result in a waste of computing time.

On the high energy side of the spectrum ($E_k > 30\,GeV$), the problem is instead to populate a tail representing $\sim 20\%$ of the energy effectively carried for secondary production but only $\sim 0.6\%$ of the overall flux. With a straightforward generation according to the particle flux distribution function this would require too much of computing time.

To overcome these problems we adopted a *biasing* technique. The H and He spectra are separately generated in different intervals of kinetic energy, the events accumulated in the various bins are then biased to a common

normalization. The energy bins, and the correspondent rigidities, are listed in table 3.2 for H and He separately.

The three energy intervals above 3 GeV have been selected allowing for a maximum fall of the intensity in the bin of approximately two orders of magnitude, while a more stringent division has been chosen for the lowest bins. This solution has allowed us to produce a relevant statistic in the energy interval $3 \div 30\,GeV$ - the most significative for secondary production - while reducing the number of events generated in the low energy part and enhancing population in the high energy tail.

	Protons		Helium		
bins	Rigidity	E_k	Rigidity	E_{kn}	E_k
vlow	$0.44 \div 0.81$	$0.1 \div 0.3$	$0.89 \div 2.81$	$0.1 \div 0.75$	$0.4 \div 3$
low	$0.81 \div 3.8$	$0.3 \div 3$	$2.81 \div 16.8$	$0.75 \div 7.5$	$3 \div 30$
med	$3.8 \div 30.9$	$3 \div 30$	$16.8 \div 3122.8$	$7.5 \div 42.5$	$30 \div 170$
high	$30.9 \div 170.9$	$30 \div 170$	$122.8 \div 401.9$	$42.5 \div 200$	$170 \div 800$
vhigh	$170.9 \div 800.9$	$170 \div 800$	$401.9 \div 1602$	$200 \div 800$	$800 \div 3200$

Table 3.2: Energy bins for the H spectrum generation

3.2.3 The flux normalization

As discussed in the previous sections, a biasing algorithm has been applied to optimize the generation with respect the geomagnetic effects and the large variation of the flux intensity. The main drawback of this kind of algorithms is that they effectively destroy the overall normalization of the produced events, which then has to be recalculated both to estimate the statistical significance of our simulation and to convert the generated events into fluxes.

In the generation phase, only the events surviving to the geomagnetic cutoff at the production sphere (500 km a.s.l.) are kept in data files for further processing. The generated H and He fluxes as function of the kinetic energy are shown as solid lines in fig 3.11, respectively in the left and the right panel.

The superimposed points represent the same fluxes after the backtracing step and the rejection due to geomagnetic cutoff. As expected, the main effect of geomagnetic cutoff is at low energies, while no significative reduction is present above few tens of GeV. An energy dependent reduction factor can be defined as:

$$\aleph_i = \frac{N_i^{kept}}{N_i^{gen}} \tag{3.3}$$

where i runs over the five energy bins. The reduction factors are calculated

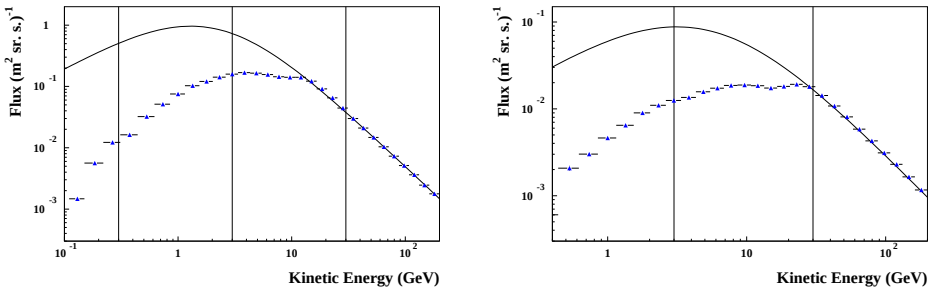

Figure 3.11: The curves represent the generated H (left panel) and He (right panel) fluxes. Points indicate the same fluxes after geomagnetic cutoff. The vertical lines are correspondent to the boundaries of the energy bins used in generation.

once in dedicated runs and are then used to reconstruct the number of generated events.

The inter-bin normalization factors relative to the generated events can be easily obtained integrating the function that defines the primary spectrum bin by bin:

$$J_i = \int_{E_i^{min}}^{E_i^{max}} F(E)\, dE \tag{3.4}$$

Combining these J_i with the reduction factors $\aleph_i$ we obtain the inter-bin normalization factors relative to the events that are passing the geomagnetic cutoff, the ones directly available in our data files.

We refer the interbin normalization to the most significative bin for the particle production, that is the *med* bin for H flux and the *low* bin for the He flux (see table 3.2). This way the global normalization factors are given by (H case):

$$G_i = \frac{J_i\, \aleph_i}{J_{med}\, \aleph_{med}} \frac{N_{med}^{kept}}{N_i^{kept}} \tag{3.5}$$

Table 3.3 is showing all the numbers involved in the normalization procedure with their errors. The errors on the global normalization factors are always smaller than 1% and negligible with respect the much larger incertitude on the primary flux intensity.

We are particularly concerned with this issue since the fluxes predicted by our simulation will have an *absolute* normalization: no adjustable parameters will enter in the comparison with the experimental data.

In fact, starting from the given flux of primary cosmic rays, we can define the time interval corresponding to the number (N^{gen}) of generated primaries

	Proton					
bin	$\aleph$	$\sigma_\aleph$	J	σ_J	G	σ_G
vlow	0.1246	$3 * 10^{-4}\%$	0.149	0.9%	0.1667	0.9%
low	0.6465	$3 * 10^{-4}\%$	0.228	0.8%	1.3254	0.8%
med	0.2212	$3 * 10^{-4}\%$	0.505	0.1%	1.0000	
high	0.0073	$3 * 10^{-4}\%$	0.997	0.2%	0.0654	0.3%
vhigh	0.0004	$3 * 10^{-4}\%$	1.000	0.4%	0.0032	0.4%
	Helium					
bin	$\aleph$	$\sigma_\aleph$	J	σ_J	G	σ_G
vlow	0.4718	$3 * 10^{-4}\%$	0.257	0.3%	0.5880	0.3%
low	0.4851	$3 * 10^{-4}\%$	0.426	0.2%	1.0000	
med	0.0402	$3 * 10^{-4}\%$	0.959	0.4%	0.1866	0.4%
high	0.0027	$3 * 10^{-4}\%$	1.000	0.8%	0.0129	0.8%
vhigh	0.0002	$3 * 10^{-4}\%$	1.000	0.5%	0.0010	0.5%

Table 3.3: Factors entering in the inter-bin and absolute normalization. Refer to text for more details.

in a given interval of energies $[E^{min}, E^{max}]$:

$$\Delta t = \frac{N^{gen}}{S\,\Delta\Omega\,\int_{E_{min}}^{E_{max}} F(E)dE} \tag{3.6}$$

where S and $\Delta\Omega$ are respectively the surface and the solid angle over which we generate the events, $F(E)$ is the function that defines the primary spectrum.

The time interval Δt is called *Equivalent Time Exposure* (ETE) and it is used to evaluate from the produced numbers of secondaries the absolute fluxes (cfr §5.1) allowing for a direct comparison with data. The ETE is more easily calculated using only the generated events in the *high* bin, where no geomagnetic reduction is effective. The obtained value of the ETE is then scaled to the normalization given by the *med* bin for protons and *low* bin for He nuclei.

3.3 The geomagnetic field

As already discussed in chapter 2, the geomagnetic field is the sum of two components: the internal field generated by the Earth and the external field generated in the interaction between the solar wind and the internal field.

Internal field To calculate the internal geomagnetic field we make use of the *International Geomagnetic Reference Field* (IGRF) model [116]. The IGRF model represents the main field without external sources and it is

the empirical representation of the Earth's magnetic field recommended for scientific use by the International Association of Geomagnetism and Aeronomy (IAGA). The geomagnetic scalar potential is represented as a series expansion of orthogonal spherical functions which takes the form:

$$V(r,\vartheta,\varphi) = R_E \sum_{n=1}^{\infty} \sum_{m=0}^{n} \left(\frac{R_E}{r}\right)^{n+1} [G_n^m \; cos(m\,\varphi) + H_n^m \; sin(m\,\varphi)] \; P_n^m(cos\,\vartheta) \tag{3.7}$$

where R_E is the mean radius of the Earth, r is the radial distance from the center of the Earth, φ is the east longitude measured from Greenwich, ϑ is the geocentric colatitude and P_n^m are the *Schimdt quasi-normalized associated Legendre functions* of degree n and order m.

G_n^m and H_n^m are the model coefficient, based on all available data sources including geomagnetic measurements from observatories, ships, aircrafts and satellites. The IGRF model consists of coefficient sets up to the order $n = 10$ for the epochs 1945 to 2000 in steps of 5 years.

The typical error on the Earth surface is of the order 1 nT out of a typical field intensity of 40000 nT. The relative error is believed to be $\sim 10^{-4}$ even far from the Earth surface [117].

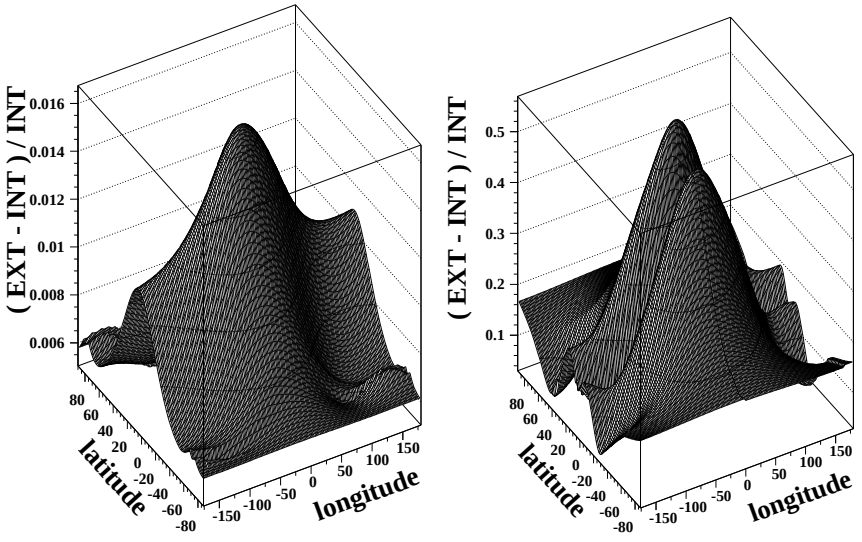

Figure 3.12: Map in geographical coordinates of the relative difference between the external and the internal components of the magnetic field at 2 (left) and 7 (right) Earth radii distance from the Earth's center.

External field To simulate the external field we use the Tsyganenko 2001 model [115] widely used in the community and recommended for scientific use by NASA. We already showed in chapter 2 (fig. 2.5) the ratio between

the internal and external field intensities as function of the distance from the Earth's center (open squares) here we show the relative difference between the external and internal component of the magnetic field, mapped as a function of geographical coordinates in fig. 3.12 for two different distances from the Earth's center. To save computation time, the external component is not calculated for distances below $2\,R_E$ where its contribution to the total field is less than 1%.

The external field depends on the solar wind pressure, on the Earth-Sun distance, and on the orientation of the Earth's magnetic field with respect of the Sun. As consequence it depends on the solar activity, on the day of the year, and of the hour of the day considered. We chose the solar activity and the day corresponding to the AMS flight on the Space Shuttle Discovery (2 June 1998), for what concerns the hour of the day we chose 0:00 GMT. We made also a test changing the hour of the day to 12:00 GMT, so to obtain the opposite dey/night configuration, no appreciable difference were noted on the results.

3.4 The tracing method

Numerical methods are of general use to describe the complex motion of a charged particle in presence of arbitrary magnetic and electrical fields. In our simulation, however, we are dealing with a slowly varying quasi-dipolar magnetic field in absence of an electrical one. This situation is considerably simpler than the general case so a semi-analytical approach to the problem becomes affordable and convenient for saving computation time.

In our approach, the particle motion is calculated in subsequent steps, each one corresponding to a displacement in a region of a nearly uniform magnetic field. Within the single step, the particle motion is described by the solution of the Lorentz equation in the trivial case of a uniform B field. The resulting trajectory is then the sum of spiral segments each one with instantaneous radius:

$$\rho = \frac{p\,sin(\lambda)}{Z\,e\,B} = \frac{R\,sin(\lambda)}{B} = \frac{R_\perp}{B} \tag{3.8}$$

and helix pitch:

$$S = 2\pi\,\frac{p\,cos(\lambda)}{Z\,e\,B} = 2\pi\,\frac{R\,cos(\lambda)}{B} = 2\pi\,\frac{R_\parallel}{B} \tag{3.9}$$

where p is the momentum of the particle, R its rigidity, Ze its charge, B the intensity of the magnetic field and λ the angle between $\vec{p}$ and $\vec{B}$.

Using this method, the main issue of particle tracing is reduced to the evaluation of an adaptive step size that guarantees a nearly uniform field in the single displacement, while optimizing the overall number of steps used

to reconstruct the trajectory. As we will discuss in the following, a relatively simple logic based on a reduced number of parameters is enough to achieve an accuracy better than 0.01% in the single step and a significative gain in processing time with respect to numerical integration methods [1].

Three control parameters are used to evaluate the optimal size of the step length Γ, defined as the displacement along the trajectory in the single step:

The maximum deflection angle θ_{MAX} By default, the step length is bounded to the value Γ_θ corresponding to a deflection in the trajectory equal to θ_{MAX}. This allows to get a default step length automatically adapted to both the particle rigidity and the field intensity.

The maximum step length Γ_{MAX} For large gyro-radius (high rigidity and/or low B intensity) Γ_θ could be too large to consider valid the approximation of uniform field. In this cases, the step length is fixed to the Γ_{MAX} value.

The minimum step length Γ_{MIN} For very small gyro-radius (low rigidity and/or high B intensity) the particle loops on a tight spiral and the default condition $\Gamma < \Gamma_\theta$ results in a too large number of steps. In these circumstances the B field does not way appreciably within a single loop and we can safely impose as step length the value of Γ_{MIN}.

Another constraint on the step length comes from the requirement that a step should not cross the boundary between two regions composed of different materials. The steps are always stopped on the boundaries, whatever is the evaluated step length. This constraint is especially relevant in the motion through the atmosphere, when crossing the layers with different material composition.

An accurate tuning of the numerical values for the three control parameters has been done in order to reconcile the opposite requirements of accuracy of the tracing, obtained with many small steps, and computational speed, obtained with few large steps.

The typical variation of $\vec{B}$ over a single step has been evaluated as a function of θ_{MAX} for a relatively large (small) value of Γ_{MAX} (Γ_{MIN}). From the obtained distributions, the behavior of the relative error on the step length has been studied for different classes of events and the single step accuracy evaluated. The influence on the whole trajectory from different sets of control parameters has been finally checked against physical distributions. In the following we will give the details for each phase of the tuning procedure.

[1] A gain of a factor ~ 30 in processing time has been evaluated from a direct comparison with the integration done in [109] using a Runge-Kutta algorithm of the 4^{th} order.

The B field variation The relevant distributions obtained from the generation of three sets of events with $\Gamma_{MAX} = 700\,km$, $\Gamma_{MIN} = 300\,m$ and $\theta_{MAX} = 10°$, $1°$, $0.5°$ are presented in fig. 3.13. In the scatter plots on the left, the step length Γ is shown versus dB/B, the relative variation of the B field intensity between the start and the end of the step, for the three values of θ_{MAX}. The rightmost distributions are instead showing Γ versus ϕ_B, the angle between the direction of $\overrightarrow{B}$ at the start and the end of the step.
Two main features emerge from these distributions:

- The change in the B field direction is contained within few degrees even for large values of Γ and θ_{MAX}. In the majority of the steps or for $\Gamma < 10^5\,m$ the effective ϕ_B is always smaller than $0.5°$.

- As expected the dB/B is strongly dependent on the step size. dB/B is nearly constant at the 0.1% level for step lengths below few tens of kilometers, while a rapid increase - up to 5% - is observed going towards longer steps. The asymmetry in the dB/B sign appearing for small θ_{MAX} values is representative of the underlaying track composition. For $\theta_{MAX} = 10°$ large steps can be performed in all the tracing condition so that dB/B can assume with the same probability positive and negative values. With smaller values of θ_{MAX} very long steps are performed almost only in the back tracing of high rigidity primary cosmic rays, and as a consequence, negative values of dB/B are favored.

From the above discussion it is clear that values of $\theta_{max} \ll 10°$ and $\Gamma_{MAX} \sim\leq 10^5 m$ allow to neglect changes of the $\vec{B}$ direction along the step while keeping under control also the variation of the B field intensity.

The single step accuracy For a given dB/B along the tracing step, the error induced on the elementary displacement (ϵ_s) depends on the step length as well as on all the variables defining the particle motion (eq. 3.8, 3.9). A conservative estimate of the error on the trajectory over the single step has been obtained by means of double tracing. In the first tracing, the field value at the starting point of the step (B_s) is used to calculate the trajectory. The value of the B field found at the end point of the step (B_e) is then used to recalculate the trajectory, starting back from the initial position and for the same time interval (t_s) as in the first tracing. The distance (ε_t) between the points of arrival of the two trajectories is a conservative estimation of ϵ_s (see fig. 3.14), since the field intensity changes continuously (in most cases almost linearly) along the step, from B_s to B_e.

We have seen how changes of the $\vec{B}$ direction along the step can be safely neglected for a reasonable choice of the control parameters. Under

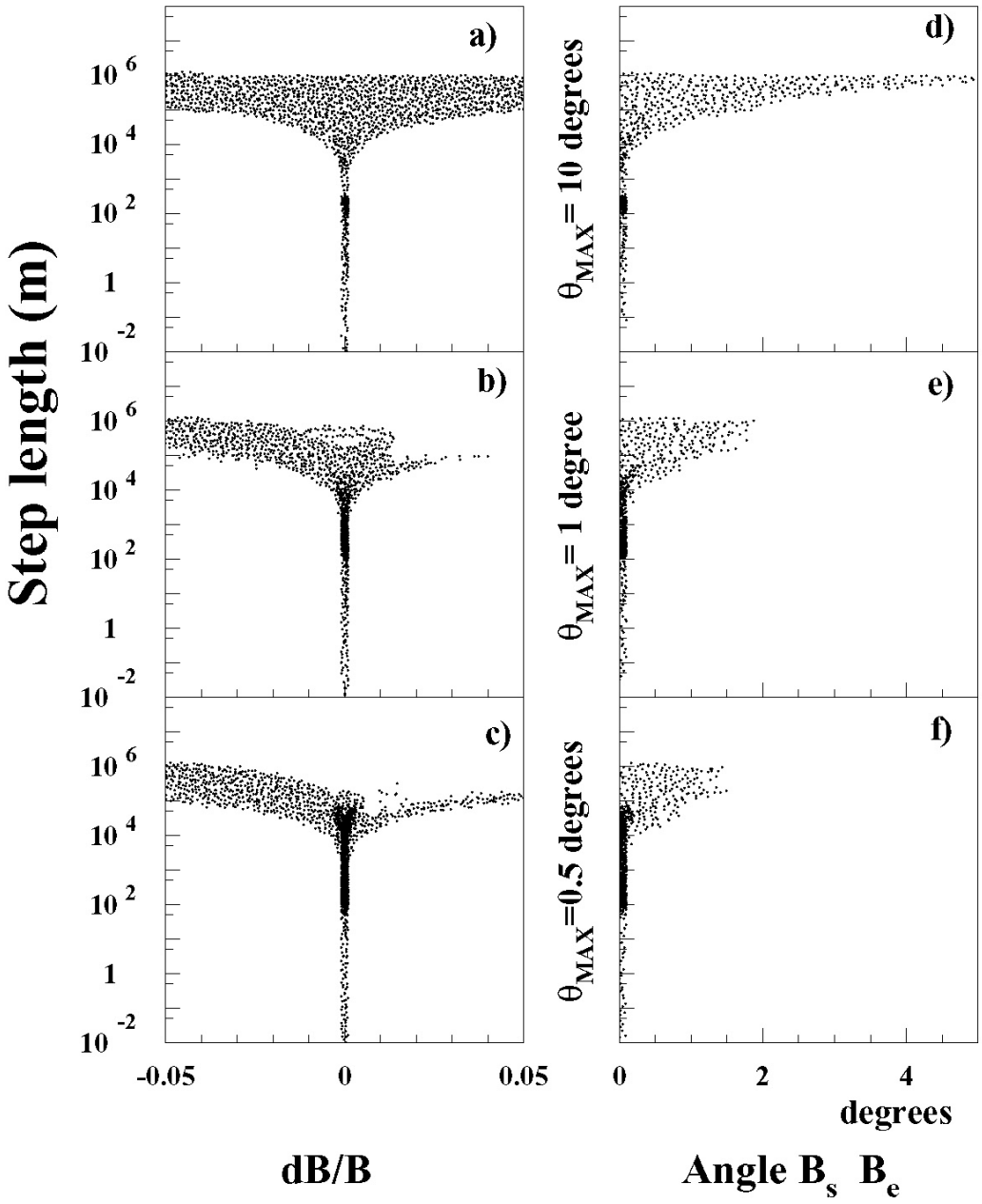

Figure 3.13: a b c) the relative variation of the B intensity from the start to the end of the step. d e f) the the angle between the B directions at the start and at the end of the step. Figures are obtained tracing a set of standard events.

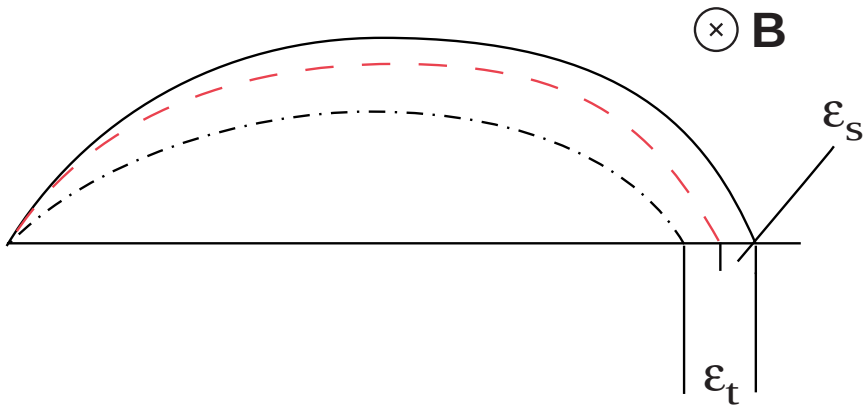

Figure 3.14: Example of the error estimation($B_s < B_e$): solid line is the trajectory obtained with $B = B_s$, dashed line is the real trajectory with B varying from B_s to B_e, dashed pointed line is the trajectory obtained with $B = B_e$. See text for more details.

this condition, the analytical calculation of ε_t becomes quite simple [2] and its expression is given by:

$$|\vec{x}(B)-\vec{x}(B+\delta B)| = \rho\,\frac{\delta B}{B}\left\{2\,[1-cos(\nu\,B\,t)] + (\nu\,B\,t)^2 - 2\,\nu\,B\,t\,sin(\nu\,B\,t)\right\}^{\frac{1}{2}} \tag{3.10}$$

where:

$\varepsilon_t = |\vec{x}(B) - \vec{x}(B+\delta B)|$, $B = B_s$, $\delta B = B_e - B_s$, $t = t_s$
$v_\perp$ the velocity component in the direction orthogonal to the field
$\rho = \frac{v_\perp}{\nu B}$ is the curvature radius
$\nu = \frac{Z\,e}{\gamma\,m}$ ρ is the gyromagnetic momentum.
m and γ are respectively the rest mass and the Lorentz boost factor of the particle.

Eq. 3.10 points out the dependence of ε_t on the field intensity B, the momentum of the particle p (trough γ and ρ), the pitch angle λ (trough ρ), and the length of the step Γ (trough t).

Figures 3.15 and 3.16 illustrate the relative error on tracing ($\epsilon_r = \epsilon_t/\Gamma$) as function of the four variables p, λ, B, and Γ. In each plot the four curves are corresponding to four values of dB/B. The two figures are relative to different values of p, λ, B and Γ representative of the typical conditions.

While the distributions reported in figures 3.15 and 3.16 can be relevant for a comprehension of the major error sources, they are of almost no practical use for the final assessment of the accuracy. In fact, a complex multidimensional analysis would be needed to reproduce the different combinations of values which could be assumed by the four parameters p, λ, B, Γ.

[2] The detailed calculation of ε_t can be found in the appendix at the end of this chapter.

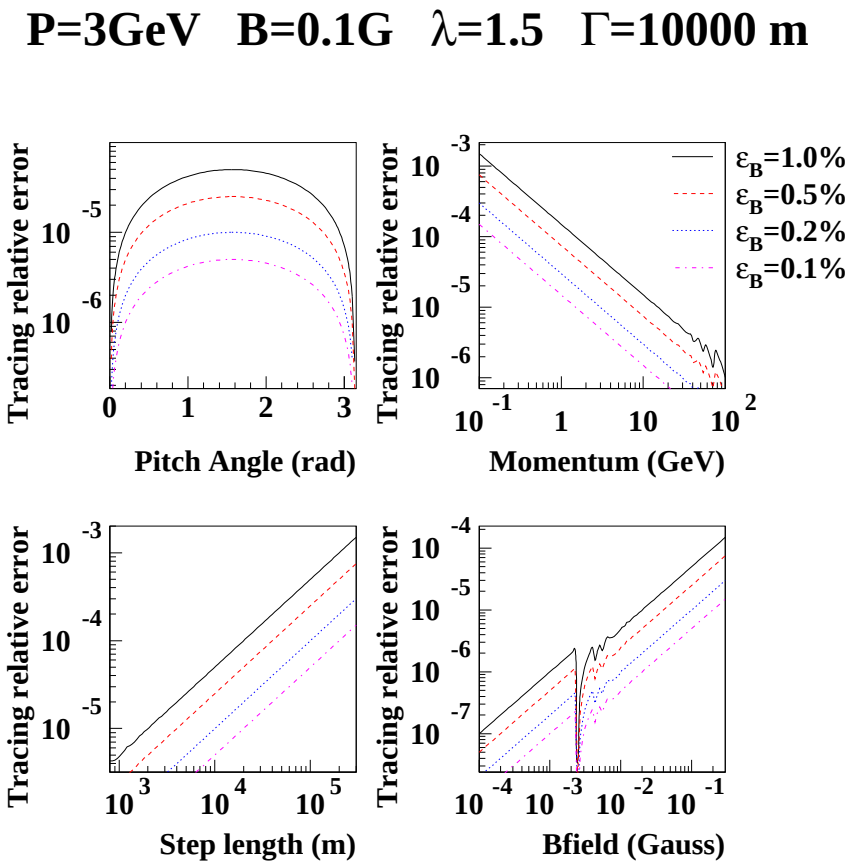

Figure 3.15: Each plot shows in turn the relative error on tracing as a function of p, λ, B, Γ. For each distribution, the other quantities are set to the values indicated on the top of the figure. The four different curves correspond to four different values of ε_B, the relative error on B intensity.

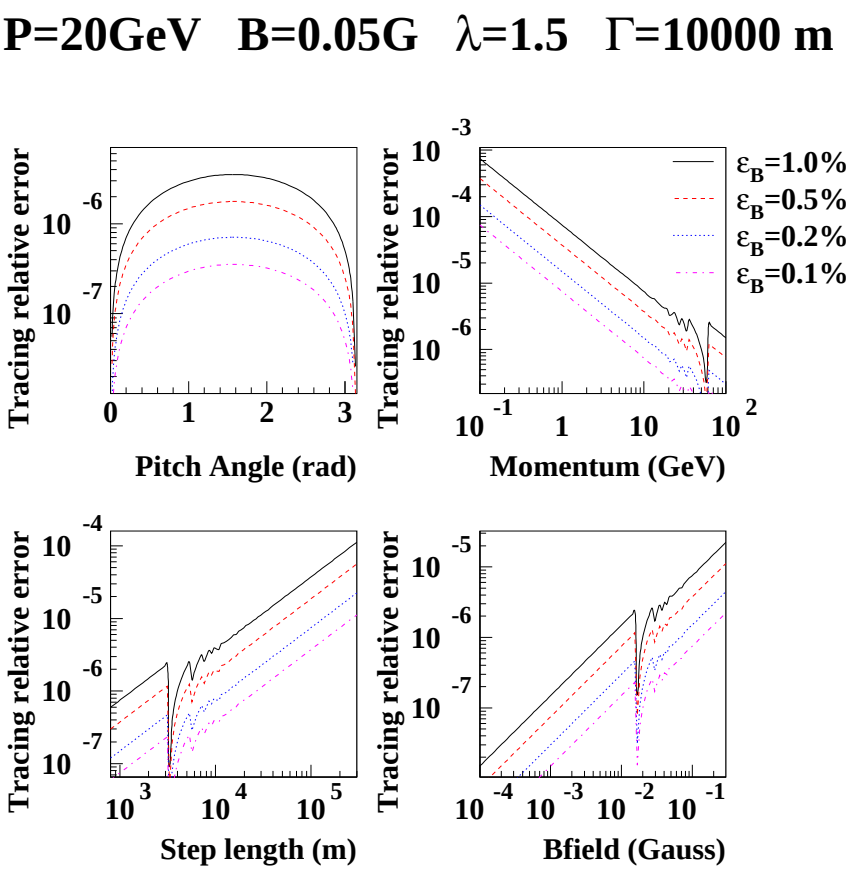

Figure 3.16: Each plot shows the tracing relative error as function of one of the four variables p, λ, B, Γ, the remaining variable are set to the values indicated on the top of the figure. The four different curves correspond to four different values of ε_B, the relative error on B intensity.

Dedicated samples of H events have been then generated with different sets of the control parameters evaluating in each step and, for all the tracks in the event, the relative error on tracing.

The influence of the control parameters on tracing could be directly evaluated from the resulting ϵ_r distributions, as those presented in figs. 3.17, 3.18. The distribution of ε_r at $\theta_{MAX} = 1^\circ$ is shown in fig. 3.17 for different values (100 , 20 , 1 Km) of Γ_{MAX}. In fig. 3.18, the ε_r behavior is studied for a fixed $\Gamma_{MAX} = 20\,km$ and different θ_{MAX} values (0.5°, 1°). The large differences in the number of entries corresponding to the various distributions is representative of the variation in the number of steps needed to simulate the same events with the different control parameters. The choice of $\Gamma_{MAX} \leq 20\,Km$ and $\theta_{MAX} \leq 1^\circ$ corresponds to a maximum ε_r of 0.01%[3] with an average ϵ_r at least two orders of magnitude smaller.

The global verification Given the large number of steps ($10^2 \div 10^5$) used to reconstruct a single trajectory, it is far to be obvious how to quote a sensible estimate of the final error. To further investigate the influence of the control parameters on the overall tracing accuracy, we directly verified the ability of the simulation to reproduce some known physical distribution.

One of the most sensitive quantity for this purpose is the *live time* of atmospheric secondaries, defined as the time interval between their production and their absorbtion in atmosphere. This effectively represents the residence time of the the magnetic shell where the secondary has been generated.

The relevance of this distribution for our study will be discussed in detail later on (cfr. §5.3). Meanwhile, we show as a reference the live time as a function of the kinetic energy for protons measured at an altitude of 400 km in the equatorial region (fig. 3.19). This has been obtained via a numerical integration tracing on the AMS data [109].

Two separated populations are clearly distinguished in the two bands of fig. 3.19: the *short lived*, with residence times typically below 1 s and weakly dependent on the particle's energy, and a *long lived*, characterized by live times up to some tens of seconds and a much stronger dependence upon the kinetic energy. For this discussion we focus on the *long lived* population, more sensible to the tracing accuracy due the larger length of time along which the trajectory must be followed.

Figures 3.20 a)-d) are showing the distribution of the life time of the secondary protons as obtained in our simulation. The plots a), b), c) are corresponding to the Γ_{MAX} values of 100, 20, $1\,Km$ with $\theta_{MAX} = 1^\circ$. In d), the values of Γ_{MAX} and θ_{MAX} are set to $20\,Km$ and 0.5° respectively.

In figure 3.20a) we can note the presence of protons with very high life time (up to some hundreds of seconds). This population disappears in b)

[3] This is the accuracy used in similar studies [109] carried on AMS data by means of numerical integration of the trajectory

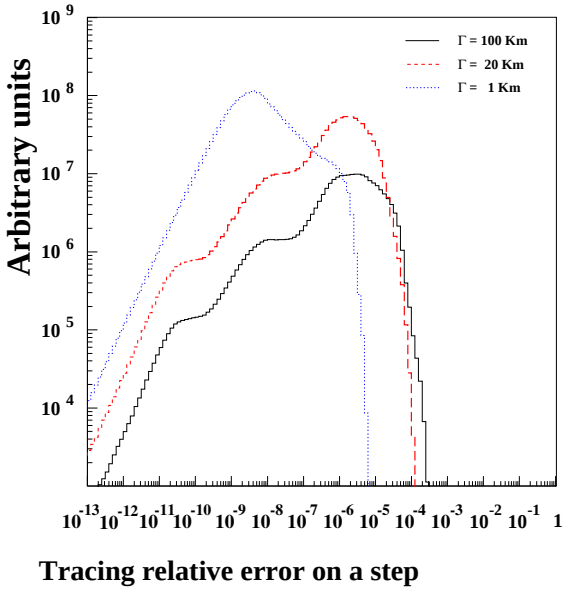

Figure 3.17: Distribution of the tracing relative error in our simulation. The three curves are corresponding to the values of the control parameter Γ_{MAX} reported in figure. In all cases $\theta_{MAX} = 1^\circ$ and

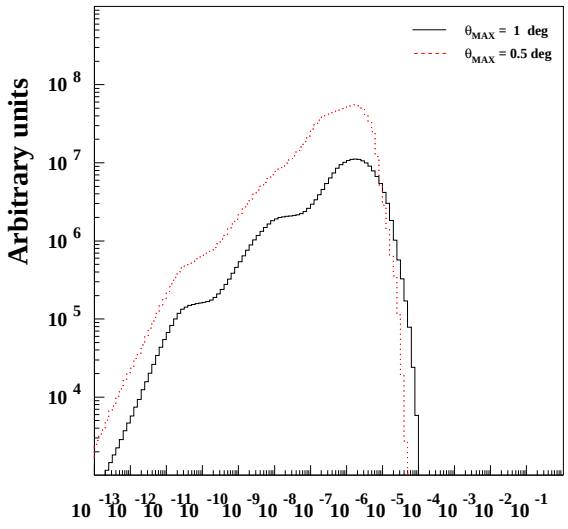

Figure 3.18: Distribution of the tracing relative error in our simulation. The two curves are corresponding to the values of the control parameter θ_{MAX} reported in the figure. In both cases $\Gamma_{MAX} = 2 \cdot 10^5 m$.

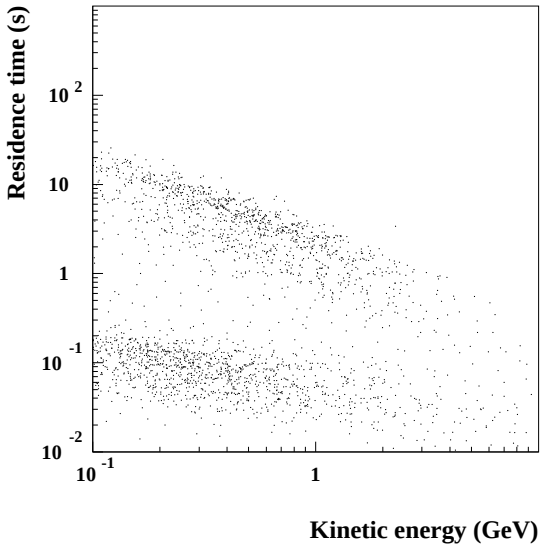

Figure 3.19: Live time of secondary protons detected by AMS in equatorial region ($|\theta_M| < 0.3$

).

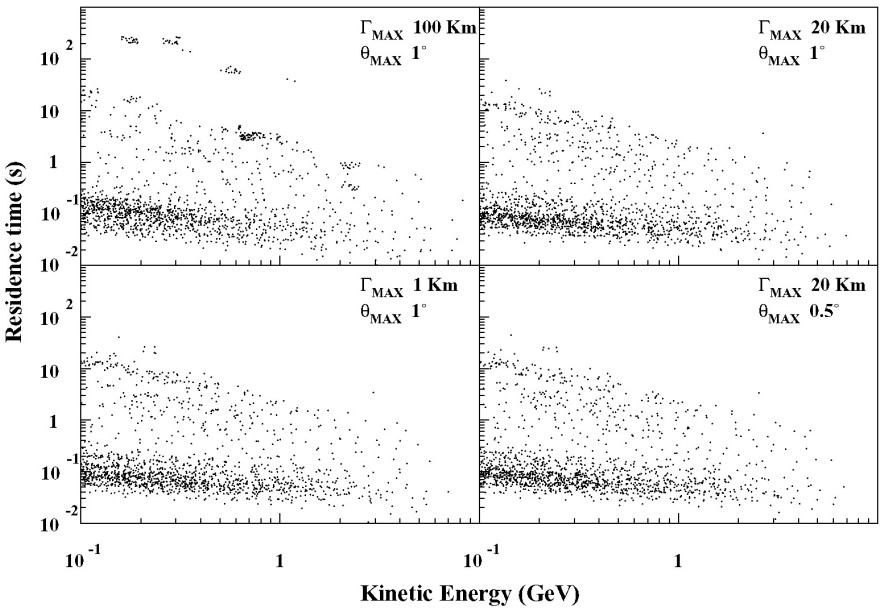

Figure 3.20: Residence times of secondary protons as a function of their kinetic energy in our simulation for four different combinations of the tracing parameters.

where the maximum step length is $20\,Km$ and the distribution assumes the same shape as for data (fig. 3.19). Choosing smaller values of the control parameters as in Fig. c,d, the distribution has no appreciable variation.

We are therefore confident in our final choice of the control parameters, $\Gamma_{MAX} = 20\,Km, \theta_{MAX} = 1°$, that satisfies a $\varepsilon_r^{MAX} = 10^{-4}$ with a minimum number tracing steps.

3.5 The Earth's atmosphere

The atmosphere can roughly be characterized as the region from sea level to about 1000 km altitude around the globe, where neutral gases can be detected. Below 50 km the atmosphere can be assumed to be homogeneously mixed and can be treated as a perfect gas. Above 80 km the hydrostatic equilibrium gradually breaks down as diffusion and vertical transport become important.

The major species in the upper atmosphere are N_2, O, O_2, H, He. Temperature-oriented nomenclature differentiates the strata of the atmosphere as follows: the troposphere, from sea level up to about 10 km, where the temperature decreases; the stratosphere, from 10 km up to about 45 km, where the temperature increases; the mesosphere, from 45 km up to about 95 km, where the temperature decreases again; the thermosphere, from 95 km to about 400 km, where the temperature increases again; and the exosphere, above about 400 km, where the temperature is constant.

In this work the atmosphere is simulated up to 120 Km using 60 concentric layers of homogeneous density and chemical composition. Data on density and chemical composition were taken from the Mass-Spectrometer-Incoherent-Scatter Extended (MSISE) model (fig. 3.21b). The Earth is modelled as a solid sphere which absorbs every particle reaching its surface.

The MSISE model describes the neutral temperature and densities in Earth's atmosphere from ground to thermospheric heights. Below 72.5 km the model is primarily based on the MAP Handbook [113] tabulation of zonal average temperature and pressure by Barnett and Corney, which was also used for the CIRA-86 [114]. Below 20 km these data were supplemented with averages from the National Meteorological Center (NMC). In addition, pitot tube, falling sphere, and grenade sounder rocket measurements from 1947 to 1972 were taken into consideration. Above 72.5 km MSISE-90 is essentially a revised MSIS-86 model taking into account data derived from space shuttle flights and newer incoherent scatter results.

In this work the atmosphere simulation stops at 120 Km a.s.l. because, above this altitude, the short term effects on the primary and secondary cosmic rays are negligible. Figure 3.21a is showing the nuclear interaction length (λ_I) and the electromagnetic interaction length (X_0) in the atmosphere plotted as function of altitude. The plot should be read in this way

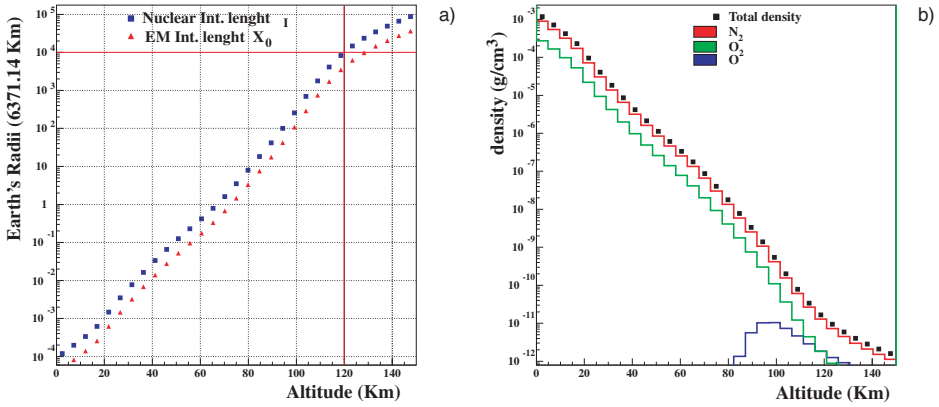

Figure 3.21: a) The nuclear interaction length (λ_I) and the electromagnetic interaction length (X_0) in the atmosphere plotted as function of altitude (see text); b) the density and the chemical composition of the Earth's atmosphere.

e.g. at 120 Km a proton should follow a circular orbit for a distance of $\sim 10^4\, R_E$ before to experience a full λ_I.

A limit of this simulation is to use homogeneous shells, where the true atmosphere density presents some variation from the pole to the equator. However although there are different profiles the global thickness of the atmosphere is more or less the same at pole and at equator. Being interested in the global production of secondaries this should not affect our simulation.

3.6 The simulation of the interactions

The simulation of the cosmic rays interactions with the atmosphere is particulary demanding since it is necessary to consider a wide energy range of primaries and also a set of different projectiles. This situation is quite different from typical particle physics experiments were almost mono-energetic beams are considered.

Historically many packages were developed to simulate atmospheric interactions of cosmic rays but they were oriented to experiments looking at cosmic rays flux from a defined location on the Earth's surface or in the near atmosphere (i.e balloon borne experiments). These simulations were interested mostly to the determination of secondaries produced in atmosphere that could reach the considered detector, as a consequence they usually introduced a set of approximations that cut off part of the cosmic rays initiated showers. This prevents their use to reproduce the behavior of secondaries above the whole Earth.

Different approximations were introduced instead in the simulations developed for the estimate of the atmospheric neutrinos fluxes: secondary particles produced in the atmospheric interactions were supposed to move collinear with the primary particle (1-Dimensional simulation). The loss of information on the directionality of the secondaries is clearly in contrast with our need of a full description of the evolution of their trajectories in the geomagnetic field.

In the last few years some 3-D models have been developed following two distinct approaches in the modelling of the interactions: parameterized codes and theoretically inspired simulations.

In the first case, one relies upon analytical formulas, parameterizing experimental data, which possibly try to exploit some general phenomenological feature of particle production.

The main advantage of this approach is that it can lead to the comprehension of some important and general properties of particle production in term of analytical expressions. The price to pay is the lack of generality and the spoiling of correlations among reactions products. As an example of this kind of simulation we can cite the TARGET code [118] developed by the Bartol group, the HKKM model [119], and the one reported in ref. [108].

The second line of approach is a theory driven simulation of the interactions. The interactions are described microscopically as results of the interactions of the fundamental components of the hadrons.

In the ideal case the features of the interactions may be derived from the QCD lagrangian but the typical energy range we are interested in, is within the low-p_T region where the running coupling is large and the perturbation theory is not applicable. In the real case the physics in this energy region is well described by effective theories based on the peculiar quark properties like confinement and gluon self-interactions, this models had remarkable success in describing the features of hadronic interactions.

We consider the microscopic approach as more fundamental and reliable than parameterizations since each steps has sound physical basis. The final predictions are obtained with a minimal set of free parameters, fixed for all energies and target/projectile combinations. Results in complex cases as well as scaling laws and properties come out naturally from the underlying physical models. The basic conservation laws are fulfilled "a priori". A microscopic model may reach a very high detail, at least in principle, and therefore it is a good choice when aiming at precise calculations. The price to pay is the loss of simplicity and flexibility: there are no more simple analytical guidelines which allow to understand the basic properties. Furthermore, microscopic codes are more demanding than parameterizations in terms of computing power.

We chose to use the FLUKA interaction model [120], together with the FLUKA framework that allows to trace the particle and to define the geometry and the materials in the volume of interest.

3.6.1 The FLUKA model

The modern FLUKA is an interaction and transport Monte Carlo code able to treat with a high degree of detail the following problems;

- Hadron-hadron and hadron-nucleus interactions $0 - 100\,TeV$
- Electromagnetic and μ interactions $1\,keV - 100\,TeV$
- Charged particle transport - ionization loss
- Neutron multigroup transport and interactions $0 - 20\,MeV$

The hadronic models which are used inside FLUKA to describe nonelastic interactions are:

- The "low-intermediate" one, PEANUT, which covers the energy range up to $5\,GeV$
- the high energy one, Dual Parton Model (DPM), which can be used up to several tens of TeV, based on the color string and quark confinement models.

The nuclear physics embedded in the two models is very much the same. The main differences are a coarser nuclear description (and no pre-equilibrium stage) and the Gribov-Glauber cascade for the high energy one.

The predictions of FLUKA interaction model have been checked with large sets of experimental data collected in accelerator experiments[4], being FLUKA a general purpose tool for simulating hadronic and electromagnetic interactions widely used in the particle physics community. This is another advantage of FLUKA with respect the "parametrical" models that are often developed and used only for cosmic rays.

Two set of data are of particular interest for which concerns the simulations of the trapped particles and of the atmospheric neutrinos fluxes:

- The reproduction of the measurements done by Atherton et al. [122] and by the SPY collaboration [123] on the secondaries produced in $p - Be$ interactions. In particular the intensity and the angular distribution of secondary K and π as well as the $K^{\pm}/\pi^{\pm}$ ratios are reproduced by FLUKA at the level of 20% as reported in [123].
- The good reproduction of the data on muons in atmosphere as measured by the CAPRICE experiment [124], both at ground level and at different floating altitudes as reported in ref. [125].

[4] A detailed review of these comparison with data can be found in ref. [121].

The production rate of π and K is interesting because these particles represent the most common products of the proton nucleus interactions and because they are the parents of secondary muons, electrons and neutrinos.

The fluxes of atmospheric muons are strictly related to the neutrinos ones, because almost all ν's are produced either in association with, or in the decay of $\mu^{\pm}$. Furthermore electrons and positrons found at AMS orbit came mostly from $\mu^{\pm}$ decays and from π^0 decay chain (cfr. §5.4).

To simulate the interactions of helium nuclei we use the superposition approximation. Helium nuclei coming to the atmosphere are unpacked into two protons and two neutrons free to interact. Work done by the FLUKA authors indicate that the superposition model well describe the helium-nucleus interaction in the atmosphere at least within the uncertainties on the Helium-nucleus cross section [125, 126].

3.7 Appendix

The trajectory of a charged particle in a uniform B field is conveniently described in a reference frame defined as in fig. 3.22. The x-axis is chosen along the **B** direction and the y-axis is directed along the force:

$$\mathbf{F} = \frac{Ze}{\gamma m}\,\mathbf{p} \times \mathbf{B} \tag{3.11}$$

where p is the momentum of the particle, Ze its charge and γ is the Lorentz factor.

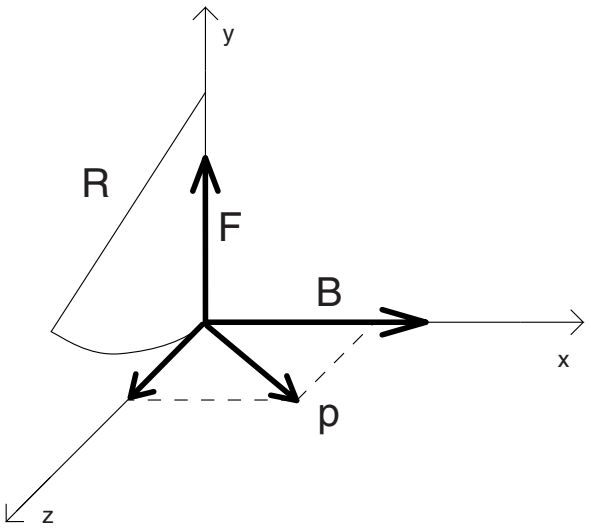

Figure 3.22: Reference frame

The z-axis is fixed such as to get a clockwise triplet and is directed along the direction of the momentum component orthogonal to the field ($\mathbf{p}_\perp$).

In this reference frame, the motion of the particle can be decomposed as a linear uniform motion along the x-axis and a circular uniform motion in the yz-plane with curvature radius:

$$\rho = \frac{p_\perp}{Ze\,B} = \frac{\gamma m\, v_\perp}{Ze\,B} = \frac{v_\perp}{\nu\,B} \tag{3.12}$$

and angular velocity:

$$\omega = \frac{v\perp}{\rho} = \nu B \tag{3.13}$$

A particle that at the time t_0 is in the origin of the frame of reference, at the time t has coordinates:

$$\begin{aligned} x(t) &= v_\parallel\, t \\ y(t) &= \rho\,(1 - cos(\nu B\, t)) \\ z(t) &= \rho\, sin(\nu B\, t) \end{aligned} \tag{3.14}$$

Considering a variation of the B field intensity is straightforward to calculate the corresponding variation in the trajectory:

$$\begin{aligned} \Delta x &= \frac{\partial x}{\partial B}\, dB = 0 \\ \Delta y &= \frac{\partial y}{\partial B}\, dB = \rho\,(\nu B t\, sin(\nu B t) - cos(\nu B t) - 1)\,\frac{dB}{B} \\ \Delta z &= \frac{\partial z}{\partial B}\, dB = \rho\,(\nu B t\, cos(\nu B t) - sin(\nu B t))\,\frac{dB}{B} \end{aligned} \tag{3.15}$$

The modulus of the distance between the end points of the original trajectory and the one obtained with the variation, is given by:

$$|\vec{x}(B) - \vec{x}(B + \delta B)| = \sqrt{(\Delta x)^2 + (\Delta y)^2 + (\Delta z)^2} = \tag{3.16}$$

$$\rho\,\frac{\delta B}{B}\left\{2\,[1 - cos(\nu\, B\, t)] + (\nu\, B\, t)^2 - 2\,\nu\, B\, t\, sin(\nu\, B\, t)\right\}^{\frac{1}{2}} \tag{3.17}$$

that is the equation 3.10.

Chapter 4

The AMS measurements

The Alpha Magnetic Spectrometer (AMS) [127] is an high energy physics experiment, scheduled for installation on the International Space Station. AMS is addressed to investigate two of the greatest puzzles in the understanding of the universe: the existence of cosmological antimatter in our universe [128, 130, 132], and the nature of the dark matter pervading the universe [133, 134].

In the June 1998, as first phase of the AMS project, a precursor (AMS01) of the planned final detector flew onboard of the Space Shuttle Discovery collecting for the first time, in the full area enclosed between the latitudes $\pm 51.7°$, high statistics measurements of the cosmic ray fluxes in the rigidity range $0.1 - 200\,GV$ [139, 140, 141, 142]. AMS01 measurements allowed to set a limit 1.1×10^{-6} on the $\overline{He}/He$ ratio in the cosmic rays flux [71].

In this work we are interested to the high statistics measurements of protons, electrons and positrons made by AMS01, since they can be used to evaluate how precisely our simulation can reproduce the physics of the interactions of primary cosmic rays with the atmosphere and the composition of secondary fluxes in the near Earth environment.

In the first section we describe the features of the AMS01 detector, in the second section we illustrate the measurement conditions in which AMS01 was operating during the Space Shuttle mission, in the last section the AMS01 measurements are reviewed separately for proton data and for electron and positron data.

4.1 The detector

AMS01 is a magnetic spectrometer designed to measure with highest accuracy the cosmic rays flux in the range of rigidity $0.1 - 200\,GV$, to search for antimatter nuclei and to measure other rare components of the cosmic rays flux.

It is a detector of compact design comprising different subdetectors (see

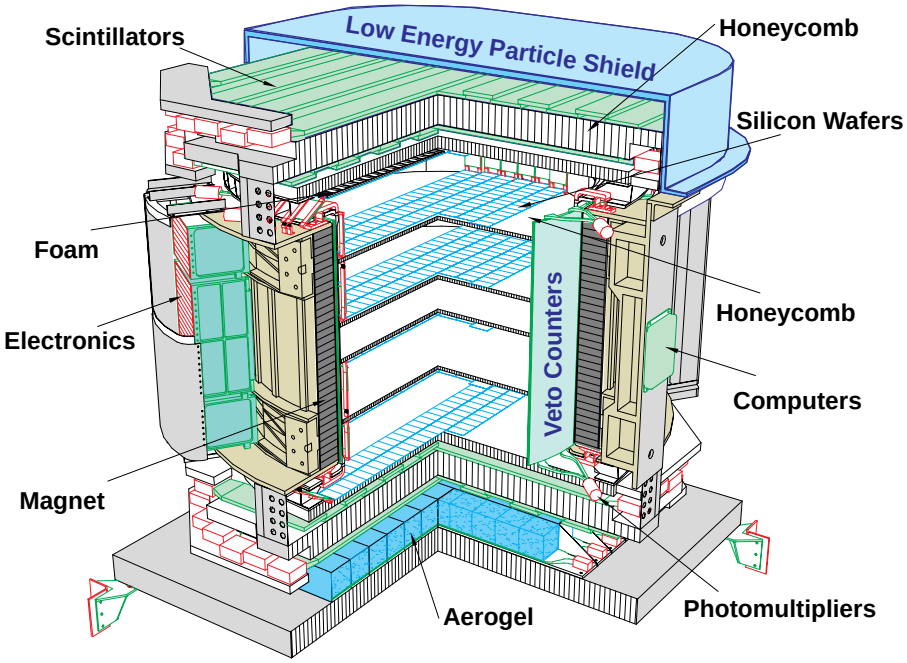

Figure 4.1: The AMS detector.

fig. 4.1), which allows an accurate measurement of the particle rigidity, velocity and charge, needed for a good particle identification.
Three main subdetectors are arranged around a cylindrical permanent magnet that guarantees a field perpendicular to the cylinder axis and with a strength of $0.14\,T$ at the center:

The silicon tracker: Six planes of microstrip silicon detectors placed in the magnet bore allow the measurement of the particle rigidity through the curvature of the trajectory in the magnetic field. They also give up to six independent measurements of the particle charge through the energy released in each plane.

The time of flight detector (ToF): Two pairs of planes of scintillator detectors placed at both ends of the magnet, allow the measurement of the time of flight of the particle with a resolution of $120\,ps$. The ToF detector provides the fast trigger signal and an independent measurement of the particle charge through the evaluation of the energy released in the scintillators planes.

The aerogel threshold Çerenkov detector (ATC): placed at the bottom of the magnet, below the last plane of the ToF allows a better $\overline{p}/e^-$

and p/e^+ discrimination for protons and antiprotons with momentum up to $3.51\,GeV/c$.

A veto system using scintillators placed on the inner magnet walls completes the detector. A low energy particle shield enclose the top part of the detector to prevent the trigger to be saturated by low energy particles. In the following the features and the performances of the magnet and of the various subdetectors are illustrated.

4.1.1 The magnet

The permanent magnet has cylindrical shape with an height of $800\,mm$, an inner diameter of $1115\,mm$ and an outer diameter of $1298\,mm$ resulting in a geometrical acceptance of $0.82\,m^2sr$. The total weight, including the support structures, is $2.2\,tons$.

The magnet design has to satisfy opposite requirements: a) to be light weight and of large acceptance; b) to have a large bending power and sufficient homogeneity of the magnetic field in the entire tracking volume; c) to have a very small magnetic flux leakage outside the magnet in order not to have influence on Space Shuttle navigation and instrumentation.

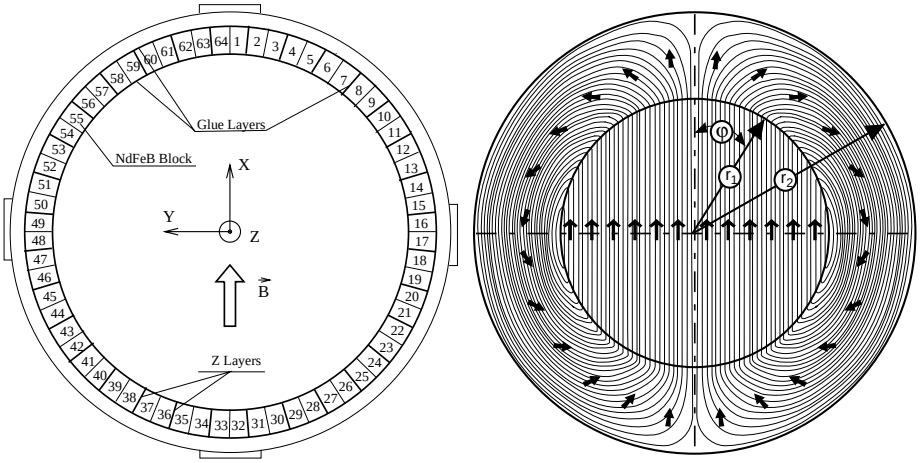

Figure 4.2: The layout of AMS01 magnet.

The solution adopted is a modular construction made of 64 sectors, each one composed of 100 $2'' \times 2'' \times 1''$ high grade $ND-Fe-B$ blocks. Figure 4.2 shows the arrangement of the field direction of the 64 sectors. The resulting cylindrical magnet shell has a magnetization vector constant in magnitude and oriented according to the formula:

$$\alpha = 2\,\phi + \frac{\pi}{2} \tag{4.1}$$

where ϕ is the angular cylindrical coordinate. Such a distribution gives an interior field of:

$$B = B_r \, ln\left(\frac{r_1}{r_2}\right) \tag{4.2}$$

where B_r is the residual flux density of the ring and r_1 and r_2 are respectively its inner and outer radius. The magnetic field is directed orthogonally to the cylinder axis and the maximum bending power of the magnet is $BL^2 = 0.15\,Tm^2$. The field quickly drops outside the magnet to become less than $3\,Gauss$ anywhere at distance of $2\,m$ from the magnet center.

4.1.2 The Time of Flight (ToF) detector

The time of flight detector is composed of two pairs of scintillator detectors placed at the top and at the bottom of the magnet. The two planes composing each pair are disposed orthogonally to allow the measurement of both coordinates in the plane. Each plane is composed of 14 plastic (BC-408) slabs, $11\,cm$ wide and of length variable from 72 to $136\,cm$, according to their location within the circular structure. To minimize the dead space there is an overlap of $5\,mm$ between adjacent slabs. Each scintillator is viewed by two groups of three photomultipliers, one each side.

The absolute time of traversal of a particle through a ToF plane is obtained from the average value of the measurements of the two sides of a counter, t_1 and t_2,

$$t = \frac{t_1 + t_2}{2} \tag{4.3}$$

while the position along the x- or y-coordinate is calculated by the difference $t_1 - t_2$, given the effective velocity of the light in the scintillator material, $v_{eff} = 15.5\,cm/ns$:

$$x = v_{eff}\frac{t_1 - t_2}{2} \tag{4.4}$$

The obtained spatial resolution is $\sigma_s \leq 2\,cm$, the time measurement provided by the ToF system has a resolution better than about $120\,ps$ [135]. The minimum time of flight of relativistic particles passing through AMS is determined by the distance between the two pairs of ToF planes (L), about $150\,cm$:

$$\beta = \frac{v}{c} = \frac{L/t}{c} \simeq \frac{150\,cm}{t}\,\frac{1}{30\,cm/ns} = \frac{5\,ns}{t} \tag{4.5}$$

The energy released by a charged particles in the plastic scintillator follows a Z^2 dependance. It is then possible to measure the absolute value of the charge of a particle $|Z|$ from the amplitude of the photomultipliers signals.

4.1.3 The silicon tracker

Silicon detectors, commonly used as tracking devices in accelerator experiments, offer the best resolution in terms of position measurement. The first

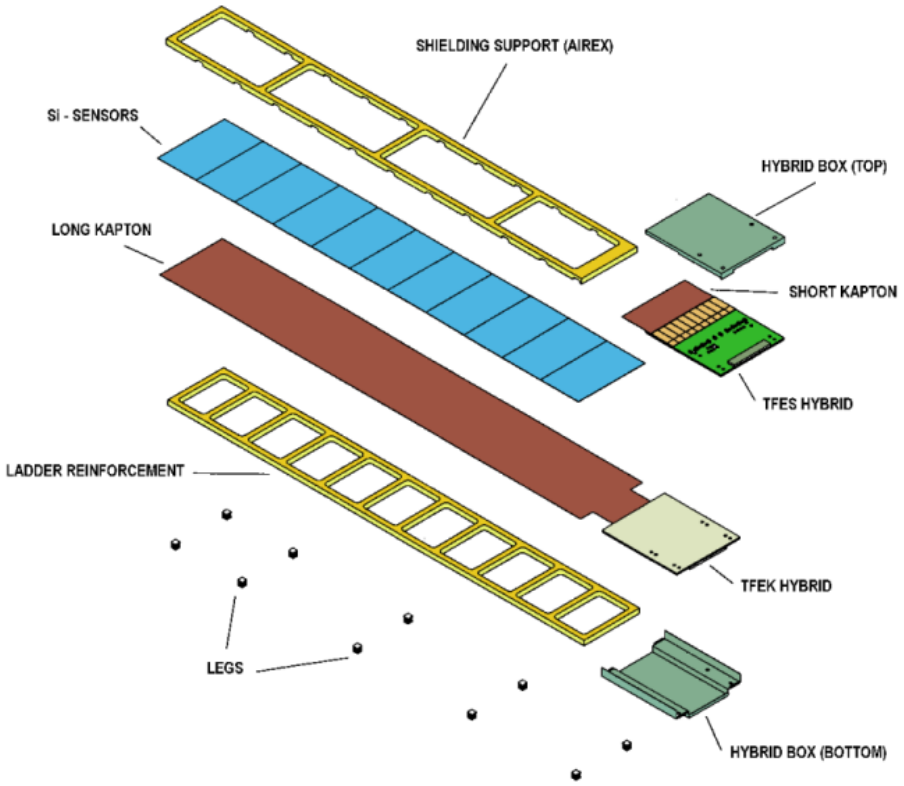

Figure 4.3: Exploded view of a ladder.

large scale application of these devices in space was successfully done with AMS01.

The AMS01 tracker consists of six planes of silicon sensors providing $10\,\mu m$ ($30\,\mu m$) position resolution in the bending (non-bending) plane of the magnet. During the flight on board the Space Shuttle Discovery only the central part of each plane was instrumented as shown in fig. 4.1.

The sensor design is based on the one used for the ALEPH and L3 micro-vertex detectors [136] at the Large Electron-Positron collider (LEP) at CERN. The sensor are double-sided micro-strip detectors $300\,\mu m$ thick and with area $40.1 \times 72.04\,mm^2$. The readout strip pitches are: $110\,\mu m$ for the Y-coordinate p-side (bending plane) and $208\,\mu m$ for the X-coordinate n-side (not bending plane).

Silicon sensors are grouped together in ladders of various lengths (7 to 15 sensors) to match the cylindrical geometry of the magnet, the maximum length of silicon for a single readout channel reaching $60\,cm$. Figure 4.3 is showing an exploded view of a ladder. There are in total 28 ladders on the inner layers and 34 ladders on the outer ones. All the ladders are supported by ultra-light honeycomb planes: the total amount of material between plane

1 and 6 is about 3.2% of a radiation length for normal incident tracks [137].

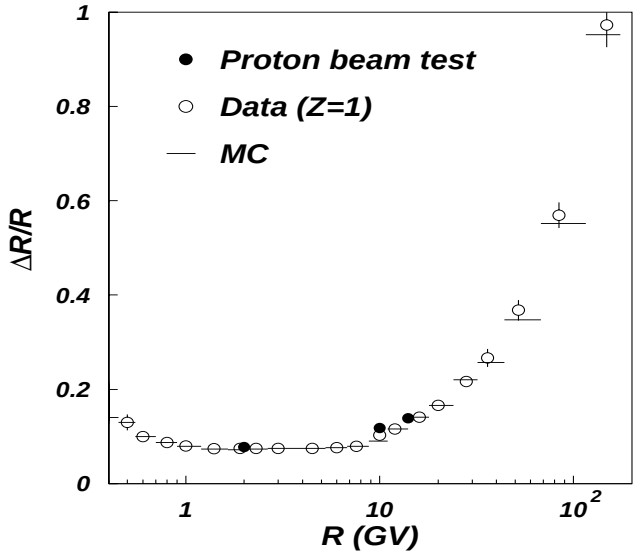

Figure 4.4: Rigidity resolution averaged over tracks with 4,5, and 6 points for Z=1. Open circles are representing flight data, black circles are data obtained in a test beam, and horizontal lines are the results of a Monte Carlo simulation. On the vertical axis is shown $\Delta R/R = (R_{measured} - R_{beam})/R_{beam}$.

Particle trajectories are reconstructed by matching the location of the energy losses (hits) in each one of the six tracker planes. The track reconstruction, made with non linear adaptive fits procedures [138], allows the determination of the rigidity $R = pc/|Z|e$ where p is the momentum, Ze is the charge of the particle. For low rigidity particles (up to $\sim 10\,GeV$) the spectrometer resolution is limited by multiple scattering, while at higher energies the tracker spatial resolution and the spectrometer bending power are the limiting factors. Figure 4.4 shows the dependence of the resolution as function of the rigidity.

The tracker provides also the main determination of the absolute value of the particle charge. The energy released in each silicon sensor is proportional to the square of the charge of the particle; a special electronic readout system has been designed to identify the particle charge up to $Z = 14$.

4.1.4 The aerogel threshold Çerenkov counter (ATC)

The ATC detector is composed of 168 independent aerogel modules arranged in two layers. In order to minimize the signal loss, the two layers are offset and supported, above and below, by a $50\,mm$ honeycomb plane.

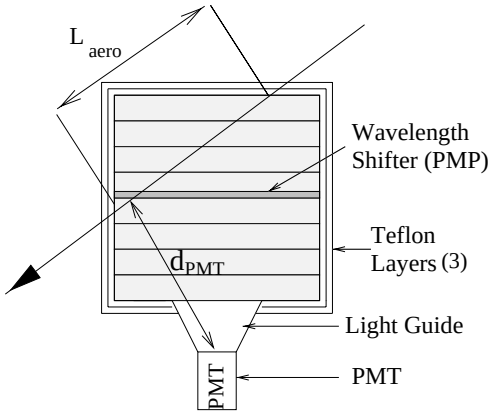

Figure 4.5: Sketch of an Aerogel Threshold Çerenkov counter module, showing the trajectory of a particle traversing L_{aero} material at distance d_{PMT} from the center of photomultiplier.

The basic module (fig. 4.5) has dimensions $11 \times 11 \times 8.8\,cm^3$ and consists of 8 aerogel slats, $1\,cm$ thick, viewed by a phototube. The emitted photons are reflected by three $250\,\mu m$ teflon layers surrounding the aerogel blocks, until they reach the window of the photomultiplier. A wavelength shifter placed between the aerogel slats allows to shift the wavelength of the Çerenkov photons into the window of maximal efficiency for the photomultiplier improving the performance of the detector.

The aerogel threshold Çerenkov counter (ATC) extends the range of particle identification beyond the limit set by the time of flight measurements. Table 4.1 shows the Çerenkov thresholds for the chosen radiator. Above these thresholds the particles are emitting Çerenkov light in the aerogel radiator, so for example below $3.51\,GeV$ it is possible to discriminate between protons and positrons because the former does not trigger the ATC while the latter does.

$Particle$	$e^{\pm}$	$\pi^{\pm}$	$p\,\bar{p}$	$He\,\overline{He}$
P_{thres}	$1.91\,MeV/c$	$0.52\,GeV/c$	$3.51\,GeV/c$	$14.0\,GeV/c$

Table 4.1: Threshold momentum for different particle species in the ATC.

4.2 The Shuttle mission

AMS01 flew onboard the Space Shuttle Discovery during the STS-91 mission which lasted 10 days (June 2nd-12th 1998). The primary goal of the Shuttle flight was the last docking with the Russian Space Station Mir.

The Shuttle flew on a 51.7° inclined orbit at an average altitude of $\sim 390\,Km$. AMS data were collected during all flight, but the mission was optimized for the AMS data taking only before docking and after the separation from Mir, for a total of 111 hours. Throughout the docking period, the Shuttle Discovery was in the shadow of Mir. This period is not useful for most AMS scientific analysis (see fig. 4.6).

During the flight AMS was pointing with different attitudes with respect the zenith: 0° (zenith), 20°, 45° and 180° (nadir direction).

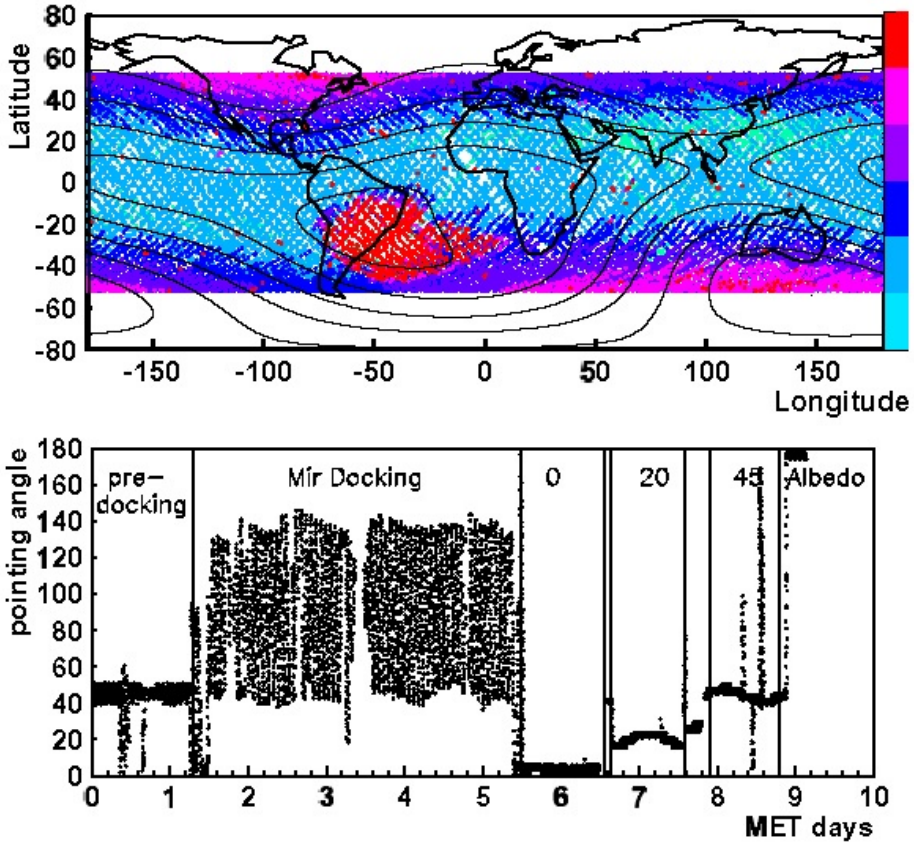

Figure 4.6: Upper plot, the AMS orbit coverage: the different colors correspond to different cosmic rays rates, lower at the equator and larger close to the poles, to be noted the large rate in the SAA zone. Lower plot: shuttle attitudes during the mission as a function of the Mission Elapsed Time (MET).

The data collected in the area enclosed between $-57° \div 0°$ in latitude and $-85° \div 23°$ in longitude, corresponding to roughly the South Atlantic Anomaly, are excluded from the AMS analysis because of the high rate of particles and the consequent low live time of the data acquisition chain.

In this work we are interested in the measurements of the proton and electron and positron fluxes at zenith and nadir attitudes.

4.3 AMS Measurements of protons and leptons fluxes in near Earth orbit

4.3.1 Proton data

The analysis of the AMS measurements of proton fluxes has been published in [139, 140]. Here we report details relevant for the comparison with our simulation as discussed in the chapter 5.

In the energy range covered by AMS, protons are constituting the largely dominant component of both cosmic rays primary and secondary particle flux. They are easily separated from electrons by their different charge sign, and the consequent different curvature in the detector magnetic field, up to rigidities $R \simeq 200\,GV$. They are well distinguished from the He component by an efficient charge separation among events with $|Z| = 1$ and events with $|Z| > 2$.

The reconstructed particle mass is required to be within 3 standard deviations of the proton mass. This cut rejected about 3% of the events while reducing the background contamination to negligible levels at all the energies.

Given the asymmetric layout of the tracker the acceptance has a dependance on the azimuth and the zenith angles. Acceptance was determined through a Monte Carlo simulation: it results to be $0.15\,m^2$ on average varying from 0.3 to $0.03\,m^2$ with the incident angle and location, while it is only weakly momentum dependent. The acceptance was corrected following an analysis of unbiased trigger events. For the proton data analysis, acceptance was restricted to events with an incident angle within 32° of the AMS axis.

AMS data on protons are presented in 10 bins (fig. 4.7) of geomagnetic latitude, both for the downgoing or zenith flux, and the upgoing or nadir flux. Zenith flux measurements are showing the primary cosmic rays flux and the geomagnetic latitude dependence on the geomagnetic cutoff effect. Below the cutoff the flux of protons rises again forming a second spectrum. The nadir measurements reveal a spectrum of under cutoff particles with the same shape and intensity as for zenith suggesting that these protons are secondary products of the cosmic rays interactions with the atmosphere.

The origin of the under cutoff particles has been investigated tracing a sub-sample of the observed data, back and forth from the point of observation until one of the following conditions is satisfied: a time limit of 30 s of flight time is reached, or the particle reaches the altitude of 40 Km assumed as typical altitude of interaction in the atmosphere. This determines the point of origin of the under cutoff particle together with the point of

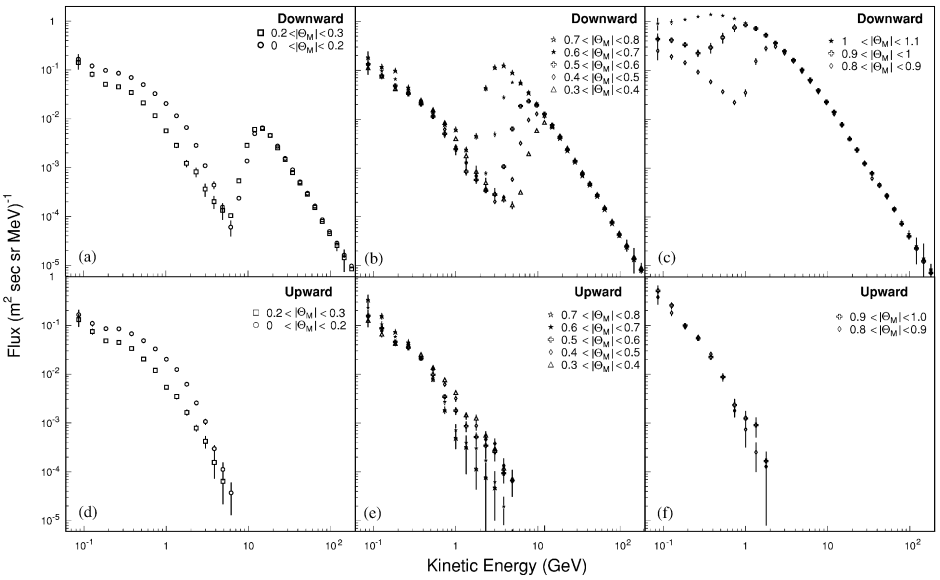

Figure 4.7: The AMS measured proton flux at different magnetic latitude θ_M for zenith (downward) and nadir (upward) attitudes of the Shuttle.

absorption in the atmosphere.

Figure 4.8 shows the distribution of the life time of the secondary particles between the origin and absorption points versus their kinetic energy. Two different population can be observed: the first (short-lived) characterized by a life time smaller the 0.3 s and no dependence on the energy, and the second (long-lived) characterized by a life time up to $\sim 30s$ and a clear correlation with the kinetic energy.

Figure 4.9 shows the map of the points of origin and absorption in the atmosphere for the long-lived component (lower plot) and for the short-lived component (upper-plot). The map of absorption point for the short-lived component is similar to the one of points of origin but is not shown.

From figure 4.9 one sees that the two components show different features having a complete different pattern of origin and absorption points. Such behavior will be discussed in chapter 5.

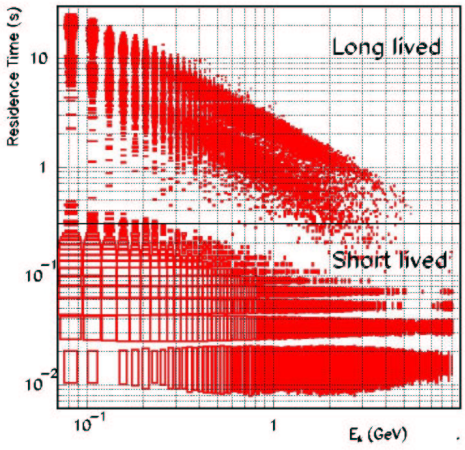

Figure 4.8: Life time of the under cutoff protons measured by AMS for $|\theta_M| < 0.3$. Life time is defined as the time between the particle production and its re-interaction with the atmosphere.

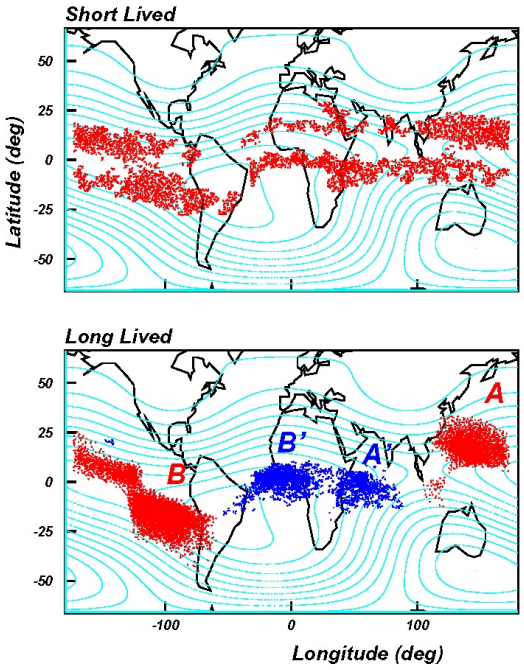

Figure 4.9: Top: geographical origin of short lived protons detected at $|\theta_M| < 0.3$. Bottom: The geographical origin and point of absorption of long lived protons detected at $|\theta_M| < 0.3$. Particles originated at 40 Km from two main locations (A and B), impinging into the atmosphere at the same altitude but in two distinct regions (A' and B').

4.3.2 Electron and positron data

The analysis of the AMS measurements of electron and positron fluxes has been published in [141]. We report here the details relevant for the comparison with our simulation illustrated in chapter 5.

Electron candidates were specifically selected by requiring the measured particle charge to be -1 and the particle velocity to be compatible with the speed of light. Backgrounds arose from protons with wrongly measured momentum and secondary pions produced in the detector materials. The two most important cuts used to remove these backgrounds were: (a) on the χ^2 value obtained in fitting the particle trajectory, which removed tracks with large single or multiple scattering, and (b) on the number of hits near the reconstructed trajectory in both the tracker and time of flight scintillators. After the above cuts were applied, the overall probability of a proton event to be accepted as an electron, estimated from Monte Carlo simulations and confirmed in the CERN test beam, was $O(10^{-4})$ with an electron selection efficiency of 75%. To further reduce the pion background only events whose track passed through the active Çerenkov counter area and, therefore, had an independent velocity measurement, were accepted.

Positron candidates were selected by requiring: the charge to be +1 and, as for electrons, the velocity be compatible with the speed of light and track quality cuts. In contrast to electrons, the main background for the positron sample came from proton events with poorly measured velocity. The rejection power against this background decreased rapidly with increasing proton momentum, therefore tighter quality cuts on the velocity measurements were applied. Above $1\,GeV/c$ protons were rejected by requiring the two independent velocity measurements from the two separate Cerenkov counter layers to be compatible with the velocity of a positron. The separation between positrons and protons has been possible up to $3\,GeV$. Lower energy protons were rejected by requiring the energy loss measurements in the four layers of the Time of Flight counters and six double layers of Silicon Tracker to be compatible with a positron. These cuts yielded an additional background rejection factor of 5 at the expense of lower positron selection efficiency.

For both electrons and positrons, the acceptance was determined as a function of particle momentum and direction. The average acceptance is energy dependent and rises from about $0.01\,m^2\,sr$ at $0.15\,GeV$ up to $0.1\,m^2\,sr$ at $0.7\,GeV$. Above that energy it remain almost constant with a systematic uncertainty of 5%. The incident differential spectrum was obtained from the measured spectrum by using an unfolding method based on Bayes' theorem [129] with resolution functions obtained from the simulation. These functions were confirmed at several energy points with calibration measurements in the CERN proton beams.

In figure 4.11 the downward and upward lepton fluxes integrated over incident angles within 25° of the AMS axis are shown in six intervals of

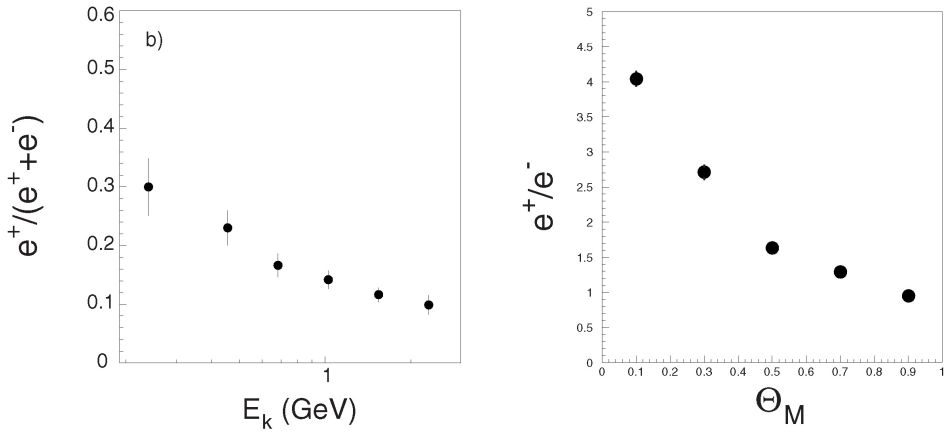

Figure 4.10: Left plot: fraction of positrons in the primary flux with respect the e^- and e^+ total flux expressed as a function of the kinetic energy. Right plot: ratio positron/electron under cutoff fluxes as function of the geomagnetic latitude.

geomagnetic latitude. The effect of the geomagnetic cutoff and its decrease with increasing θ_M is particulary visible on the downward electron spectra. As in the case of protons a substantial under cutoff spectrum is observed for both e^- and e^+. Furthermore, upward and downward under cutoff fluxes result of equal intensity.

As for the proton case, electrons and positrons have been traced backward and forward from the detection points until: they reach the time limit of 30 s or they reach the altitude of 40 Km a.s.l. assumed as the limit of the atmosphere.

The live time and absorption points are shown in figures 4.12, 4.13 and 4.14. Plots for the origin points are similar and are not shown. As in the case of protons the under cutoff populations can be divided in short and long lived components, which are presenting different geographical distributions of origin and impacts points on the atmosphere.

Another interesting feature observed on the lepton second spectra is the predominance of positrons over electrons. Figure 4.10 shows (right plot) the ratio positrons to electrons of the integrated under cutoff spectra, a net excess of positrons is observed in the equatorial region, which gradually disappears approaching the polar region.

The origin of the observed features on the lepton spectra are discussed in chapter 5.

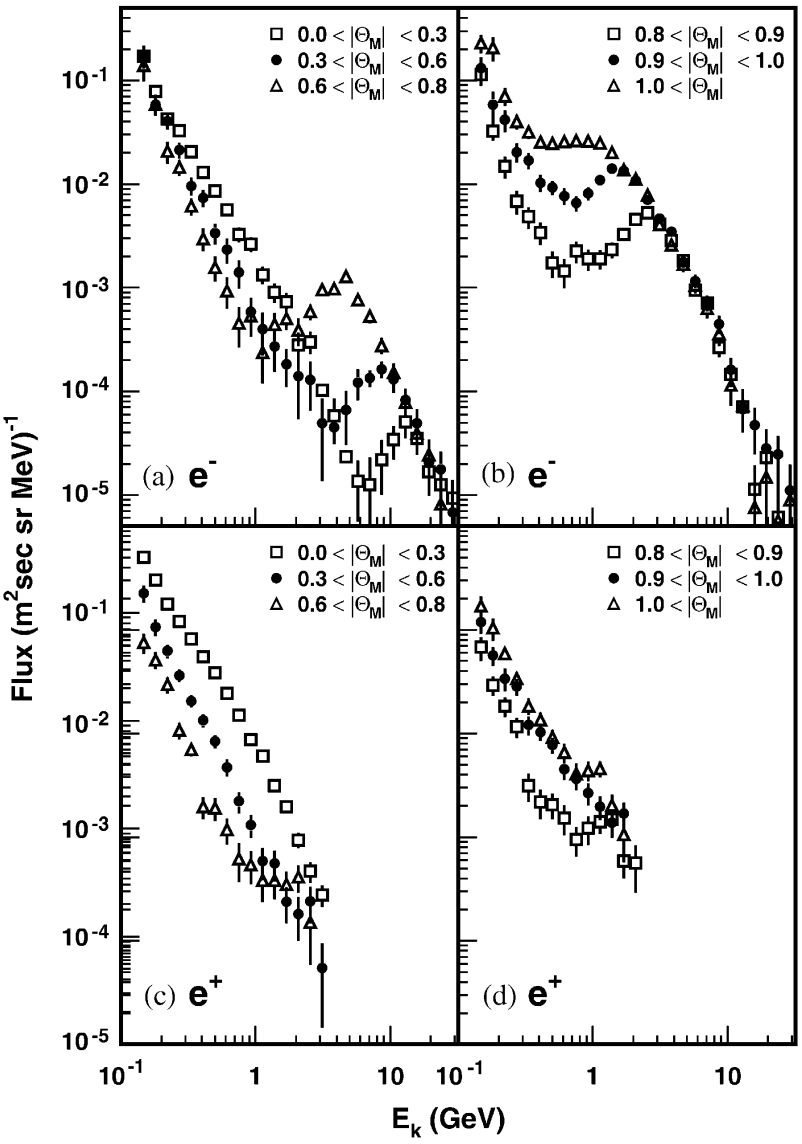

Figure 4.11: The AMS lepton measured flux.

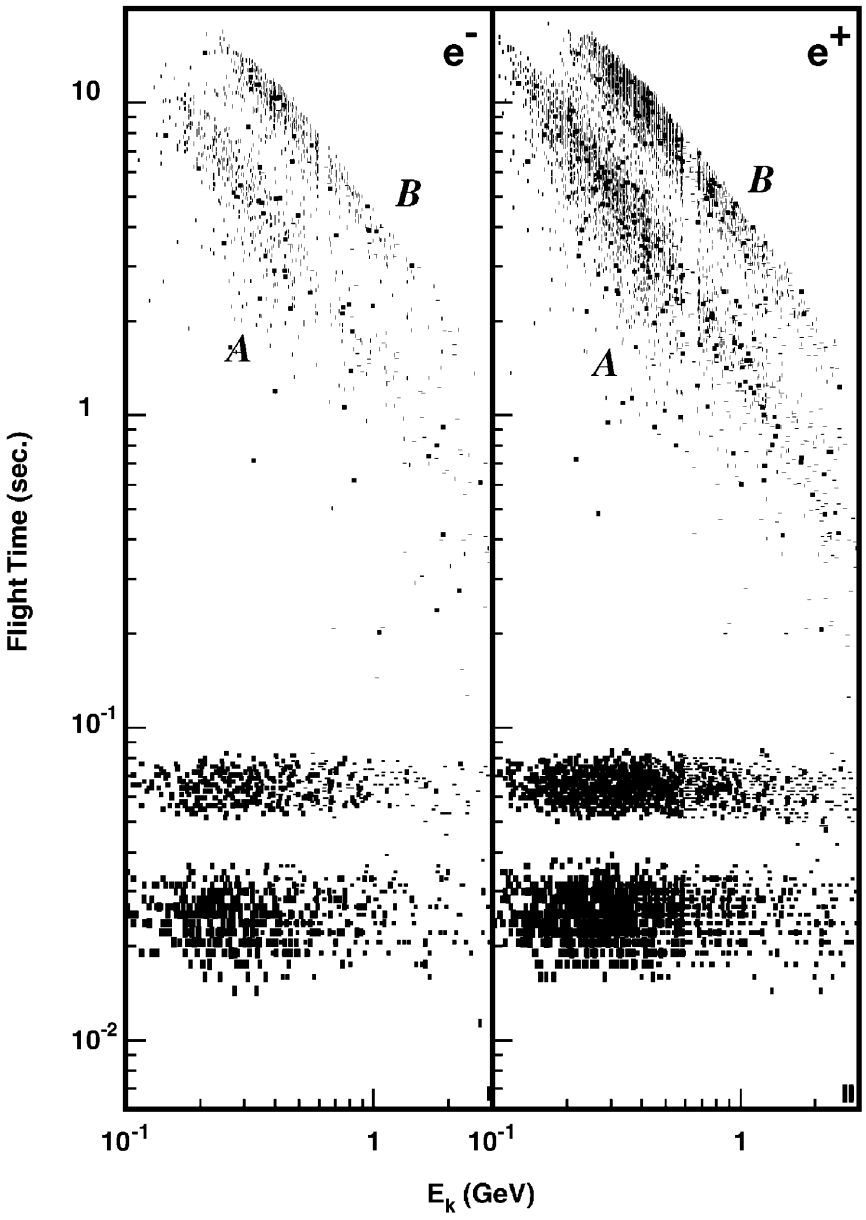

Figure 4.12: Life time of the secondary electrons and positrons measured by AMS for $|\theta_M| < 0.3$.

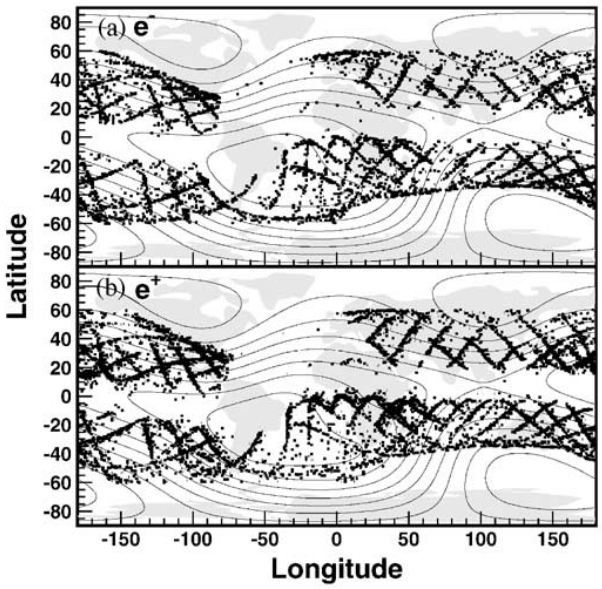

Figure 4.13: Maps of absorption points of short lived electrons and positrons measured by AMS for $|\theta_M| < 0.3$.

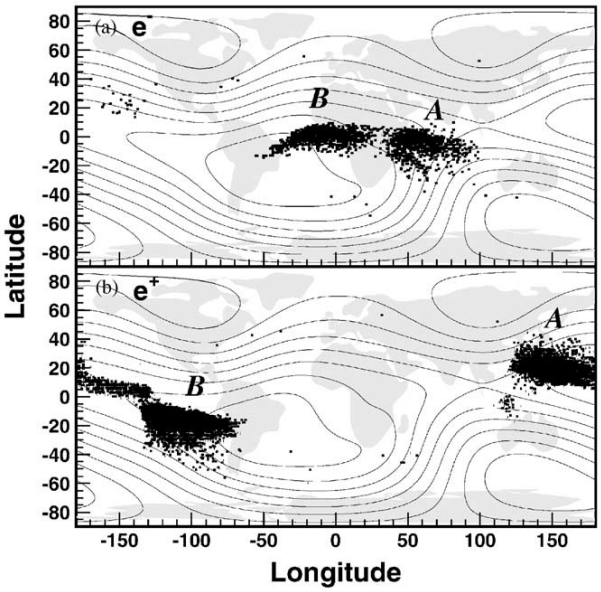

Figure 4.14: Maps of absorption points of long lived electrons and positrons measured by AMS for $|\theta_M| < 0.3$.

Chapter 5

Monte Carlo simulation results

In this chapter we validate our Monte Carlo simulation and critically discuss its limits through a comparison with the AMS measurements of proton and $e^{\pm}$ fluxes in Low Earth Orbit. In the first section the conceptual differences among our model of flux and its experimental determination are discussed. We then separately review the AMS proton and $e^{\pm}$ measurements discussing the sources and the dynamical processes underlying the experimentally observed distributions. We conclude with a brief discussion on the relevance of our simulation for a better comprehension of the near earth radiation environment.

5.1 The flux measurement

The AMS flux measurements are performed with a point-like detector[1], with a limited field of view, recording at different times in different space points a steady flux of primary CR and under-cutoff particles. The same logic, if strictly applied in our simulation, would lead to a high degree of inefficiency and prohibitive waste of computing time. In fact, it would require to fully simulate a number of events equivalent to the incident CR flux over the whole Earth for the 10 days of the AMS flight, with only an extremely small fraction reaching the detector.

We therefore implemented a more efficient approach. But this requires, for a direct comparison of the AMS data with the results of our simulation, a careful discussion on what we assume as a *detector* and what are the conceptual differences underlying the flux definition used in our simulation with respect the AMS measurements.

The measured flux reported by AMS in a specific interval of geomagnetic

[1] with respect to the size of the Earth surface.

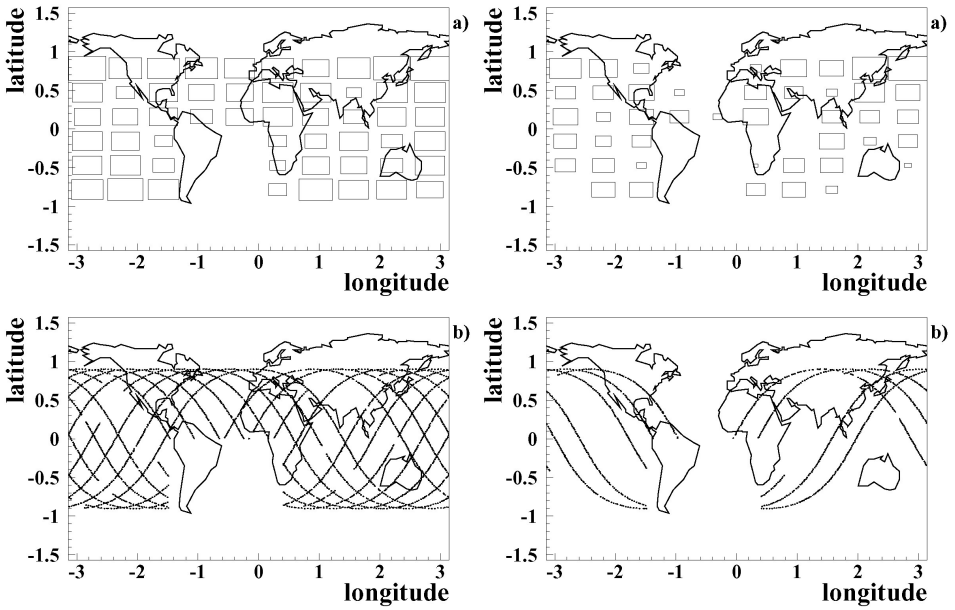

Figure 5.1: Time exposure (a) and orbital coverage (b) of the AMS experiment for attitudes pointing to zenith (left) and nadir (right).

latitudes [2] is effectively defined as:

$$\Phi = \frac{\sum_i N_i^{obs} \cdot C_i}{\sum_i \Delta t_i} \tag{5.1}$$

where N_i^{obs} and Δt_i are the number of counts and the observation time in a given spatial position, respectively, and C_i includes both the geometric acceptance and the efficiency factors. The index i runs over all measurements done when the AMS position falls in the selected range of geomagnetic latitudes. Given a flux which in general depends on the latitude and longitude, the quantity defined in 5.1 is truly representative of the mean flux within the selected latitude range, only for an uniform sampling of the region with comparable exposure times in different locations. This condition is partially satisfied for data taken with AMS pointing to the zenith while a much looser coverage characterizes data taken during the nadir pointing. In fig. 5.1a the time spent by AMS in different regions is mapped in geographical coordinates. The size of the boxes superimposed on the globe is proportional to the time spent by AMS in the corresponding bin of geographical longitude and latitude. The corresponding orbits are illustrated in fig. 5.1b. The

[2] In this chapter we use the term geomagnetic latitude (longitude) as short form for *corrected* geomagnetic latitude (longitude).

left plots are relative to the shuttle orbits with AMS pointing to zenith, the same quantities are shown on the right for AMS pointing to nadir. In all plots the orbits in the region of the South Atlantic Anomaly have not been taken in account.

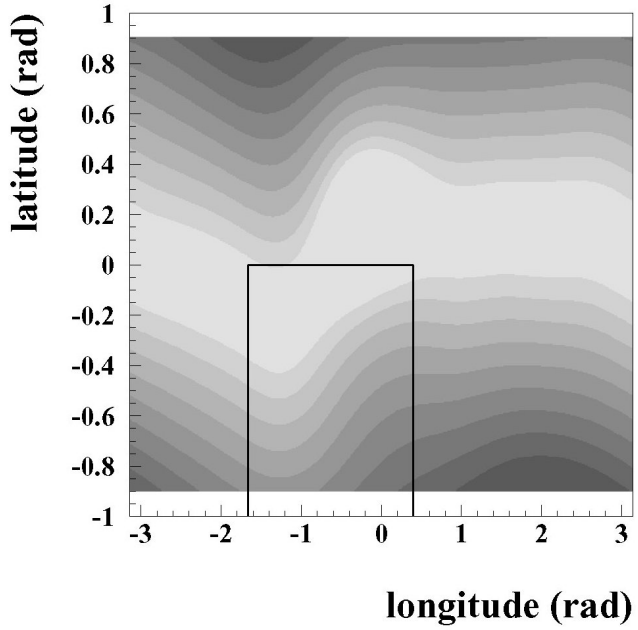

Figure 5.2: Representation in geographical coordinates of the different surfaces corresponding to the geomagnetic latitude intervals adopted in the AMS measurements. See text for a more detailed discussion.

In our simulation we operate on an event by event basis: we fire a primary cosmic ray, let it eventually interact with the atmosphere and then we follow the motion of the secondaries in the geomagnetic field. The detection boundary is defined by a geocentered spherical surface with a radius matching the average altitude of the AMS orbit. Each time a particle, primary or secondary, intersects this surface all the information about its nature and its motion are recorded. A boundary crossing becomes a *count* in our detector if it occurs in a region covered by the AMS measurement and with a particle direction with respect to the zenith or nadir within the angular acceptance of AMS.

The size of our detector for a flux measurement in a given geomagnetic latitude range is therefore defined by the area delimited on the surface of the detection sphere by the corresponding parallels in geomagnetic latitude. In fig. 5.2 the detector surfaces corresponding to the different intervals of the geomagnetic latitude used in AMS flux measurements are shown in geographical spherical coordinates. The same intensity in the gray scale has

been used for surfaces in the northern and southern hemispheres which contribute to the binning in the absolute value of geomagnetic latitude adopted by AMS. The superimposed rectangle delimits the South Atlantic Anomaly region excluded for AMS published results. The numerical values for the different areas (SAA excluded) are listed in tab. 5.1[3]

θ_M interval (radians)	Area (km^2)	$\delta A/A$ %	θ_M interval (radians)	Area (km^2)	$\delta A/A$ %
$\theta_M\| < 0.2$	$9.94\,10^7$	0.5%	$0.6 < \|\theta_M\| < 0.7$	$3.81\,10^7$	0.7%
$0.2 < \|\theta_M\| < 0.3$	$4.28\,10^7$	0.7%	$0.7 < \|\theta_M\| < 0.8$	$3.40\,10^7$	0.7%
$0.3 < \|\theta_M\| < 0.4$	$4.26\,10^7$	0.7%	$0.8 < \|\theta_M\| < 0.9$	$2.24\,10^7$	0.8%
$0.4 < \|\theta_M\| < 0.5$	$4.16\,10^7$	0.7%	$0.9 < \|\theta_M\| < 1.$	$1.48\,10^7$	0.9%
$0.5 < \|\theta_M\| < 0.6$	$4.02\,10^7$	0.7%	$\|\theta_M\| > 1$	$0.85\,10^7$	1.1%

Table 5.1: Area of the detector surfaces corresponding to the intervals of geomagnetic latitude adopted in the AMS flux measurements.

The mean flux within a geomagnetic latitude bin is then obtained summing all the counts registered within the AMS FoV cut. We then obtain the flux as:

$$\Phi = \sum_i \frac{N_i}{S\ \cos\theta_i\ \Delta\Omega\ \Delta t} \tag{5.2}$$

where:

i the index running on all counts in a given geomagnetic bin

θ_i is the angle between the zenith (nadir) and the particle momentum $\Delta\Omega = \pi(1 - \cos\theta_{MAX})$ is the solid angle integrated over the angular acceptance, i.e. the field of view of AMS

Δt is the equivalent exposure time for all generated events as defined in §3.2.3

S is the surface of our detecting area.

According to our definition (eq. 5.2), we have the same equivalent time exposure (§3.2.3) over all longitudes and latitudes in a given latitude interval: then what we reproduce in our simulation is a true mean flux. Large flux fluctuations in conjunction with the limited uniformity of the AMS exposure could potentially lead to a discrepancy among our fluxes and those reported by AMS.

[3]The quoted uncertainties in tab. 5.1 are relative to the accuracy of the numerical integration needed to evaluate them. In fact no analytical correspondence exists among geographical and geomagnetic coordinates and the computation has been performed by means of a grid, where the grid step has been chosen in order to get an accuracy better than 1%.

Another difference between the AMS measurement and our definition of measured flux should be stressed. Secondaries revealed in AMS will be in general produced by different primaries impinging in the atmosphere *before* the measurement, within a relatively large time window. The time needed by each secondary to reach the AMS detector sets the size of this window, which ranges from few milliseconds for short lived secondaries up to ~ 30 s for the long lived ones. In all cases, these time scales are much larger than the ETE of our simulation.

In our simulation, instead, we operate on an event by event basis. We record all the secondaries produced by the interaction of a given primary, we follow their motion along their whole *live time* and count all their intersections with the detecting sphere. In fact, the secondaries generated in the interaction of a single primary P_0 will arrive at different times ($T_1 < T_2 < ... < T_n$) on our detection sphere, but we treat them in our flux definition (eq. 5.2) as they were *simultaneous* counts in our detector at the time T_{event}. In real life, this would be equivalent to the situation in which $(P_1, ..., P_n)$ primaries with the same characteristics of P_0 would interact at different instants $(T_{event} - T_1, T_{event} - T_2, ..., T_{event} - T_n)$ giving then a simultaneous arrival of all secondaries at T_{event}.

Under the hypothesis of a steady flux of primaries, our logic is basically safe and allows to take into account in our simulation the presence of secondaries with residence times much larger than our ETE. However, as an undesirable side effect of our approach, a statistical correlation exists among all secondaries corresponding to the same primary interaction. Moreover, the same secondary can be multiply counted when traversing the detection sphere at successive instants, as discussed in §5.2.2.

The statistic of primary cosmic rays generated to compare with AMS data is equivalent to a time of $11.61\,ps$ for the H component and $16.92\,ps$ for the He component. This is equivalent respectively to $18.7\,10^6$ primary protons and $3.1\,10^6$ helium nuclei fired from our production shell placed at $500\,Km\ a.s.l.$.

5.2 The proton data

5.2.1 The overall flux

The comparison between AMS data and the proton fluxes calculated with our simulation at the AMS orbit is presented in figures 5.3 and 5.4, for the zenith and nadir directions, respectively. AMS data are drawn as full points, our simulation is the solid line histogram. The dashed line histograms are representing the contribution of atmospheric secondaries alone as calculated in our simulation.

Data are subdivided in the same intervals of geomagnetic latitude adopted in AMS. For zenith pointing data, this corresponds to 10 bins in the absolute

value of geomagnetic latitude ranging from equatorial ($0 \leq |\theta_M| \leq 0.2\ rad$) to nearly polar latitudes ($1 \leq |\theta_M| \sim 1.1\ rad$). For nadir pointing data, there is no AMS coverage for the most polar interval, so only the first 9 intervals can be discussed.

Figure 5.5 shows, for four selected geomagnetic latitude bins, the comparison of the nadir and zenith proton differential fluxes as a function of energy, as calculated in our simulation. As expected, no contribution from primary CR exists in the nadir fluxes, while the same flux intensity from secondaries is found for the nadir and zenith observations.

An overall good agreement between our simulation and AMS data is observed in the distributions of figs. 5.3, 5.4 and can be better appreciated in fig. 5.7, where, the ratio Monte Carlo over data for the zenith proton fluxes are shown. The two black lines in each plot are representing the $\pm 20\%$ band around unity.

Different aspects of our simulation are involved in the description of the observed fluxes at energies above, below and around the geomagnetic cutoff, corresponding to the dominance of different physical mechanisms. At energies well above the geomagnetic cutoff, the generation technique and the global normalization can be tested independently from other aspects of the simulation. At energies close to the geomagnetic cutoff, the complex structure of the penumbra is a severe test of our propagation of the cosmic flux to Earth. At energies well below cutoff, all the aspects of this simulation are simultaneously involved leading to a physical interpretation of the experimental results.

In the following, we will therefore separately discuss our results in the three portions of the energy spectra, with a dedicated section for the analysis of the under-cutoff component.

The above cutoff region At proton energies well above the geomagnetic cutoff the origin of the measured fluxes should be fully due to primaries, i.e. cosmic protons coming from deep space. Moreover, geomagnetic modulation of their energy spectra should be absent, i.e. their shape and normalization should not depend on geomagnetic latitude. These are the ideal conditions to verify the quality of our generation technique and the overall normalization, since the result of our simulation should coincide with the input flux.

Figure 5.6a shows the integral of the flux above $30\,GeV$ (I_{30}) as function of the geomagnetic latitude for both AMS data (open circles) and this simulation (open squares), compared with the integral of the function used in the generation of the primary flux (horizontal line). The simulated integral fluxes are fully compatible with the generation function within the statistical errors. Relative fluctuations at the percent level are observed, as expected from the small systematic contributions from the normalization procedure and detector area calculation. The spread of the AMS data points reflects

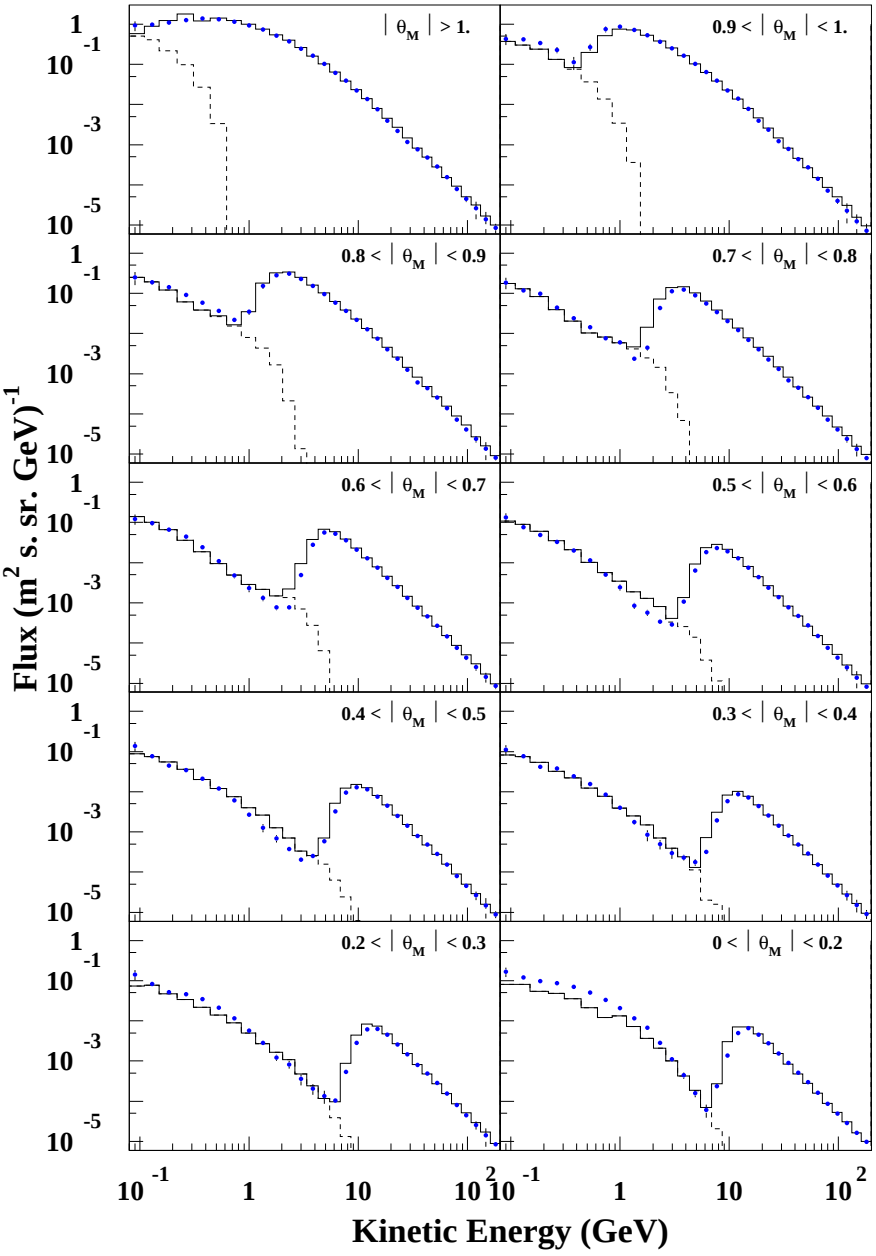

Figure 5.3: Proton differential flux as a function of kinetic energy measured at zenith by AMS (points) and calculated in our simulation (solid line). The different distributions correspond to separate intervals of geomagnetic latitude.

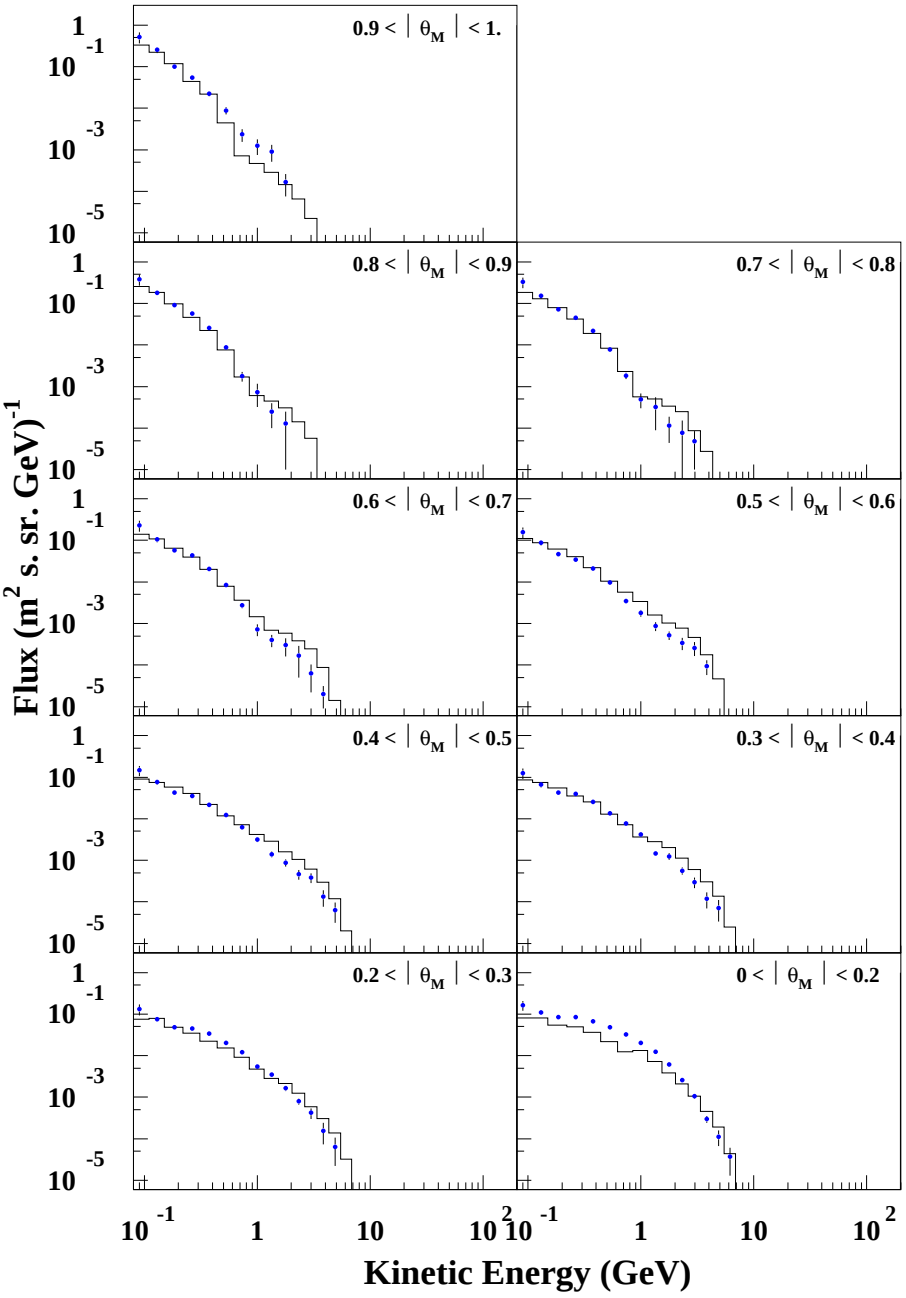

Figure 5.4: Proton differential flux as a function of kinetic energy measured at nadir by AMS (points) and calculated in our simulation (solid line). The different distributions correspond to separate intervals of geomagnetic latitude. Dotted line represents the secondary flux alone.

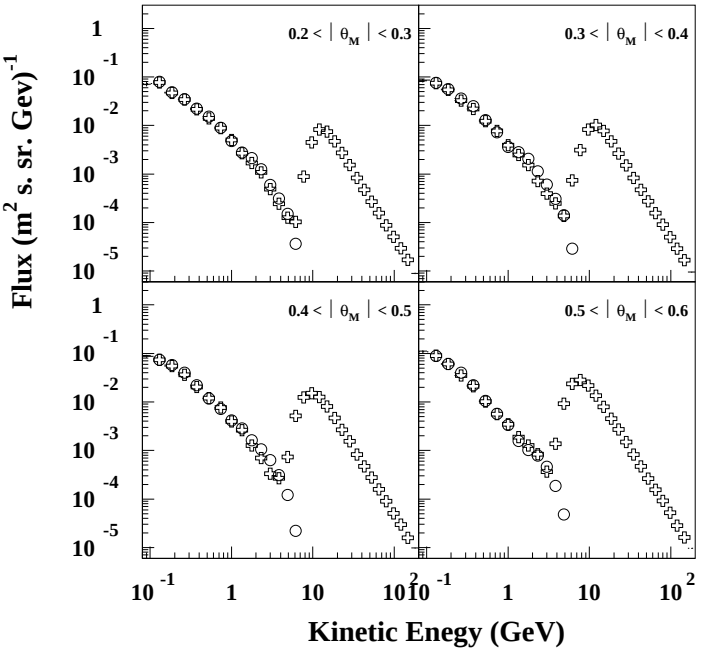

Figure 5.5: Proton differential flux as a function of kinetic energy at zenith (empty circles) and at nadir (crosses) predicted in our simulation. The different distributions are relative to separate intervals of geomagnetic latitude

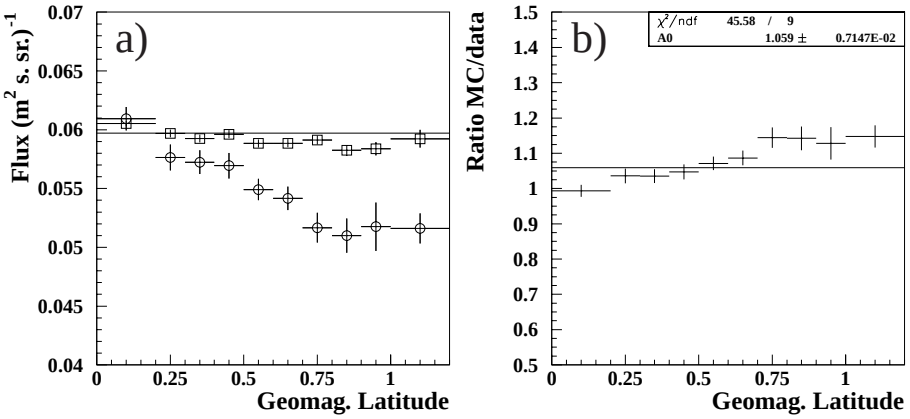

Figure 5.6: Left: the integrated proton flux above $30\,GeV$ plotted for AMS data (open circles) and this simulation (open squares). The horizontal line is the integral of the function used to generate the primary proton flux. Right: ratio simulation/data of the plots on the left side.

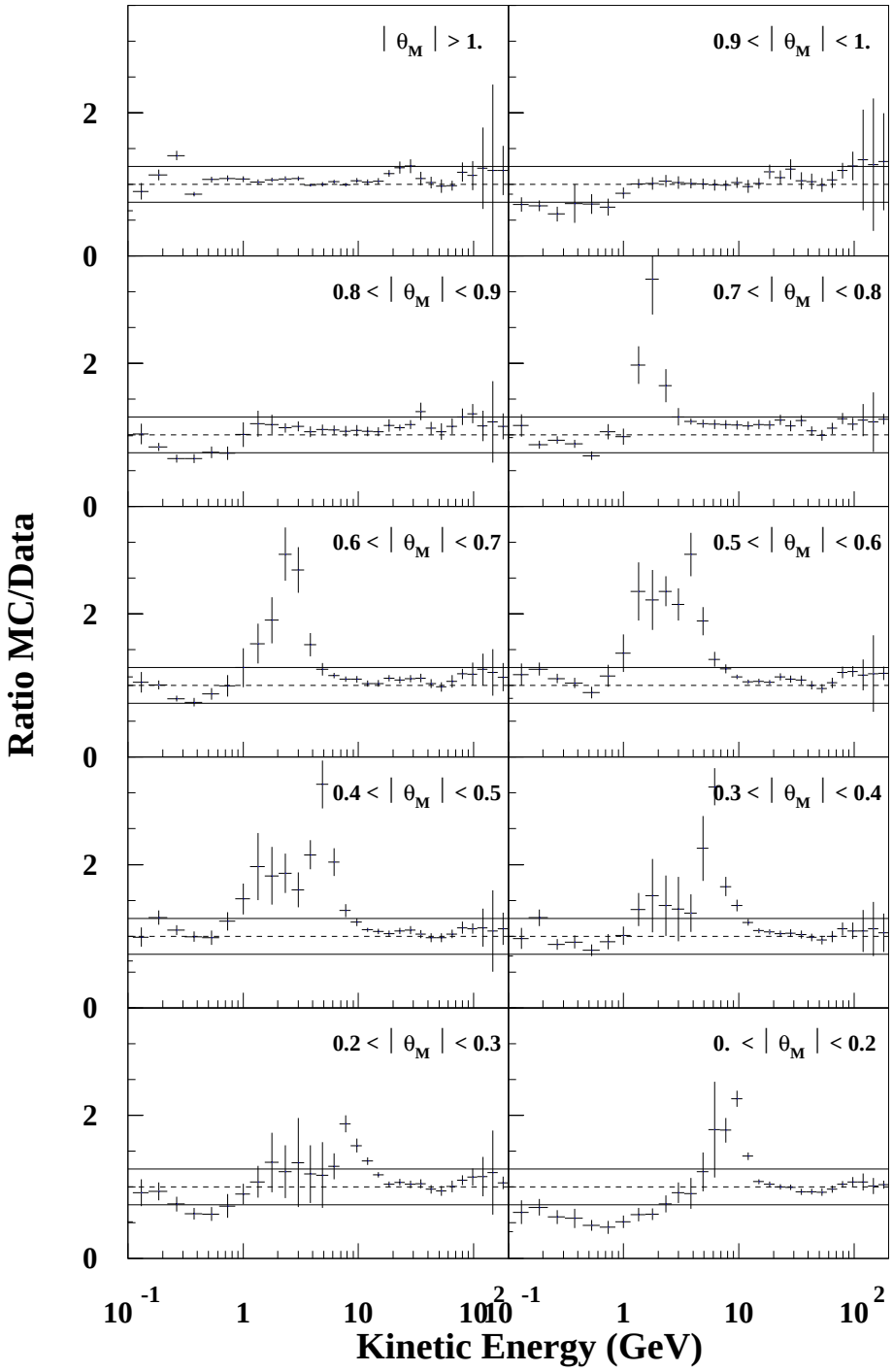

Figure 5.7: Monte Carlo over data ratio for differential energy spectra of protons at zenith. The different distributions are relative to separate intervals of geomagnetic latitude.

the systematic uncertainty on the flux measurements [139, 140].

Figure 5.6b shows the ratio (Monte Carlo over data) of the distributions presented in fig. 5.6a: the normalization of our simulation is on average 5.9% higher than AMS data (as our input spectrum is) with the latitude dependent behavior dominated by the systematic trend in the AMS measurements.

The near cutoff region We have already discussed in §2.3 the difficulties arising in an accurate and general definition of geomagnetic cutoff rigidity. In our discussion, we identify as *cutoff region* the portion of the energy spectrum where the transition occurs from a purely primary component of the flux at high energies to a purely secondary component at low energies. This region is the portion of the spectrum corresponding to the rise of the primary flux intensity after the deep observable in all the distributions, but in the most polar latitude interval, of fig. 5.3.

In the cut off region, the simulation results are in excess with respect AMS data in almost all the geomagnetic latitude bins, as shown in figure 5.7. Although this excess is accompanied by large statistical errors both in simulation and in data, it is worthwhile to discuss the limit of this simulation producing it.

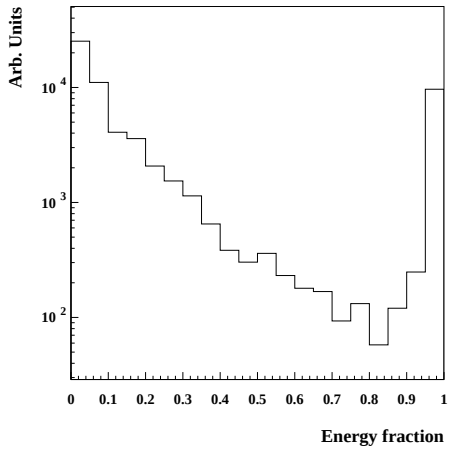

Figure 5.8: Distribution of the energy fraction carried by protons detected at 400 km coming from *unpacked* He nuclei. Refer to text for more details

This limit is relative to the naive implementation in FLUKA of the superposition model for He interactions with the atmosphere. In the generation phase, the He nuclei are exactly transported in the geomagnetic field to evaluate their access to atmosphere. However, as the limit of atmosphere is reached by the He nucleus, it is *unpacked* in its constituents. The resulting protons and neutrons are then separately followed in their trajectories

and interactions. The rigidities of the single nucleons - and therefore their trajectories in the magnetic field - will be different from that of the original He nucleus. This will finally result in unphysical effects if particles do not quickly interact after unpacking and if this happens at near cutoff rigidities, where even small changes in the rigidity can produce dramatic effects. In this case, unpacked nucleons can escape at 400 km along bounded/semi-bounded trajectories and contribute to the simulated fluxes. We verified the existence of this effect looking at the energies of secondary protons in our detector for events with primary He. Figure 5.8 is showing the distribution of the kinetic energy of such protons, normalized to 1/4 of the kinetic energy of the primary He nucleus. The peak near the unity is composed of the protons coming directly from the *unpacking* of a primary He nucleus.

A cut is applied at the value of the energy fraction of 0.95 to remove this component. Its effect on the proton spectrum at a given latitude interval can be seen in figure 5.9, where the proton spectrum is shown before (left) and after (right) the cut. The AMS data are superimposed as blue triangles. The observed excess in the simulation is then the residual component that survives the cut. From the figures, it can be also be seen how only the cutoff region is affected by this specific cut.

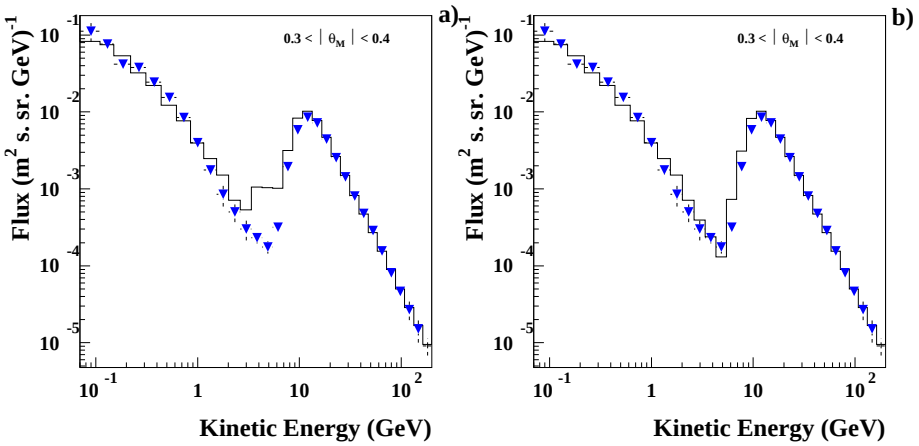

Figure 5.9: Proton fluxes predicted from the simulation (solid line) compared to AMS data (blue triangle) before (left) and after (right) the cut on the energy fraction. See text for more details

5.2.2 The under cutoff region

In our simulation, only secondary protons produced in the interactions of the primary cosmic rays with the atmosphere are populating the under cut-off region of the spectrum. The comparison with the observed fluxes in

this portion of the spectra is therefore relevant for an interpretation of the experimental data and to study the physical processes and the dynamical features at their origin. At the same time, any discrepancy arising in this comparison can be used to critically evaluate the limit of our approach.

Taking as references the distributions of figs. 5.3 and 5.7, and considering the relative normalization of our Monte Carlo with respect to data in the above cutoff region (fig. 5.6), the general trend exhibited by our simulation is an underestimation of the observed under cutoff flux. The effect is not dramatic, being at a level $< 20\%$ in most cases, and indeed partially expected from the approximations done in the representation of the cosmic ray flux (missing contributions of heavier nuclei in the primary flux, uncertainties in the slope of the H and He spectra). If compared with similar studies [107] [108], this is the most accurate description of the AMS under cutoff data obtained so far.

What we will discuss in the following are the peculiar features of the production and transport in the geomagnetic field of the under cutoff protons observed by AMS.

The production The under cutoff protons detected by AMS at 400 Km represent a tiny fraction of all secondaries produced in atmospheric interactions of cosmic rays. Conversely, most of the secondary protons are re-interacting in the atmosphere contributing to the generation of the cosmic ray initiated *air showers*. The escape of secondaries out of the atmosphere at the altitude of AMS orbit is a quite *rare* event indeed, and is limited to protons generated in the early stages of the shower development under peculiar kinematical conditions.

Quantitatively, in our simulation $85 \div 90\%$ of cosmic protons surviving the geomagnetic cutoff at 500 Km a.s.l. are interacting in atmosphere[4] but only $7 \div 8\%$ of them produces secondary protons detected in AMS. Of these protons, 46% results directly from the first CR interaction, 40% from the second and third interactions, the remaining 14% is produced in interactions up the fifth.

Looking at the atmospheric depth of the CR interaction and its kinematics, the sub-sample of primaries contributing to under cutoff proton fluxes seen by AMS (referred as P_e in the following) shows different characteristics with respect the whole CR primaries interacting in atmosphere (P_f).

Figure 5.10 shows, on the right plot, the altitude profile of the primary interactions for both samples. On the left, the distribution of the cosine of the angle between the momentum of the interacting primary and the local zenith is shown for P_e (dashed line) and P_f (solid line) samples. The mean altitude of the interactions is $36.5\,Km$ for P_e and $25.2\,Km$ for P_f. As

[4] the remaining $10 \div 16\%$ re-escapes along complex trajectories, and reaches, eventually, the deep space.

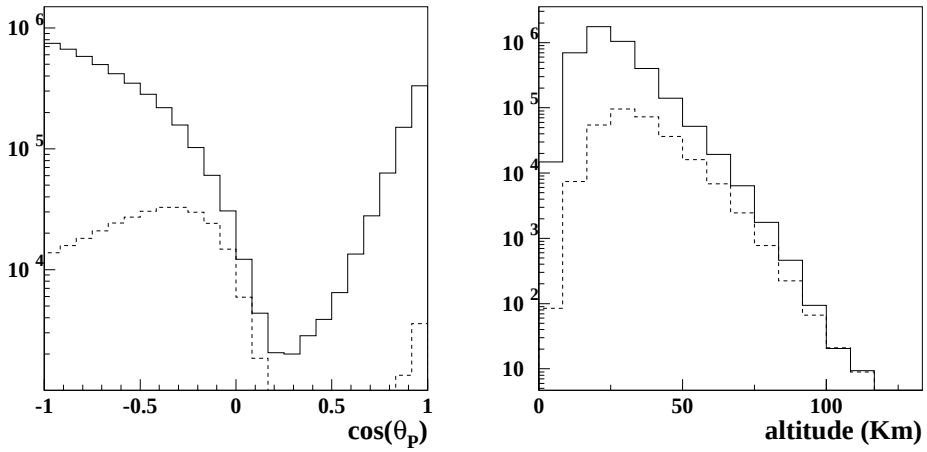

Figure 5.10: Distributions of the altitude (right) and the direction with respect local zenith (left) of the interaction of primary protons with atmosphere. The solid line is relative to the full sample (P_f), the dashed line is representative of the sub-sample generating secondaries detected in AMS (P_e).

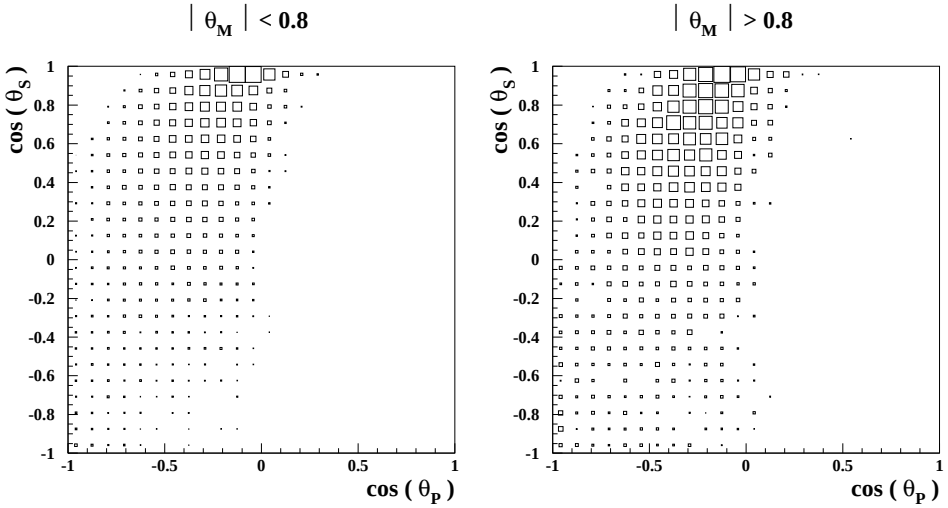

Figure 5.11: Angular distributions of the secondary production at different geomagnetic latitude intervals. On x-axis is represented the cosine of the angle between the primary cosmic ray momentum and the local zenith direction. On y-axis is shown the cosine of the angle between the secondary proton momentum and the primary CR initiating the shower

expected, secondary protons produced at higher altitudes and at large angles with respect to zenith are favored in escaping due to the smaller probability of re-interaction in the residual atmosphere.

Trapped secondary protons are produced preferentially by primary cosmic rays impinging on the atmosphere with a local zenith angle near 90°. These secondary protons have also a similar direction with respect the local zenith. This behavior is shown in figure 5.11, where the two scatter plots present on the x-axis the cosine of the angle between the primary cosmic ray momentum and the local zenith direction, and on the y-axis the cosine of the angle between the secondary proton momentum and the shower axis[5]. Approaching the polar region both angles tend to have a broader distribution, as shown in the right plot in figure 5.11, but the trajectories grazing the atmosphere are still favored. Plots contain only primary cosmic rays belonging to the P_e population.

As already discussed in chapter 3, the contribution of the He primary flux to the production of secondaries is expected to be $\approx 30\%$. This number is the result of the convolution of the fraction of He in the primary cosmic ray flux with the interaction probability for He in a superposition description. We verified this behavior in the results of our simulation. The left plot in figure 5.12 shows the relative contribution of H and He primary fluxes to the secondary proton flux. The He contribution is $\approx 30\%$ only at high latitudes, steadily increasing approaching the equator, where it accounts for $\sim 65\%$ of the secondaries observed in AMS.

The large contribution of He primary flux to the secondary protons in the equatorial bins is a direct consequence of the geomagnetic cutoff. As shown in the rightmost plot of figure 5.12, at a given kinetic energy per nucleon the He nuclei have a greater rigidity with respect H nuclei. Going towards magnetic equator, the geomagnetic cutoff increases and the penumbra region widens. As a consequence the He primary flux contribution is enhanced with respect the one of H primary flux.

The contribution due to the different primary energy bins used in the generation is given in figure 5.13. The left plot is relative to the H primary flux, the right one to the He primary flux. The sum of the contributions in the two plots is normalized to one, contributions smaller than 1% are taken in account but not shown in these plots.

Dominant contributions are coming from the cosmic rays with E_{kn} ranging from few $GeVs$ to few tens of $GeVs$. In the equatorial (polar) regions, where geomagnetic effects are particularly strong (weak), contributions from other energy ranges are becoming important. This aspect is stressed in the two most equatorial bin where 4 different primary energy ranges (counting separately H and He) are contributing each to more than 10% of the flux.

[5]The shower axis coincides with the direction of the primary cosmic ray that initiated the shower.

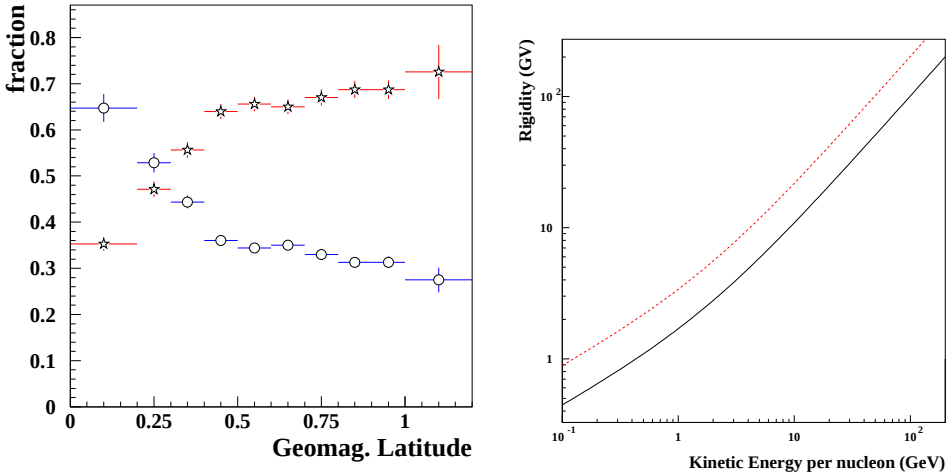

Figure 5.12: Left plot: Relative contribution of He (stars) and H (circles) cosmic fluxes to the production of secondaries observed at different latitudes in AMS. Rightmost plot: Rigidity of H (solid line) and He (dashed line) nuclei as a function of the kinetic energy per nucleon

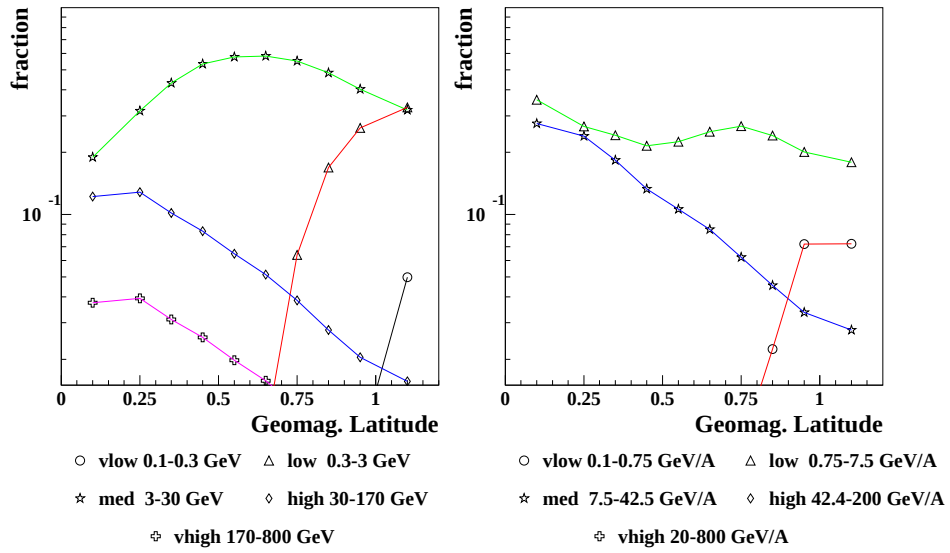

Figure 5.13: Breakdown in energy intervals of the relative contributions of H (left) and He (right) nuclei to the production of secondaries observed at different latitudes in AMS. The normalization is relative to the total flux $H + He$.

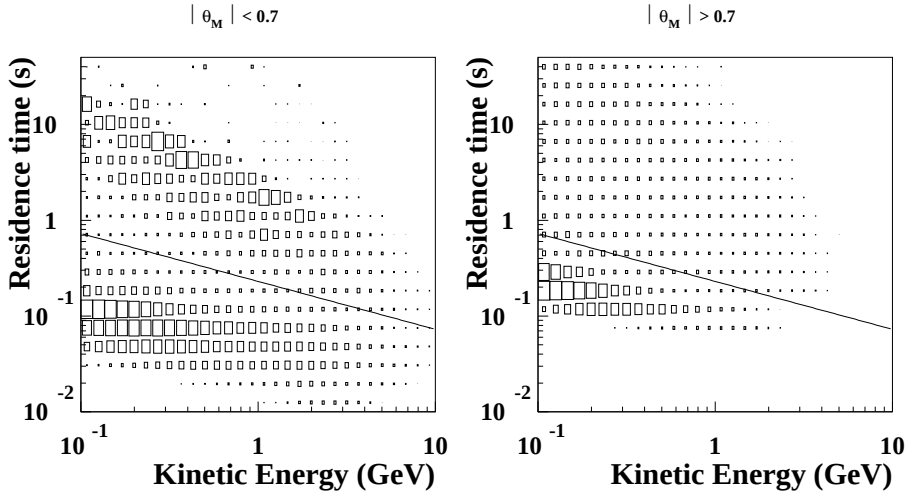

Figure 5.14: Live time as a function of kinetic energy for secondary protons observed in our simulation at low (left) and high (right) magnetic latitudes. See text for a detailed discussion.

Geomagnetic effects on secondaries The dynamical properties of the under-cutoff proton fluxes measured by AMS, briefly reviewed in Chap.4, have raised a wide interest in the scientific community. Qualitative studies and simulations have been performed to describe the so-called *short* and *long* lived populations and their *origin* and *impact* points with the atmosphere.

In particular an original analysis of the AMS data [109] in the framework of the Adiabatic Theory has pointed out the existence of radiation belts underneath the Van Allen belts, filled by *Quasi-Trapped* atmospheric secondaries.

In our simulation, being able to globally reproduce the observed dynamical properties, we can also verify qualitative arguments for their existence and perform detailed comparison with data.

Figure 5.14 shows the relation between the life time and the kinetic energy of the secondary protons revealed at different geomagnetic latitudes in our simulation. In the left distribution - which corresponds to low geomagnetic latitudes - the *short lived* and *long lived* populations can be clearly distinguished. An empirical function $f(E_{kn}) = 0.23/\sqrt{E_{kn}}$ corresponding to the line superimposed on the plots has been used to separate the two populations [109]. No clear structure appears for large values of the protons life time in the right distribution, relative high latitudes.

A different behavior among the populations of the different geomagnetic latitude intervals is also observed when looking at the number of crossing of the AMS detection sphere done by each particle along its trajectory. This

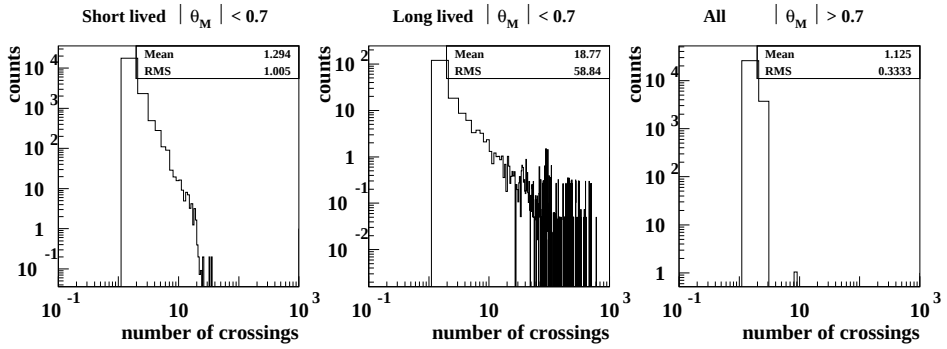

Figure 5.15: Number of crossing of the AMS detection sphere done by (1)*long-lived* and (2)*short-lived* secondary protons detected at $|\theta_M| < 0.7$ and (3)all protons at $|\theta_M| > 0.7$.

is shown in fig. 5.15 where the distribution of the number of crossing is reported separately for *long-lived*, *short-lived* protons at $|\theta_M| < 0.7$ and all protons at $|\theta_M| > 0.7$.

The reason for such differences becomes immediately clear when looking at the typical trajectories of such particles, shown in figs. 5.16, 5.17, 5.18. There, the Z axis is pointing towards magnetic south, X and Y axis are defined in the magnetic equatorial plane. The scale units are Earth radii. The Earth is represented by the internal circle, while the external circumference gives the detector surface of our simulation. In fig. 5.16 the gyration and bouncing motion for typical *short-lived* particles are clearly visible in the vertical projections. The detecting surface is crossed only twice since the reabsorption in atmosphere takes place after two bounces. In fig. 5.17 the gyration, bouncing and drifting components of the motion are clearly visible for a *long-lived* particle in the vertical projection on the rightmost plot. In this case the motion is relatively close to the Earth and the detecting surface is crossed many times before reabsorption. The equatorial projection on the left clearly shows the total drift path, nearly circular and eccentric with respect the Earth as expected from the geomagnetic dipole offset. The origin of the proton is marked with a cross and a continuous westward drift characterizes its motion until reabsorption. In fig. 5.18 no periodicity can be identified in the motion of a proton with relatively long live time detected at $|\theta_M| > 0.7$. The motion is at relatively large distances from the Earth, so that the proton will encounter the detector surface only at the beginning and at the end of its life.

The *short* and *long lived* protons detected at low magnetic latitudes are escaping from atmosphere under kinematical conditions which allow for a periodic motion on magnetic shells. The different time scales in their life outside atmosphere are relative to the geometry of the shells, i.e. to the

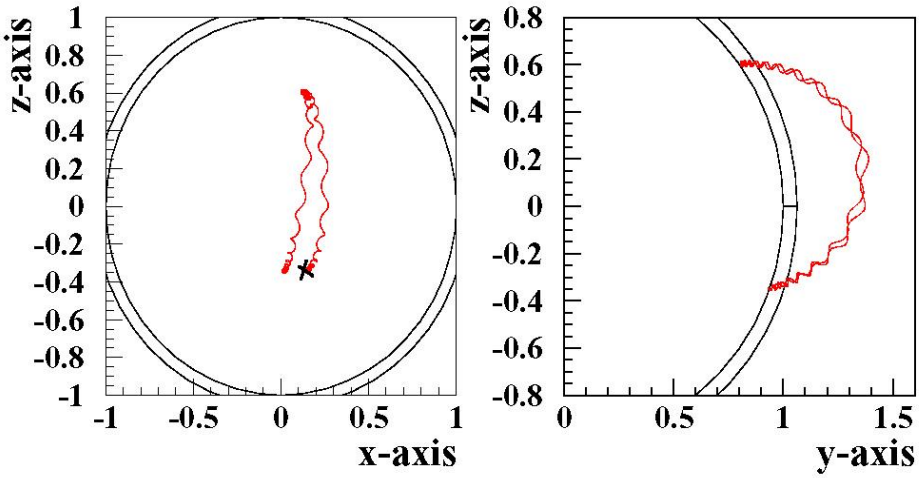

Figure 5.16: Typical trajectory for a *short-lived* proton.

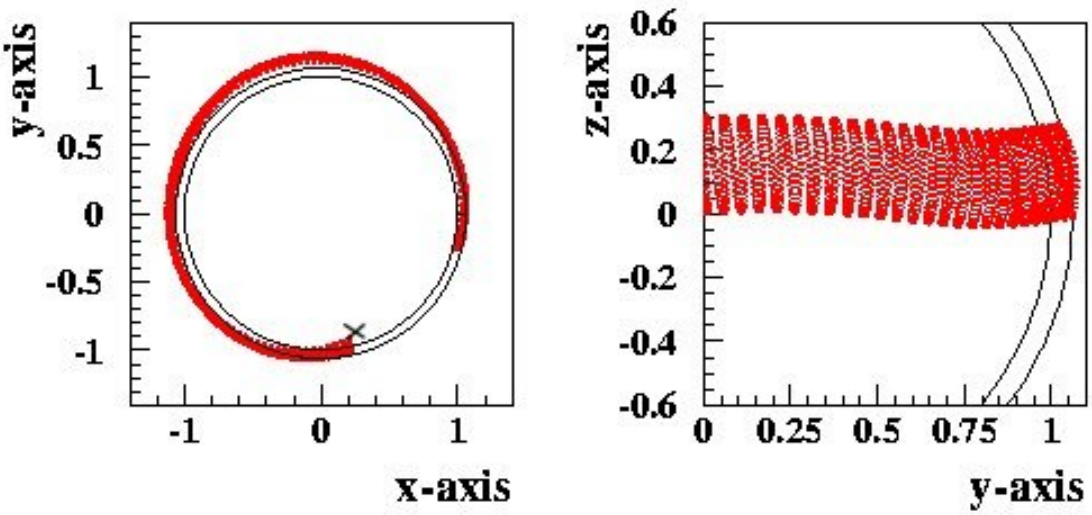

Figure 5.17: Typical trajectory for a *long-lived* proton

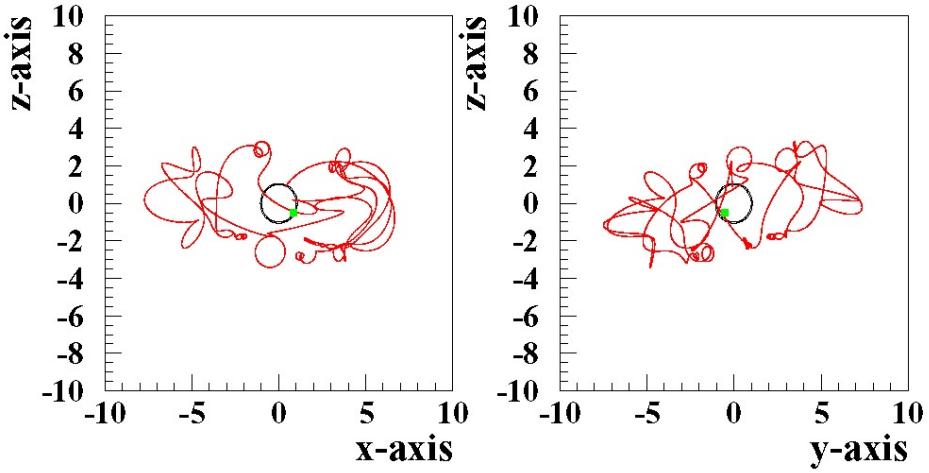

Figure 5.18: Chaotic trajectory for a proton revealed at $|\theta_M| > 0.7$

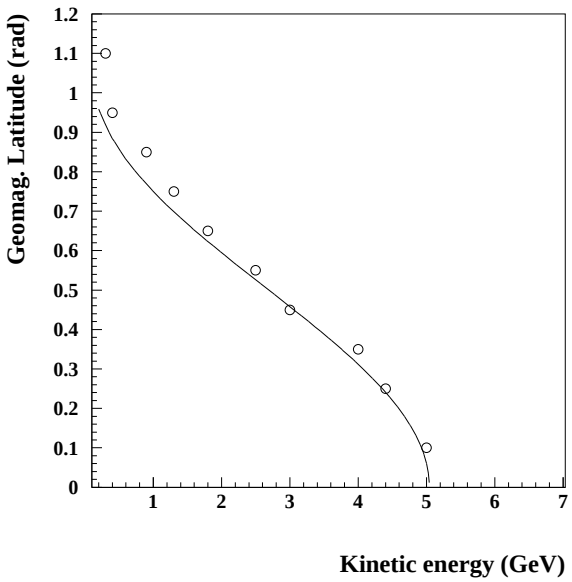

Figure 5.19: Solid line represents at a given geomagnetic latitude the maximum proton energy for which an adiabatic motion can subsist. The empty circles are indicative of the maximum energy at which a significant flux of secondary protons is observed at the different latitudes. See text for a more detailed discussion.

height of their mirror points. For these particles, the use of an adiabatic approach in analyzing their characteristics is fully justified and supported by our simulation. In particular, the *long-lived* component can be simply associated to the *Quasi-Trapped* component defined in [109]. Different kinematical conditions are instead characteristics of protons escaping at high magnetic latitudes. This can be qualitatively seen also in fig. 5.19. There, the solid line represents at a given geomagnetic latitude the maximum proton energy for which an adiabatic motion can exist. This is an indicative curve obtained imposing a maximum value of 0.3 for the smallness parameter (cfr. §2.3.2) calculated using the approximated formula proposed in ref. [131]. Empty circles indicate the maximum energy at which a significant flux of secondary protons is observed in our simulation at the different latitudes. Up to geomagnetic latitudes $|\theta_M| < 0.7$ the energy of the secondary protons is in the region of adiabatic motion. At higher latitudes however, the situation is different and a large part of the secondaries follows complex trajectories.

Good results are obtained when comparing our simulation with AMS data. Left plot of figure 5.20 shows the residence times of secondary protons moving along magnetic shells versus the kinetic energy, to fill this scatter plots we imposed the same cuts used in the data and described in ref. [109],

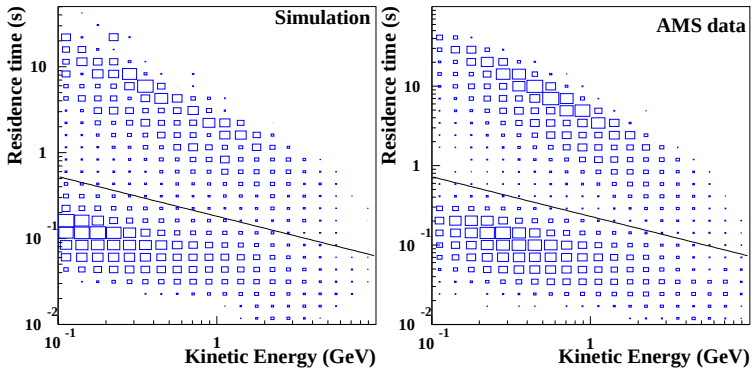

Figure 5.20: Distribution of residence times as a function of kinetic energy obtained in our simulation (left) and in AMS data [109] (right) for secondary protons at $|\theta_M| < 0.7$

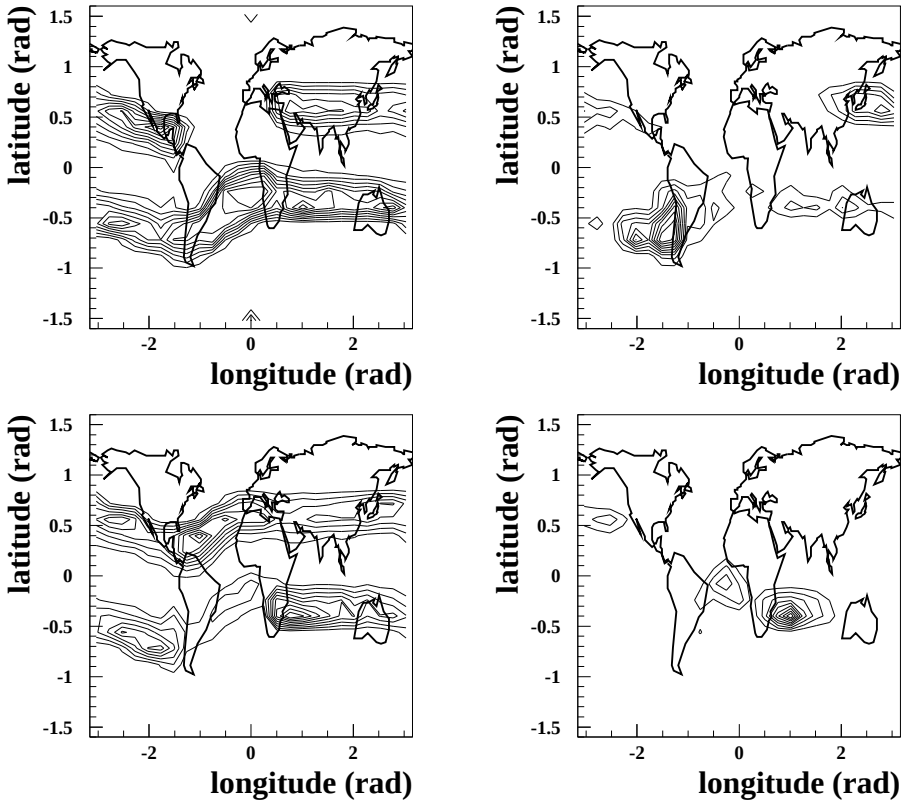

Figure 5.21: Geographical locations of origin (top plots) and reabsorption (bottom plots) in atmosphere of *short-lived* (left plots) and *long-lived* (right plots) protons detected in our simulation at $|\theta_M| < 0.7$.

so some difference is observed with respect fig. 5.14. A good agreement is observed comparing with the distribution obtained from AMS data [109] (fig. 5.20 right plot).

A nice agreement is also found when looking at the geographical maps of the points of origin and reabsorption in the atmosphere for the *short* and *long* lived protons. These are presented in figure 5.21: upper plots refer to the origin points and lower plots to the absorption points of secondaries. Left (right) plots are relative to *short (long) lived* protons detected at $|\theta_M| < 0.7$ in our simulation. The equivalent distributions measured by AMS were presented in §4.3.

The continuous distribution in the location of origin (absorption) points for *short-lived* is symptomatic of the motion of these particles on magnetic shells with most of the mirror points below atmosphere. The distinct spots visible instead for *long-lived* particles are the signature of a motion along magnetic shells intersecting the atmosphere only in regions of weakest B field, as around the SAA.

The successful description of all these dynamical effects in our simulation, allows for a critical discussion on the differences between our detection technique and the AMS measurements. In our simulation all the crossings of the secondaries produced in an event are considered as simultaneous and this allows us to reproduce the AMS measurements with an ETE of the order of picoseconds. This is particulary critical when dealing with the *long-lived* component of the under-cutoff fluxes.

Long lived protons are produced only in a small fraction ($\sim 0.3\%$) of the events but they have a large influence on the under-cutoff fluxes due to their large number of detector crossings. In the most equatorial bin the contribution of the long lived protons to the under cutoff is $\sim 70\%$ (fig. 5.22a) but the real number of particles generating this flux is quite small. This can be better understood looking at the right plot of fig. 5.22. There, full squares represent the simulated flux of protons at $\theta_m < 0.3$ and triangles indicate the flux component due to long lived particles only. The open circles give instead the long lived flux in our detector obtained by counting only once each particle. It is evident how a small number of particles is effectively generating most of the under cutoff flux observed at equatorial geomagnetic latitudes.

Short and long lived components of the under cutoff fluxes are separately calculated, i.e. the flux in a given energy bin at a given latitude will be written as:

$$J = J_s + J_l = \frac{\sum_i n_{si} m_{si}}{\Delta T S \Delta\Omega} + \frac{\sum n_{li} m_{li}}{\Delta T S \Delta\Omega}$$

where n_{si} (n_{li}) is the number of short (long) lived particles contributing with m_{si} (m_{li}) crossings to the flux. The statistical error on J_s and J_l is calculated as:

$$\frac{\sigma_{J_s}}{J_s} = \frac{1}{\sqrt{N_s}} \; ; \; \frac{\sigma_{J_l}}{J_l} = \frac{1}{\sqrt{N_l}}$$

Where $N_s = \sum_i n_{si}$ and $N_l = \sum_i n_{li}$ represent the number of short and long lived particles contributing to the flux. The error on the total flux is then obtained by the quadratic combination of the errors on the single J_s and J_l components.

However, this takes only partially into account the real effect of statistical fluctuations of the rare long lived component ($N_L \ll N_s$). This is particularly evident in the most equatorial bin where ~ 200 long lived particles dominate the simulated flux and a clear deficit can be observed.In our opinion, a much larger sample of primaries would be needed to keep under control the fluctuations of long lived fluxes.

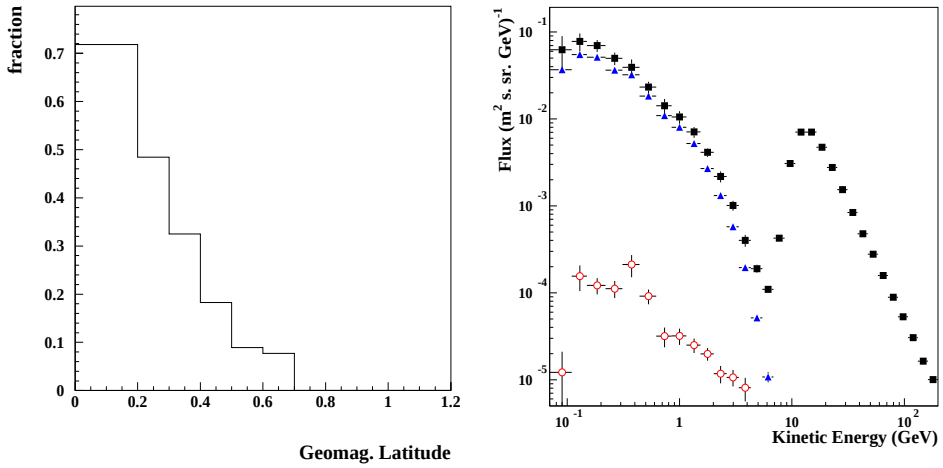

Figure 5.22: Left: Relative contribution of the *long-lived* component to the under-cutoff proton flux as function of the geomagnetic latitude. Right: The long lived protons flux (triangles) compared with the total flux (full squares) and to the long lived flux obtained counting only once each particle (open circles). Plots are relative to the geomagnetic latitude bin $|\theta_M| < 0.2$

5.3 The electron and positron data

Figures 5.23 and 5.24 show the positron and electron fluxes, respectively, measured by AMS (triangles) compared with the results of this simulation (solid lines). The fluxes are corresponding to the zenith attitude of AMS and are subdivided in six intervals of geomagnetic latitude as in [141]. Since cosmic fluxes of $e^{\pm}$ are not included in our simulation, the comparison is relevant only for the under cutoff part of the spectrum.

A good overall agreement is observed for both positrons and electrons at $|\theta_M| < 0.9$. At higher latitudes, the simulated $e^{\pm}$ fluxes are definitely lower than the AMS observations, whereas for protons only a minor deficit was observed. This is justified by the missing contribution of cosmic $e^{\pm}$ fluxes, which are neglected in our simulation, but become relevant at low energies in the most polar bin.

In the following we describe the features of the under cutoff positrons and electrons fluxes, and we discuss the details of the agreement between data and simulation for $|\theta_M| < 0.9$.

5.3.1 The production

As for protons, positrons and electrons that populate the under cutoff part of the spectrum are produced in the interactions of primary cosmic rays with the atmosphere.

Electrons and positrons are mostly coming from the decays of charged and neutral pions. Charged pions contribute, separately to electrons and positrons populations, through the chain:

$$\pi^{\pm} \longrightarrow \mu^{\pm} \longrightarrow e^{\pm} \tag{5.3}$$

while neutral pions are producing the same amount of e^- and e^+ through the chain:

$$\pi^0 \longrightarrow \gamma\,\gamma \longrightarrow 2(e^+ + e^-) \tag{5.4}$$

The relative contributions of charged and neutral pions to the under cutoff flux of e^- and e^+ observed in AMS depend on the combination of two factors: the features of the primary CR interaction (i.e. multiplicity and energy of charged/neutral pions) and the charge dependent transport of the secondaries in the geomagnetic field.

Table 5.2 shows, at four typical energies, the mean multiplicity and the mean energy fraction of protons and pions produced in the interaction of the cosmic rays with the atmosphere. The numbers in the table are relative to our simulation, thus reflect the physics processes implemented in the FLUKA model. The relative abundance of charged and neutral pions is energy dependent: at low energies the production of π^+ is favored as a consequence of the initial charge bias, at higher energies the charge asymmetry tends to vanish and the π^0 contribution becomes the most important. Table 5.3 instead shows the relative contribution of the charged and neutral pions to the e^- and e^+ fluxes detected at 400 Km.

The *ancestors* of e^- and e^+ are produced in the early stages of the shower development: in the 60% of the cases positrons and electrons that are reaching the AMS orbit are coming from pions produced in the primary interaction, another 30% comes from pions produced in the second or in the third interaction, a residual 7.5% is coming from pions produced in interactions

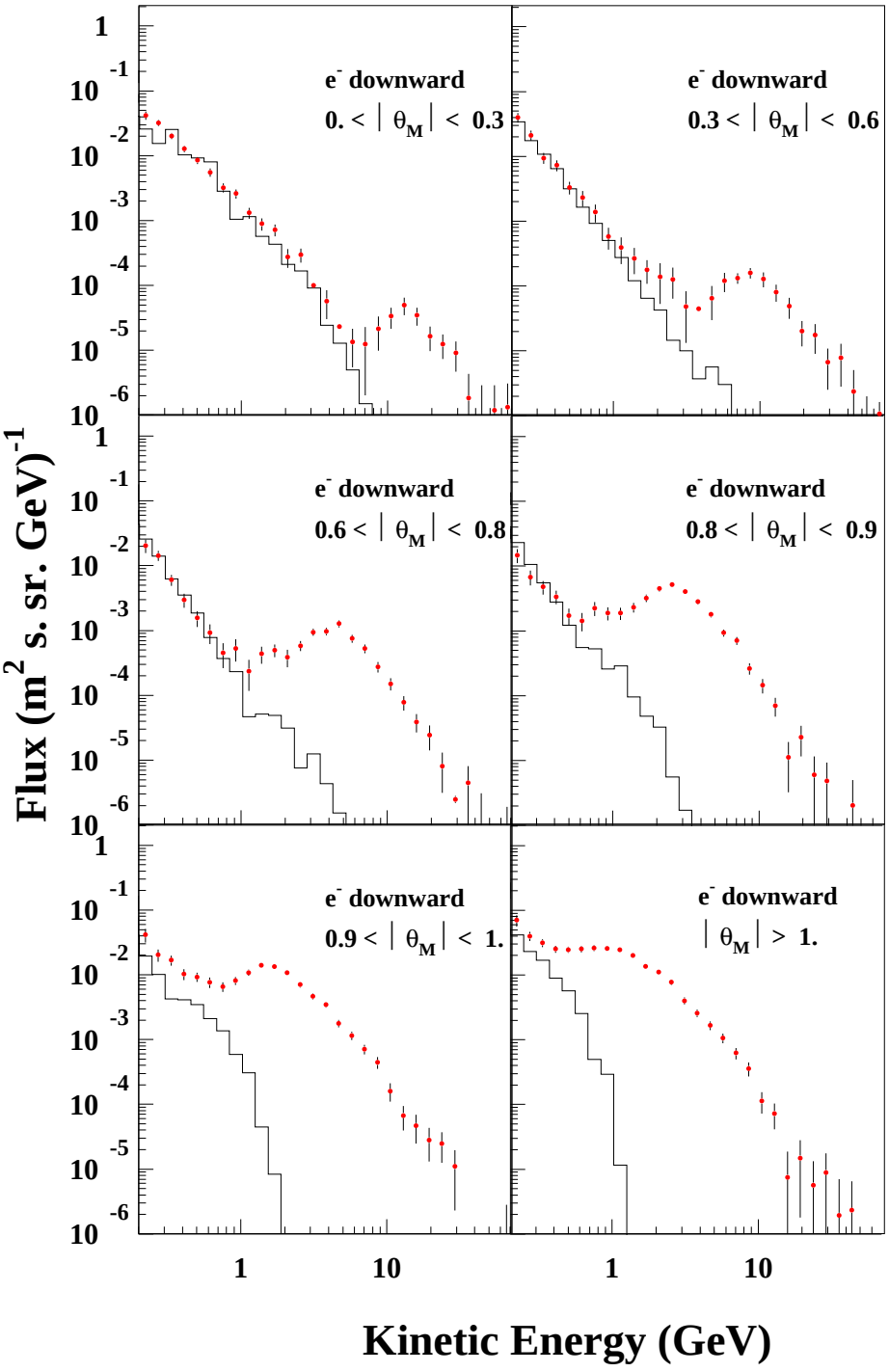

Figure 5.23: Zenith electrons fluxes measured by AMS (red points) compared with the fluxes calculated in this simulation (solid line histogram)

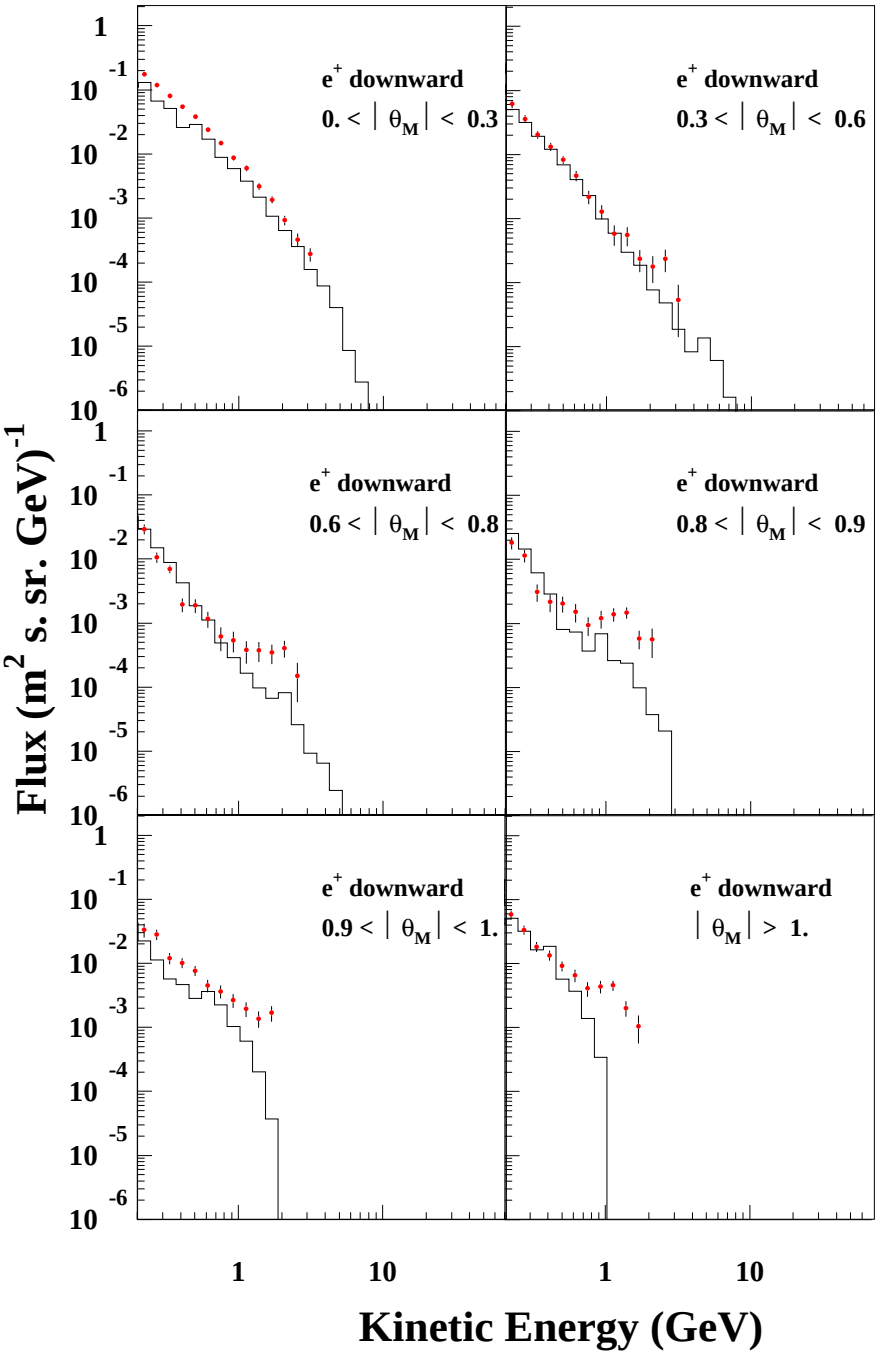

Figure 5.24: Zenith positrons fluxes measured by AMS (red points) compared with the fluxes calculated in this simulation (solid line histogram)

	$5GeV$		$10GeV$		$20GeV$		$30GeV$	
Particle	Mult.	E frac.	Mult.	E frac.	Mult.	E frac.	Mult.	E frac.
p	1.983	0.409	2.676	0.337	2.744	0.307	2.770	0.294
π^+	0.711	0.131	1.292	0.149	1.970	0.159	2.381	0.164
π^-	0.389	0.068	0.975	0.098	1.641	0.116	2.047	0.122
π^0	0.638	0.114	1.601	0.169	2.378	0.175	2.840	0.177

Table 5.2: Energy fraction and multiplicity of secondary particles for the proton interactions with atmospheric nuclei in FLUKA 2000. Four typical energies of primary protons are considered.

	π^+	π^-	π^0	Other
electrons	0.6%	41%	55%	3.4%
positrons	45%	0.4%	52%	2.6%

Table 5.3: Relative contribution of charged and neutral pions to the production of e^- and e^+ observed at 400km as resulting from our simulation

up to the fifth. The missing 2.5% is produced in the conversion of $\gamma - rays$ produced in the first interaction.

Positron and electrons observed at the altitude of 400 Km are then produced mostly as particles of fourth and fifth generation, while under cutoff protons are usually of second or third generation. Appearing later in the development of the shower, electrons and positrons are carrying a smaller fraction of the primary cosmic ray with respect the under cutoff protons. Since the under cutoff spectra considered in this work cover the same energy ranges both for protons and for electrons and positrons[6], it follows that e^- and e^+ observed at 400 Km are produced by primaries with a greater energy with respect to those producing under cutoff protons.

Only 3.4% of the primary cosmic rays reaching the Earth atmosphere produce e^- and e^+ detectable by AMS at 400 Km. These $e^\pm$ are produced in preference by primary cosmic rays grazing the atmosphere, as in the case of the under-cutoff protons. Figure 5.25 shows on the x-axis the cosine of the zenith angle for the primary cosmic ray at the interaction. On the y-axis is reported the cosine of the angle of the secondary electron momentum with respect the shower axis. As was observed for secondary protons, at lower geomagnetic latitudes the distribution is peaked for a primary zenith angle near 90° and for secondary e^- collinear with the primary cosmic ray. A broader distribution is observed at higher latitudes. No significative differences are found in the same distributions for positrons.

[6]AMS positron fluxes are measured in a limited energy interval, however in our simulation we take into account the full e^+ secondary production.

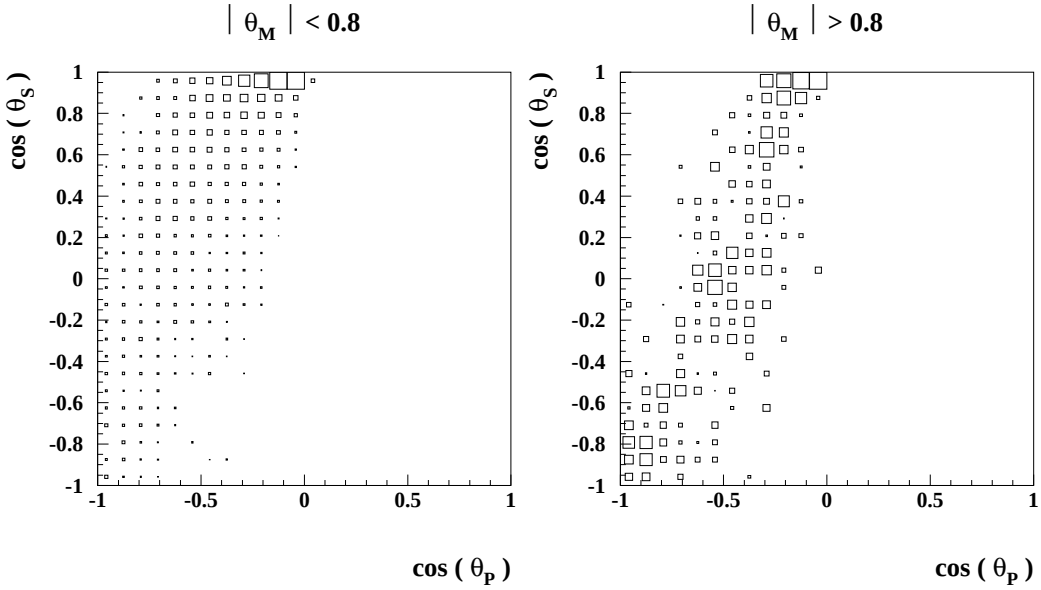

Figure 5.25: Angular distributions in the secondary production of e^- in different geomagnetic latitude intervals. On the x-axis is represented the cosine of the angle between the primary cosmic ray momentum and the local zenith direction. On the y-axis is shown the cosine of the angle between the secondary electron momentum and the primary CR initiating the shower.

More interesting is the distribution of the azimuth angle (as defined in chapter 2) of the primaries at the interaction.

Figure 5.26 shows, as a function of the geomagnetic latitude, the fraction of eastward going primary protons responsible for secondary protons (filled squares), positrons (empty diamonds) and electrons (empty squares) observed in our AMS-like detector. A clear dominance of eastward going protons is observed for the production of positive charged secondaries (protons and positrons) at low geomagnetic latitudes. The effect is reduced with increasing latitudes and tends to vanish in the polar region. The opposite trend is found for the protons producing electrons.

The underlying mechanism for such a behavior is sketched in fig. 5.27: protons grazing the atmosphere going towards East (West) are expected to favor the production of upward moving positrons (electrons) which can therefore escape atmosphere. The opposite is true if the charge sign of secondaries is reversed.

This effect, combined with the East-West asymmetry due to the rigidity cutoff on primaries (cfr. Chap.2), has a relevant influence on the different spectra for e^- and e^+ escaping the atmosphere after generation.

Figure 5.29 shows the relative contribution of the different charge states

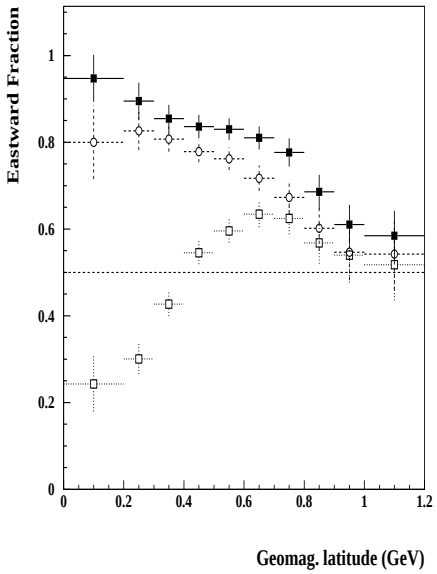

Figure 5.26: Fractions of eastward going primary protons responsible for secondary protons (filled squares), positrons (empty diamonds) and electrons (empty squares) observed in our AMS-like detector, as a function of the geomagnetic latitude.

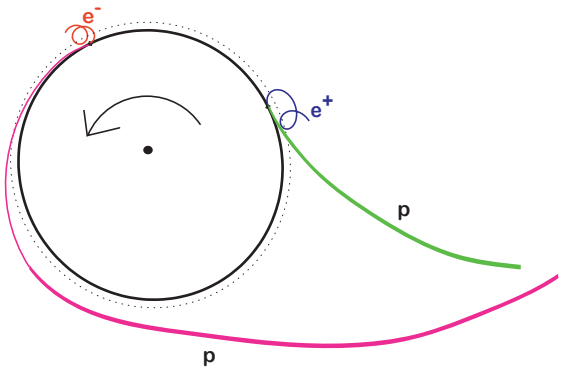

Figure 5.27: The trajectories of protons interacting in the atmosphere are represented in an equatorial projection. The B field lines can be assumed exiting from the plane of the figure in the orthogonal direction. The right proton is moving towards East at the interaction. The resulting positron, approximately emitted along the primary direction, is bent to escape the atmosphere. The left proton is moving towards West at the interaction. The resulting electron is bent to escape the atmosphere.

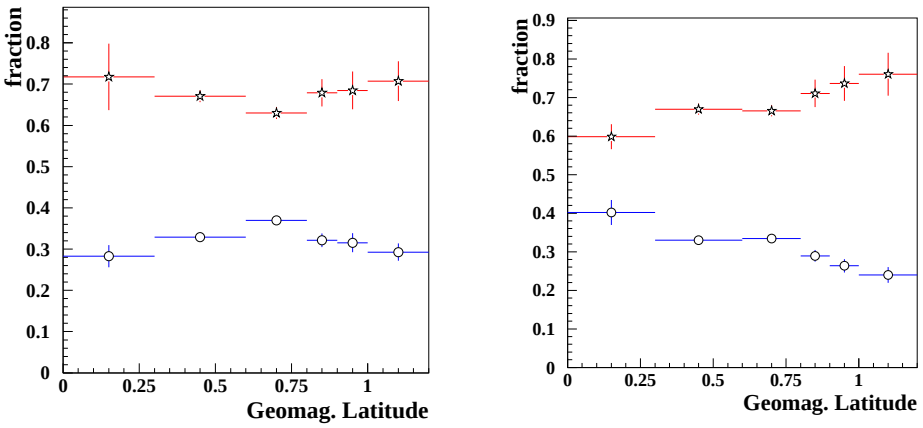

Figure 5.28: Relative contributions of H (stars) and He (empty circles) primary fluxes to the under-cutoff e^- (left) and e^- fluxes (right) as a function of the geomagnetic latitude of detection

of the pions to the production of under-cutoff e^- and e^+ as a function of their detection geomagnetic latitude. The π^0 relative contribution increases both for $e^\pm$ with latitude, representing a $\sim$ 60%(55%) of the $e^{+(-)}$ flux source at $|\theta_M| > 0.5$. This is expected from the generated multiplicities of neutral/charged pions in the proton interactions with the atmosphere (tab. 5.2). The geomagnetic effects discussed above are responsible for the enhancement of the charged pion contribution at low latitude for both e^- and e^+, as well as for the lager enhancement of the charged pions contribution observed for positrons.

Figure 5.28 shows the relative contribution of H and He primary fluxes to the under cutoff components of e^- (left) and e^+ (right) fluxes as a function of geomagnetic latitude. A different behavior is observed for electrons and positrons. In the e^+ flux, the He contribution increases moving from the polar to the equatorial latitudes, where it reaches a maximum at $\sim$ 40%. In the e^- flux, the He contribution is nearly constant at all latitudes, at a value of $\sim$ 30%. For both e^- and e^+ fluxes this distribution differs from what observed for secondary protons (cfr. figure 5.13) where a larger contribution of He was found, especially near equator.

The origin of these differences is strictly related to the different energies of the primaries generating under-cutoff protons, electrons and positrons. As previously discussed, the energy of the primaries originating the $e^\pm$ fluxes observed in AMS are larger than the energies of the primaries responsible for the H fluxes. Therefore, in proximity of the cutoff, the rigidity difference between H and He nuclei at a given kinetic energy per nucleon is not critical for $e^\pm$ production as it was for H. In fact, the kinetic energies of the primaries are anyhow larger for the observed $e^\pm$.

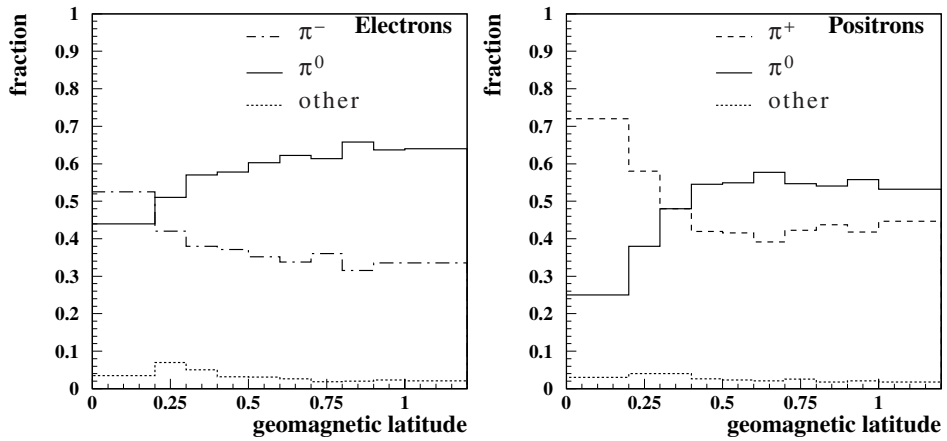

Figure 5.29: Simulation of the relative contributions of charged and neutral pions to the e^- (left) and e^+ (right) fluxes as a function of their detection latitude.

The effect is effectively washed out in the e^- fluxes due to the different kinematics of the e^- escape from atmosphere (cfr. figs. 5.27, 5.26) which naturally selects primaries with large energy.

The contribution of primary H and He for the different energy intervals to the electrons and positron production is presented in the figures 5.30 and 5.31, respectively, as a function of the geomagnetic latitude. Geomagnetic effects are modulating the relative importance of the contributions. As expected, the higher energy components are dominating the electron fluxes at equatorial latitudes.

5.3.2 Geomagnetic effects

The live time of the secondary positrons and electrons has been studied to compare with AMS measurements and to investigate the dynamical features of the under cutoff spectra. Electrons and positrons have in this aspect a behavior very similar to the one observed for secondary protons. Figure 5.32 shows, for two ranges of geomagnetic latitudes, the correlation between the kinetic energy and live time of under cutoff electrons and positrons. The structure is very similar to the one observed for protons (fig. 5.20) and the same distinction in long and short lived populations naturally arises.

Figures 5.33 shows the fractional contribution of long lived e^- and e^+ to the under cutoff fluxes separately for electrons and positrons. The long lived component is prevalent in the most equatorial bin, and rapidly decreases going towards higher latitudes. No significant differences are observed between e^- and e^+ . The same estimation of the statistical error used for the protons has been used also for e^- and e^+ .

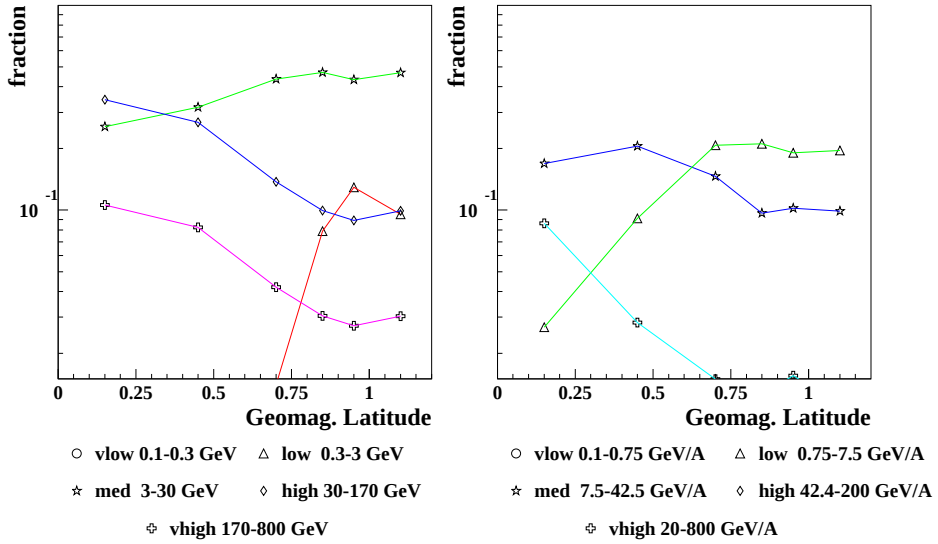

Figure 5.30: Relative contributions of H (left) and He (right) nuclei to the production of secondary electrons observed at different latitudes in AMS (simulation).

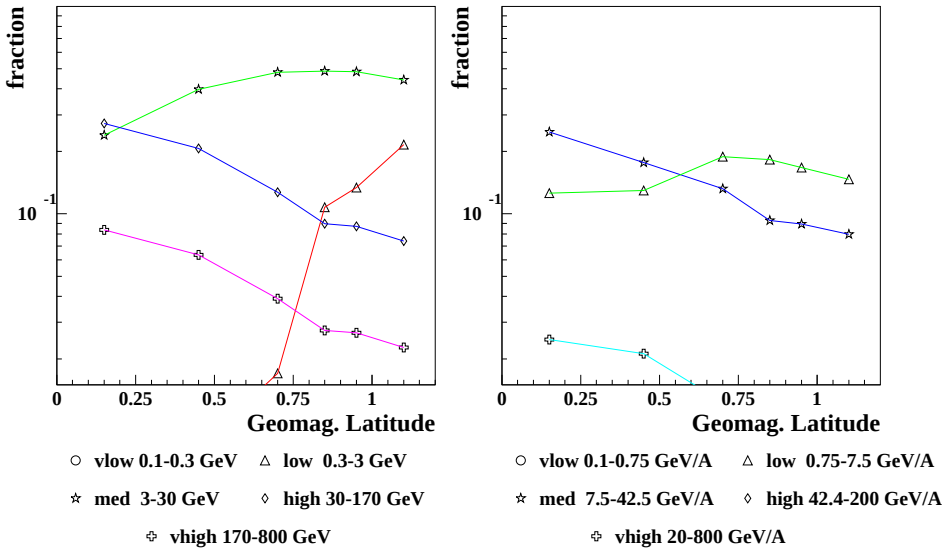

Figure 5.31: Relative contributions of H (left) and He (right) nuclei to the production of secondary positrons observed at different latitudes in AMS. (simulation)

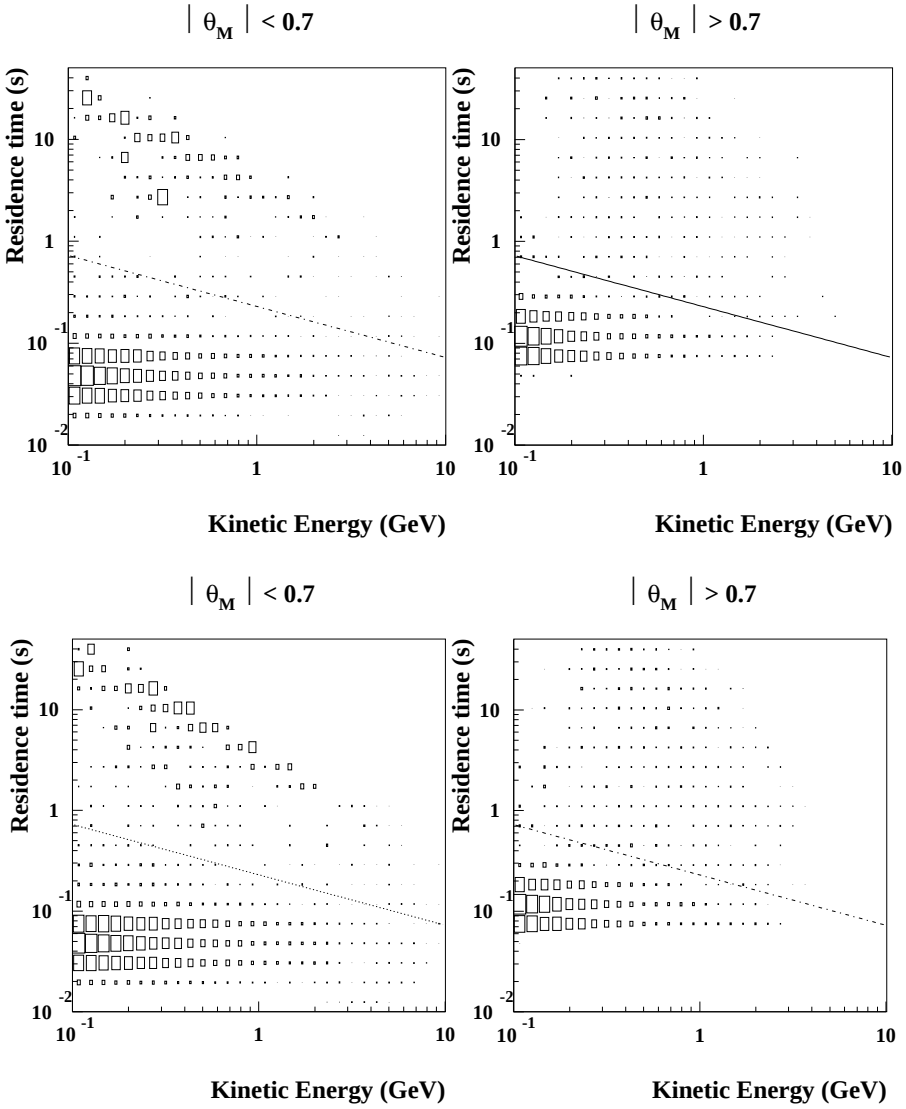

Figure 5.32: Live time as a function of kinetic energy for secondary electrons (upper plots) and positrons (lower plots) observed in our simulation at low (left plots) and high (right plots) magnetic latitudes. See text for a detailed discussion.

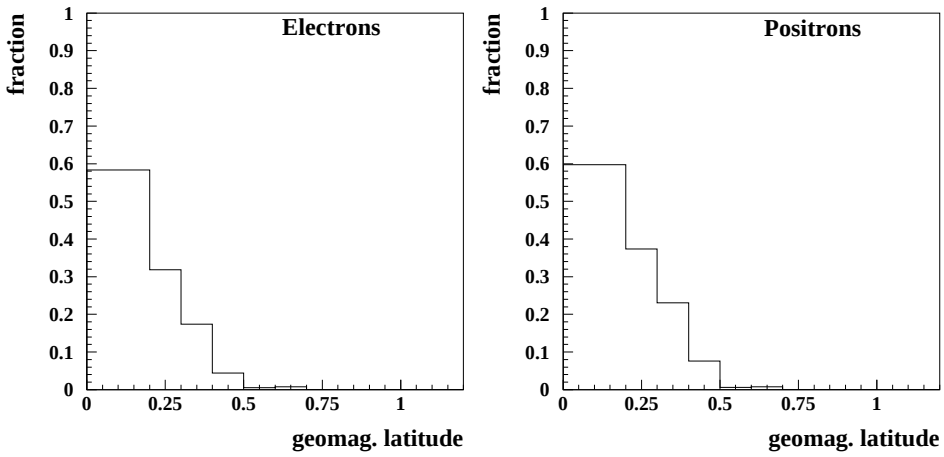

Figure 5.33: On the left (right) the fraction of the under cutoff electron (positron) flux generated by long lived particle.

The origin and the absorption regions of e^- and e^+ have been studied separately for the two populations. In figure 5.35 (5.34) the geographical maps of origin and absorption for short and long lived electrons (positrons) are shown.

These maps show that short lived e^- and e^+ move on shells whose mirror points are inside the atmosphere, while long-lived e^- and e^+ move on shells intersecting the atmosphere only above the SAA and the other zones of weakest geomagnetic field. Furthermore long lived particles origin and absorption zones are consistent with electrons (positrons) drifting eastward (westward) around the Earth.

5.3.3 Comparison with AMS

The two upper panels of figure 5.36, show the integrated under cutoff fluxes of positrons and leptons as function of the geomagnetic latitude. Open squares represent this simulation while black stars are the AMS data. The two low panels are presenting the ratios, simulation over data, of the plots shown in the upper panels. Black lines delimitate the $\pm 20\%$ interval around unity.

At high latitudes, we observe the deficit due to the neglected contribution from primary $e^\pm$ already discussed in §5.1. At intermediate latitudes ($0.3 < |\theta_M| < 0.8$) the agreement between our simulation and AMS data is at the level of $\pm 20\%$, consistent with the expected uncertainties. In the most equatorial bin a severe discrepancy is observed. The simulated $e^-(e^+)$ flux represents only a $\sim 75(60)\%$ of the AMS measurement. The origin of this deficit has been identified, as in the proton case, in the dominance of long

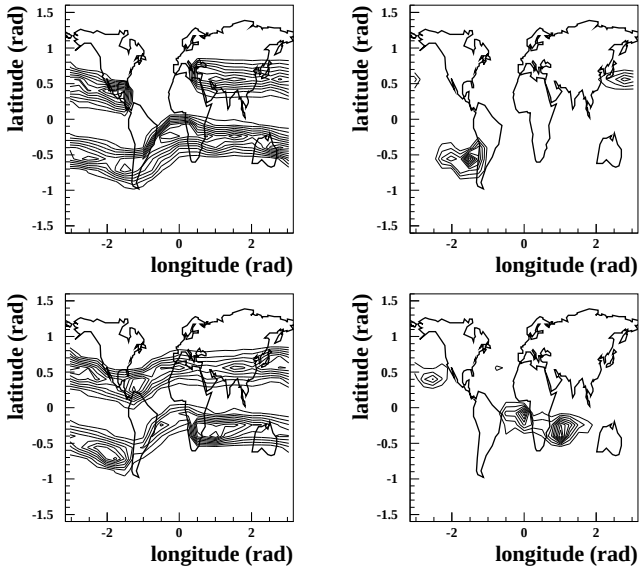

Figure 5.34: Geographical locations of origin (top plots) and reabsorption (bottom plots) in the atmosphere of *short-lived* (left plots) and *long-lived* (right plots) electrons detected in our simulation at $|\theta_M| < 0.7$.

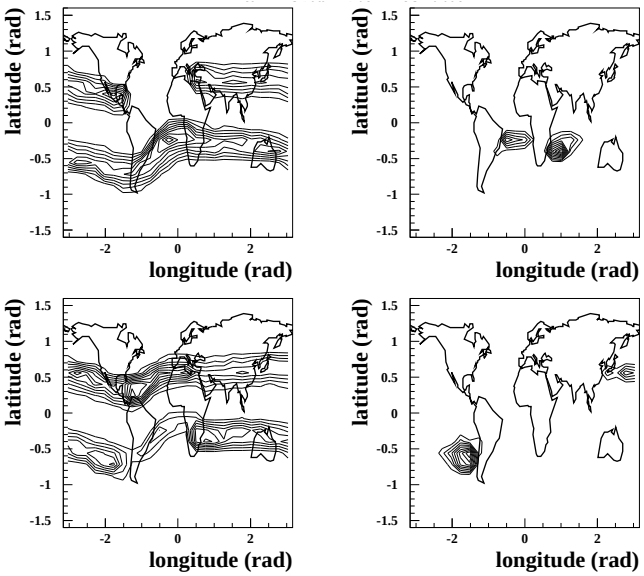

Figure 5.35: Geographical locations of origin (top plots) and reabsorption (bottom plots) in the atmosphere of *short-lived* (left plots) and *long-lived* (right plots) positrons detected in our simulation at $|\theta_M| < 0.7$.

lived particles, which account for $\sim 60\%$ of both e^+ and e^- under cutoff fluxes.

Figure 5.37 shows the ratio of under-cutoff positron and electron fluxes as a function of geomagnetic latitude measured by AMS (black squares) and in our simulation (open circles). The peculiar dependence of this ratio with the geomagnetic latitude and in particular the net positron dominance at $|\theta_M| < 0.5$ are well reproduced in our simulation. It is clear from our simulation that this behavior is mostly due to geomagnetic effects, and cannot be attributed to charge asymmetry at production (tab. 5.2 and 5.3). The positron dominance near equator is due to the lower geomagnetic cutoff experienced by Eastward going primaries, which are preferably injecting positrons at the AMS altitude. The positron dominance tends to vanish going towards magnetic poles, as the East-West asymmetry effect reduces.

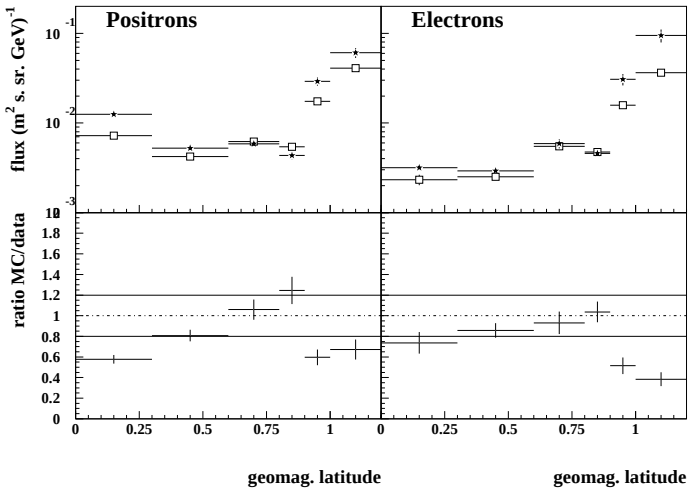

Figure 5.36: Upper two panels are presenting the integrated fluxes of under cutoff electrons (left) and positrons (right) as function of the geomagnetic latitude, for both AMS data (black points) and this simulation (open squares). Lower two panels are showing the ratio Monte Carlo over data of the corresponding upper panels, the two horizontal lines are at $\pm 20\%$.

5.4 Summary

The detailed comparison of our simulation results with the AMS measurements of proton and $e^{\pm}$ fluxes verified under many different aspects our model of cosmic ray interactions with the near earth environment.

The generation procedure and the absolute normalization of our Monte Carlo flux have been validated against the measurements of primary H spec-

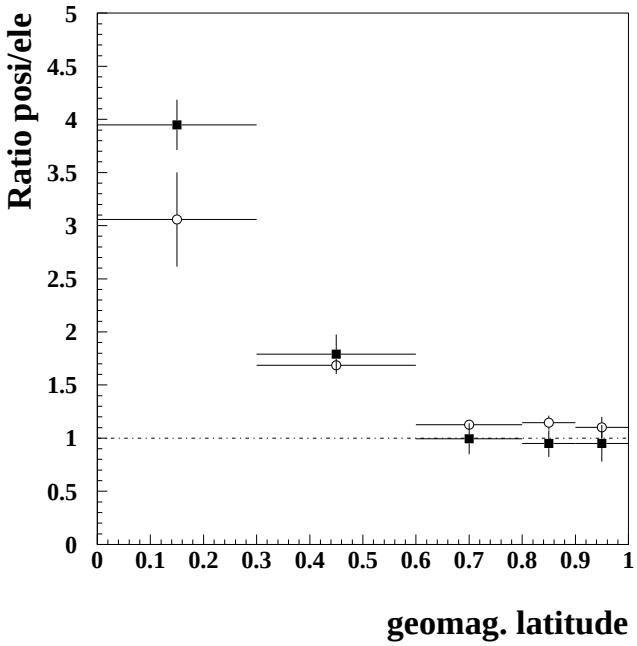

Figure 5.37: ratio of under cutoff positrons flux and under cutoff electrons flux as function of the geomagnetic latitude, for both AMS data (black squares) and this simulation (open circles)

trum.

The latitude dependence of the geomagnetic cutoff on primary fluxes has been correctly reproduced, with a reduced agreement only in the penumbra region due to the limited statistics and the approximations in the transport of He in atmosphere.

The accuracy of the interaction model and the precision of the tracing in the geomagnetic field are both confirmed by the results obtained in the simulation of the under-cutoff fluxes. In most cases, our simulation reproduces within a $\pm 20\%$ the under cutoff proton and lepton fluxes measured by AMS, as well as the relative charge abundances in lepton fluxes. The agreement is worsened at the level of $\pm 40\%$ only in a few circumstances, as consequence of peculiar dynamical conditions. These correspond to regions where most of the flux is determined by a small number of secondaries characterized by a long residence time. This is in effect the only point of our generation where the equivalent exposure time of few picoseconds revealed to be insufficient to cope with the rarity of the long lived particle production rate.

Nevertheless, the main dynamical features of under cutoff particles, with both short and long residence times, found in our simulation are in optimum agreement with the results obtained by back tracing methods applied to AMS data. In particular, the location of production and absorption points

obtained for short and long lived secondaries are those expected for particles moving along the open drift shells intercepted by AMS.

Reanalyzing the AMS data in terms of the adiabatic invariant formalism, i.e. in terms of fluxes in the (L, α_0) parameter space, as done in [109], our results gain a more general meaning. This simulation is able to reproduce the fluxes of under cutoff particles along the magnetic drift shells intercepted by AMS out of the SAA. Since, as shown in [109], this set of shells represents a significative portion of the (L, α_0) parameters space corresponding to the near Earth region, we are confident that our simulation is able to well reproduce the near Earth fluxes of protons and $e^{\pm}$, with kinetic energy above $0.1\,GeV$.

Furthermore, looking at the same result from another point of view, we can conclude that the dominant source of under cutoff particles in the Low Earth Orbit (out of the SAA region) is the interaction of the primary cosmic rays with the Earth's atmosphere, since it is the sole injection process implemented in our simulation.

This Monte Carlo simulation is then a good tool to study the near Earth high energy radiation environment, and will be used to investigate the background sources for the experiments operating in Low Earth Orbit.

Conclusions

The simulation of the radiation environment produced in the near Earth region by the interactions of primary cosmic rays with the Earth atmosphere is a difficult task. All the aspects of the simulation are closely related and only an accurate tuning of all the components allows to get reliable results.

The injection of under cutoff particles to bounded trajectories around the Earth, is depending on the angle between their momentum and the geomagnetic field at the moment of their production. For this reason the choice to use FLUKA 2000 that provides a full tridimensional description of the interactions, revealed of fundamental importance.

As drawback, such a description of the interactions is particulary demanding in terms of computing power and only the optimization of the particle tracing and the use of the backtracing method in the primary flux generation has allowed to collect the high statistic needed for this work.

This work would had been of scarce utility without the possibility to compare the results of the simulation with a data set like the one collected by AMS. The high statistics of the AMS data, its accurate determination of cosmic rays composition and the wide latitude coverage over a full range of longitudes, has allowed to test extensively our simulation.

The comparison with AMS data has been a success, our simulation was able to reproduce the detailed dynamical features of protons, electrons and positrons fluxes. Furthermore we had the possibility to investigate the mechanisms at the base of the production and of the injection of the under cutoff particles that are composing the high energy radiation in the near Earth environment. The good agreement with AMS data is also demonstrating that, at least outside the SAA region, the sole source of the radiation environment in the near Earth region is the interaction of the primary cosmic rays with the atmosphere.

This simulation, is then a good tool to study describe the high energy radiation environment on which future experiments will operate in low Earth orbit (LEO).

This simulation can also be used to study the particle fluxes produced in the atmosphere by the primary cosmic rays impinging on it. In particular can be used to investigate the detailed geomagnetic effects on the atmospheric neutrino fluxes predictions.

Acknowledgements

First of all I want to express gratitude to my advisor prof. Roberto Battiston, who gave me the possibility to work in these last three years in the AMS-Perugia group and that encouraged me to start this thesis work.

I want to thank sincerely Dr. Bruna Bertucci, who also participated to the development of this simulation, for her constant interest, her patience and the continuous encouragement she gave me.

I would like to thank Dr. G. Battistoni and Dr. A. Ferrari for the providing of one of the fundamental building block of this simulation the FLUKA 2000 code, and for the willingness they always shown in discussing the development of this simulation.

I wish to thank Dr. E. Fiandrini and Dr. G. Esposito, my colleagues in this PhD adventure, for the useful discussion we had and for the kindness and the friendship during these three years we shared the same office.

I would also to thank Dr. B. Alpat, Dr. G. Ambrosi, Dr. W. J. Burger, and all the other members of the AMS-Perugia group.

Finally I want to thank my family for the constant comfort they gave to me and Stefania for her love, for her patience and for the beautiful moments we shared in the last two years.

Bibliography

[1] V. F. Hess, Phys. Z. **13**(1912) 1084

[2] W. Kohlhörster, Phys. Z. **14**(1913) 1153

[3] W. Bothe and W. Kohlhörster, Phys. Z. **56** (1929) 571

[4] M. Schien et al., Phis. Rev. **59**(1941) 615

[5] P. Freier, Phis. Rev. **74**(1948) 213

[6] K. R. Pyle et al., Astrophys. J. **282**(1984) L107

[7] H. Debrunner et al., Geopyhs. Res. **93** (1988) 7206; J. Steinacker et al., Astron. Astrophys. **224**(1989) 259

[8] M. Takeda et al., Phis. Rev. Lett. **81** (1998) 1163

[9] D. J. Bird et al., Proc. of 24th ICRC Rome 1995, vol. 2 504

[10] L. J. Gleeson and W. I. Axford, Astroph. J. Lett. **149** (1967) 115

[11] M. Nagano and A. A. Watson, Rev. of Mod. Phys. **72** (2000) 689

[12] M. S. Longair, *High Energy Astrophysics*, vol. 1, University Press, Cambridge 1994

[13] T. Abu-Zayyad et al., Astrophys. J. **557** (2001) 686

[14] B. Wiebel-Sooth et al., A. &A. **330** (1998) 389

[15] D. Muller et al., Ap J **374** (1991) 356

[16] J. J. Engelmann et al., Astron. Astrophys. **233** (1990) 233

[17] D. J. Bird et al., Astrophys. J. **511** (1999) 739

[18] N. Hashida et al., Astropart. Phys. **10** (1999) 303

[19] J. A. Bellido et al., Astropart. Phys. **15** (2001) 167

[20] P. Sommers, Proc. of 27th ICRC, Aug. 2001, Hamburg Germany, Rapp. papers, p. 170.

[21] O. Adriani et al., NIM **A478** (2002) 114

[22] A. Letessier-Sevlon, astro-ph/0006111

[23] R. Battiston, *II International Workshop on Matter, Antimatter, Darkmatter*, Int. J. Mod. Phys. 17 (2002) 1589

[24] M. Ichimura et al., Phys. Rev. **D48** (1993) 1949.

[25] M. J. Ryan, J. F. Ormes & V. K. Balasubrahmanyan, Phys. Rev. Lett. 28 (1972) 985

[26] H. Reevs, Rev. Mod. Phys. **66** (1994) 193

[27] M. M. Shapiro, ASP conf No. 171; Eds R. Ramaty et al., (1999) 139-145

[28] J. H. Schmidt, B. M. Haisch, J. J. Drake, Science **265** (1994) 1420

[29] J. J. Drake, Science **267** (1995) 1470

[30] H. O. Kalges et al., Nucl. Phys. B Proc. Suppl. **52B** (1997) 92

[31] M. Aglietta et al., Astrop. Phys. **10** (1999) 1

[32] F. Arqueros et al., A&A **118** (1983) 223

[33] K. Boothby et al., Ap. J. Lett. 491 (1997) L35

[34] J. W. Fowler et al., Astrop. Phys. **15** (2001) 49

[35] B. N. Afanasiev et al., Proc. of the International Symposium on EHCR, M. Nagano editor, 1996 ICRR Tokio, p. 32.

[36] C. J. Bell et al., J. Phys A **7** (1973) 990

[37] A. Borione et al., Nucl. Inst. Meth. **A346** (1994) 329

[38] R. M. Baltrusaitis et al., Phys. Rev. D **31** (985) 2192

[39] J. Linsley, Phys. Rev. Lett. **10** (1963) 146

[40] L. Scarsi et al., Proc. of 27 ICRC, 2001 Hamburg Germany, HE1. 8, p. 839

[41] J. F. Krizmanic et al., Proc. of 27 ICRC, 2001 Hamburg Germany, HE1. 8, p. 861

[42] The Auger Collaboration, Proc. of 27 ICRC, 2001 Hamburg Germany, HE1. 8, p. 699, p. 765

[43] J. -P. Meyer, L. O'C Drury, D. C. Ellison, Astrophys. J. **487** (1997) 182

[44] K. H. Kampert, Proc. of 30th ISMD, Lake Balaton Hungary, Oct. 2000, astro-ph/0102266

[45] Sakaki et al., Proc. of 27th ICRC, 2001 Hamburg Germany, HE1. 04, p. 345.

[46] R. Ramaty et al., Astrophys. J. **488** (1997) 730

[47] R. Plaga, **astro-ph**/0111555

[48] K. Greisen, Phys. Rev. Lett. **16**(1966) 748

[49] G. T. Zatsepin, V. A. Kuzmin, Pis'ma Zh. Eksp. Teor. Fiz. **4**(1966) 114 [JETP. Lett. **4** (1966) 78]

[50] G. A. Medina Tanco, Astrophys. J. Lett. **510** (1999) L91

[51] M. Blanton, P. Blasi, A. V. Olinto, Astropart. Phys. **15** (2001) 275

[52] B. Wiebel-Sooth et al., Lanodolt-Bornstein **vol VI/3c**, Springer Verlag (1999) 37

[53] B. Peters, Nuovo Cimento **XXII** (1961) 800

[54] E. Waxmann in "Physics and Astrophysics of Ultra-High-Energy Cosmic Rays", Lecture Notes in Physics vol. 576 Springer-Verlag, Berlin 2002

[55] G. Sigl et al., Phys. Rep. **327** (2000) 109 and references within.

[56] A. Barrau, Astropart. Phys. **12** (2000) 269

[57] A. A. Watson, Proc. of 25th ICRC, Durban **8** (1998) 257

[58] G. Burbidge, Phys. Rev. **101** (1995) 906

[59] P. Lagage et C. Cesarsky, A&A **118** (1983) 223

[60] H. J. Volk et P. L. Biermann, Ap. J. **229** (1988) L65

[61] R. Silberberg et al., Ap. J. **363** (1990) 265

[62] G. Morfill et al., Ap. J. **312** (1987) 170

[63] A. P. Szabo et al., Phis. Rev. Lett. **69** (1992) 2885

[64] R. Plaga, A&A **349** (1999) 259

[65] M. Hillas, Nature **395** (1998) 15

[66] I. S. Shklowski, Dokl. Akad. Nauk. SSSR **91** (1953) 475

[67] W. H. Ip and W. I. Axford, Proc. of Internat. Symp. on Astroph. aspects of Most. Ene. CR, World Scientific, Singapore 1991, p. 273

[68] K. -H. Kampert et al., **astro-ph**/0102266

[69] D. J. Bird et al., Astroph. J. **441** (1995) 144

[70] T. Maeno et al., Astropart. Phys. **16** (2001) 121

[71] AMS Collaboration, J. Alcaraz et al., Phys. Lett. **B461** (1999) 387

[72] E. Fermi, Astroph. J. **119** (1954) 1

[73] V. S. Berezinsky et al., Astrophysics of Cosmic Rays, North-Holland, Amsterdam 1990.

[74] D. Maurin et al., Ap. J. **555** (2001) 585

[75] R. Aloisio et al., Phys. Rev. **D62** (2000) 530

[76] R. R. Daniel, S. A. Stephens, Space Science Review **17** (1975) 45

[77] V. L. Ginzburg, S. I. Syrovatskii, New York Gordon and Breach (1969)

[78] A. Tilgner, F. Busse and E. Grote, Sterne und Weltraum **4** (2000) 230

[79] M. Walt, Introduction to geomagnetically trapped radiaton. (Springer-Verlag, 1970) .

[80] G. Gustafson et al., J. Atmos. Terr. Phys. **54** (1992) 1609

[81] A. H. Compton, Phys. Rev. **43** (1933) 387

[82] V. D. Il'in et al., Kosmicheskie Issledovaniya **24** (1984) 88

[83] SPENVIS online tool, *http://spenvis. oma. be/*, BIRA-IASB, Belgium 2001.

[84] J. G. Roeder, *Dynamcs of Geomagnetically trapped radiation*, Springer Verlag, 1970

[85] D. J. Cooke et al., Nuovo Cimento **14** (1991) 213

[86] M. Shulz and al., *Particle diffusion in the radiation belts*, Springer, New York, 1974.

[87] D. A. Hamlin et al., J. Geophys. Res. **66** (1966) 1

[88] H. Hilton, J. Geophys. Res. **28** (1971) 6952

[89] T. K. Gaisser and al., Proceedings of the 27th ICRC, Hamburg(germany) (2001), 1643

[90] W. R. Webber, Golden RL, Stephens SA. Proc. 20th Int. Cosmic Ray Conf. 1:325 (1987)

[91] M. S. Vallarta, Phys. Rev. **47** (1935) 747

[92] E. -S. Seo et al. Astrophys. J. 378 (1991) 763

[93] P. Pappini et al. Proc. 23rd Int. Cosmic Ray Conf. 1:579 (1993)

[94] R. Bellotti et al. Phys. Rev. **D60** (1999) 052002

[95] M. Boezio et al. Astrophys. J. **518** (1999) 457

[96] W. Menn et al. Astrophys. J. 533 (2000) 281

[97] T. Sanuki et al. Astrophys. J. 545 (2000) 1135

[98] J. Alcarez et al. Phys. Lett. B490 (2000) 27

[99] J. P. Wefel et al., Proc. of th 27th ICRC, Hamburg(Germany) (2001), OG1. 05, p. 2111

[100] J. T. Link et al., Proc. of th 27th ICRC, Hamburg(Germany) (2001), OG1. 05, p. 2143

[101] F. H. Gahbauer et al., Proc. of th 26th ICRC, Salt Lake City(USA) (1999), OG4. 1. 07

[102] S. J. Stochaj, Proc. of th 27th ICRC, Hamburg(Germany) (2001), Rapp. Papers p. 136

[103] K. Asakamori et al. *Ap. J.* 502 (1998) 278

[104] Ivanenko IP, et al. *Proc. 23rd Int. Cosmic Ray Conf.* 2:17 (1993)

[105] A. V. Apanasenko et al. *Astropart. Phys.* **16** (2001) 13

[106] Y. Kawamura et al. *Phys. Rev.* **D40** (1989) 729

[107] V. Plyaskin, Phys. Lett. **B516** (2001) 213

[108] L. Derome et al., Phys. Lett. **B489** (2000) 1; L. Derome et al., Phys. Lett. **B515** (2001) 1

[109] G. Esposito, *Study of cosmic ray fluxes on low Earth orbit observed with the AMS experiment*, Phd. Thesis, Perugia 2002

[110] G. Fiorentini, A. Naumov and F. L. Villante, Phys. Lett B **510** (2001) 173

[111] F. James, RANLUX Computer Phys. Comm. **79** (1994) 111

[112] F. James, Cernlib documentation.

[113] K. Labitzke, J. J. Barnett, and B. Edwards (eds.) , Handbook MAP 16, SCOSTEP, University of Illinois, Urbana, 1985.

[114] A. E. Hedin, MSIS-86 Thermospheric Model, J. Geophys. Res. **92** (1987) 4649

[115] N. A. Tsyganenko, J. Geophys. Res. **100** (1995) 5599

[116] C. E. Barton, Revision of IGRF, 1996 Americal Geophysics Union http://www. agu. org

[117] F. J. Lowes, Earth Planets Space **52** (2000) 1207

[118] T. K. Gaisser, Proc. of TAUP 2001, Assergi (Italy) (2001) ; R. Engel et al., Proc. of th 27th ICRC, Hamburg (Germany) (2001) , HE2. 02

[119] M. Honda et al., Phys. Rev. D**52** (1995) 4985

[120] A. Fassó et al., Proc. of the MonteCarlo 2000 Conference, Lisbona (Portugal) , October 2000. A. Kling et al. eds., Springer-Verlag Berlin, (2001) 955-960,.

[121] A. Ferrari et al., *Proc. of the 1st International Workshop on Space Radiation Research and 11th NASA Space Radiation Health Investigators*, Arona (Italy) , May 2000.

[122] H. W. Atherton et al., CERN 80-07 (1980)

[123] G. Ambrosini et al., Phys. Lett. B **425** (1998) 208

[124] M. Boezio et al., Phys. Rev. D**62** (2000) 032007

[125] G. Battistoni et al., Astropart. Phys **17** (2002) 477-488

[126] G. Battistoni, Proc. of TAUP2001, Nucl. Phys. B (Proc. Suppl.) **110** (2002) 336-338

[127] S. Ahlen et al., Nucl. Inst. Meth. **A350** (1994) 351

[128] G. Stiegmann, Ann. Rev. Asron. Astroph. **14** (1976) 339

[129] G. D'Agostini, Nucl. Instr. Meth. **A362** (1995) 487

[130] E. W. Kolb and M. S. Turner, Ann. Rev. Nucl. Part. Sci. **33** (1983) 645

[131] R. S. Selesnick et al., J. Geophys. Res. **100 A6** (1995) 9503

[132] P. J. E. Pebbels, Principles of Physical Cosmology, Princeton University Press, Princeton N. J., 1993.

[133] J. Ellis et al., Phys. Lett. **B214** (1988) 403

[134] M. S. Turner and F. Wilzek, Phys. Rev. **D42** (1990) 1001

[135] D. Alvisi et al., Nucl. Inst. Meth. **A437** (1999) 212

[136] M. Acciarri et al., Nucl. Inst. Meth. **A351** (1994) 300

[137] J. Alcaraz et al., Il Nuovo Cimento **A112** (1995) 1325

[138] J. C. Hart and D. H. Saxon, Nucl. Inst. Meth. **A435** (1984) 309

[139] AMS Collaboration, J. Alcaraz et al., Phys. Lett. **B472** (2000) 215

[140] AMS Collaboration, J. Alcaraz et al., Phys. Lett. **B490** (2000) 27

[141] AMS Collaboration, J. Alcaraz et al., Phys. Lett. **B484** (2000) 10

[142] AMS Collaboration, J. Alcaraz et al., Phys. Lett. **B494** (2000) 202